

EXPLOITING LUMINESCENCE EMISSIONS OF SOLAR CELLS FOR INTERNET-OF-THINGS (IOT) APPLICATIONS

by

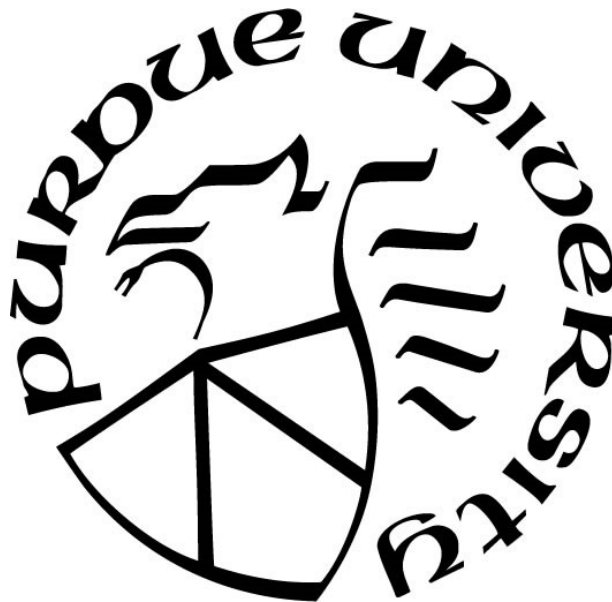
Xiaozhe Fan

A Dissertation

Submitted to the Faculty of Purdue University

In Partial Fulfillment of the Requirements for the degree of

Doctor of Philosophy



Department of Engineering Technology

West Lafayette, Indiana

May 2021

THE PURDUE UNIVERSITY GRADUATE SCHOOL
STATEMENT OF COMMITTEE APPROVAL

Dr. Walter D. Leon-Salas, Chair

School of Engineering Technology

Dr. Suranjan Panigrahi

School of Engineering Technology

Dr. Robert A. Nawrocki

School of Engineering Technology

Dr. Saeed Mohammadi

Department of Electrical and Computer Engineering

Approved by:

Dr. Kathryn A. Newton

*To my parents,
Jie Liu and Guangwei Fan,
To my girlfriend,
Li Song,
And to all my friends,
Without your support, none of my success would be possible*

ACKNOWLEDGMENTS

I would like to thank my advisor, Prof. Leon-Salas, for his valuable support throughout my entire Ph.D. marathon. I would like to delivery my sincere appreciation to Prof. Panigrahi, Prof. Mohammadi, and Prof. Nawrocki for their guidance. I would like to thank my parents, Guangwei Fan and Jie Liu for their encouragement. I would like to thank my girlfriend, Li Song for her company. I would like to thank my current and past teammates: Thomas Fischer, Taylor J. Zigon, Seungjin Lee, Samuel Denton, Sindhubala Kadirvelu, Jegan Rajendran, Jino Ramson, Archana Dharanipragada, Matthew Scott, and James A. Hidalgo for their care and fellowship.

This material is based upon work supported by the National Science Foundation under award no. ECCS-1809637.

TABLE OF CONTENTS

LIST OF TABLES.....	8
LIST OF FIGURES	9
LIST OF Abbreviations	14
ABSTRACT.....	16
CHAPTER 1. INTRODUCTION	17
1.1 Scope.....	18
1.2 Significance.....	20
1.3 Research Questions.....	20
1.4 Assumptions.....	21
1.5 Limitations	22
1.6 Delimitations.....	22
1.7 Contributions.....	22
1.8 Summary	23
CHAPTER 2. REVIEW OF LITERATURE	24
2.1 Solar Cell Based SWIPT Systems	26
2.2 Solar Cell Based Visible Light Identification System.....	27
2.3 Self-powered Microsystem Based on a Single LED.....	29
2.4 Self-powered Optical Transceiver Based on Retro-VLC Technique	29
2.5 Solar Cell Enabled Optical Frequency Identification (OFID) Technique	30
2.6 Summary	31
CHAPTER 3. RESEARCH METHODOLOGY	33
3.1 OFID Communication System Architecture.....	33
3.2 OFID Reader	34
3.2.1 Dual-Aperture Reader.....	35
3.2.2 Single-Aperture Reader	40
3.2.2.1 Optical System	41
3.2.2.2 Electronic System.....	42
3.3 OFID Tag Design.....	48
3.3.1 High-efficiency Solar Cells as Wireless Transmitter	48

3.3.2 Luminescent Emissions of Solar Cells	49
3.3.3 Simultaneous Information and Power Reception Circuit for OFID Tags	51
3.3.4 Luminescence Modulator Circuits.....	58
3.3.5 A Microcontroller-based OFID Tag for Temperature Sensing	58
3.3.6 An FPGA-based OFID Module for Sensing Applications	61
3.3.6.1 Power Management Unit.....	61
3.3.6.2 Receiver.....	64
3.3.6.3 Digital Controller	65
3.3.6.4 PL and EL Modulator.....	65
3.3.7 Summary.....	66
CHAPTER 4. RESULTS	67
4.1 Validation of Luminescent Emissions in a GaAs Solar Cell	67
4.2 Comparison of two PL Modulator Circuits	70
4.3 The First OFID System Prototype	75
4.4 The Second OFID System Prototype.....	78
4.4.1 Single-aperture OFID Reader	78
4.4.1.1 Wavelength Selection of Reader	78
4.4.1.2 LED Driver Linearity and Power Efficiency	79
4.4.1.3 Reader LED Driver Circuit Bandwidth.....	82
4.4.1.4 Reader Receiver Circuit Bandwidth	85
4.4.2 FPGA-based OFID Module.....	87
4.4.2.1 Reader Receiver Circuit Bandwidth	87
4.4.2.2 Noise Reduction Due to Band-pass Filter	89
4.4.2.3 Tag PL Modulator Bandwidth.....	92
4.4.2.4 Cold Startup and Power Consumption	100
4.4.3 Uplink and Downlink Communication Performance	107
4.4.3.1 BER Measurement in the Downlink Direction.....	107
4.4.3.2 BER Measurement in the Downlink Direction.....	113
4.4.3.3 Evaluation of Communication Range.....	116
4.5 Summary	121
CHAPTER 5. SUMMARY, CONCLUSIONS, AND RECOMMENDATIONS	124

REFERENCES	129
------------------	-----

LIST OF TABLES

Table 1. Comparison between OWC and RF communication technologies	24
Table 2. Model parameters of the GaAs solar cell.....	54
Table 3. Circuit parameters for both PL modulator & EH circuits.....	72
Table 4. Model Parameters	97
Table 5. Minimal quiescent currents consumed by various hardware components	107

LIST OF FIGURES

Figure 1. Possible applications of OFID systems.....	19
Figure 2. Solar cell enabled SWIPT system proposed by Fakidis et al. (2014, 2018); Malik and Zhang (2015); Y. Wang et al. (2018); Z. Wang et al. (2014, 2015); Zhang et al. (2015)	26
Figure 3. Solar cell enabled SWIPT system proposed by Fan and Leon-Salas (2017).	27
Figure 4. A solar cell based visible light identification system proposed by Lee (2015).	28
Figure 5. A Retro-VLC enabled smart dust device proposed in (J. Liu et al., 2019; O'brien et al., 2009).	30
Figure 6. OFID system architecture (Leon-Salas & Fan, 2019b).....	33
Figure 7. The proposed OFID reader topology by Leon-Salas and Fan (2019b). In both figures, the PL emission generated from an OFID tag is modulated in an on-off fashion.	34
Figure 8. The system architecture of a dual-aperture OFID reader (Fan et al., 2019).	35
Figure 9. Real optical systems for both transmitter and receiver. a) dissembled optical systems. b) assembled optical systems.	36
Figure 10. Real design of electronic systems on PCB boards.	37
Figure 11. A photograph of fabricated dual-aperture reader.	39
Figure 12. Conceptual diagram of the optical communication between the OFID reader and tag (Fan et al., 2021).	39
Figure 13. The schematic diagram of the single-aperture reader proposed in (Fan et al., 2021).	40
Figure 14. The photograph of the proposed single-aperture optical system.....	40
Figure 15. The schematic diagram of the electronic system architecture.....	42
Figure 16. The circuit diagram and photograph of the proposed LED driver.	43
Figure 17. The circuit diagram and photograph of the proposed receiver.....	45
Figure 18. Modelled and simulated frequency responses of the third-order bandpass filter for $R_4 = 15 \text{ k}\Omega$, $R_5 = 75 \text{ k}\Omega$, $C_1 = 750 \text{ nF}$, and $C_2 = 100 \text{ pF}$	47
Figure 19. The photograph of the digital control unit.....	47
Figure 20. Experiments showing luminescent emissions from a solar cell. a) The real experiment setup; b) Demonstrated PL emission when the cell was under both open circuit and short circuit conditions; c) Demonstrated EL emission when the cell was biased by an external power source with an output of 1.05 V (Leon-Salas & Fan, 2018).	50
Figure 21. A circuit model for the luminescent emission process in a solar cell (Leon-Salas & Fan, 2019a).	50

Figure 22. A simultaneous information and power reception circuit (SIPR) proposed by Fan and Leon-Salas (2017).	52
Figure 23. Small-signal model of a loaded solar cell.....	53
Figure 24. Measured and fitted IV curve of a GaAs solar cell.	54
Figure 25. Magnitude plots of transfer function $H1 = iscip_h$ and $H2 = vscip_h$	55
Figure 26. The magnitude plot of the transfer function H_{sense} under different R_s for cell's model parameters in Table 2 , $V_{SC} = 0.851$ V, $C_j = 798$ nF, $R_L = 90.5 \Omega$ and $C_L = 10 \mu F$	56
Figure 27. The magnitude plot of the transfer function H_{sense} under different CL for cell's model parameters in Table 2 , $R_s = 1 \Omega$, $V_{SC} = 0.851$ V, $C_j = 798$ nF, and $R_L = 90.5 \Omega$	57
Figure 28. The magnitude plot of the transfer function H_{sense} under different R_L for cell's model parameters in Table 2 , $R_s = 1 \Omega$, and $C_j = 798$ nF. V_{SC} varies with R_L	57
Figure 29. The circuit diagram and photograph of the proposed OFID tag.	59
Figure 30. The schematic diagram and photograph of the new proposed OFID module.	60
Figure 31. The schematic diagram of the energy harvester ADP5090	62
Figure 32. The experimental setup to evaluate the relationship between the luminescent radiant power and the bias voltage across the solar cell.	68
Figure 33. The measured optical power of luminescent emissions when the solar cell was under illuminated and dark conditions.....	68
Figure 34. Conceptual diagram of the experiment setup to validate the information transmission via the modulated PL emission.	69
Figure 35. Recorded waveforms at V_{TX} and V_{RX} when data was transmitted at different data rates. (a) 0.5 kbps. (b) 1 kbps. (c) 5 kbps. (d) 10 kbps.	70
Figure 36. Photo-luminescence modulation circuits proposed in (Leon-Salas & Fan, 2019b). ...	71
Figure 37. Photograph and schematic diagram of the experimental setup. (a) photograph of the setup. (b) schematic diagram of the setup (Leon-Salas & Fan, 2019b).....	72
Figure 38. Transmitted and received waveforms captured from both PL modulator & EH circuits (see Figure 36). (a) PL modulator & EH circuit 1. (2) PL modulator & EH circuit 2.....	73
Figure 39. A comparison of the maximum harvested power P_{Lmax} between two proposed PL modulator & EH circuits during data transmission.....	74
Figure 40. The measured BER versus distance for both circuits.	75
Figure 41. OFID system setup that demonstrated the wireless sensing functionality. The setup contained the first OFID reader prototype and the first OFID tag prototype.	76
Figure 42. Recorded charging profiles of the tag's supercapacitor with and without the data transmission event.....	76

Figure 43. Recorded temperature samples from the temperature meter and OFID reader.....	77
Figure 44. Experimental setup to measure harvested power when the solar cell was illuminated under different LED light. (a) photograph of the setup. (b) schematic diagram of the setup.....	79
Figure 45. Measured I-V and calculated P-V characteristic curves when the solar cell received the same radiant power generated by different LEDs.....	80
Figure 46. The conceptual and real experimental setups for evaluating both linearity and power efficiency of the LED driver.	81
Figure 47. The relationship between the LED's forward current I_{led} and modulation voltage V_{mod} for different converter's output voltage V_{dd} . (a) $V_{dd} = 2.2$ V. (b) $V_{dd} = 2.124$ V. (c) $V_{dd} = 2.027$ V. (d) $V_{dd} = 1.819$ V.....	82
Figure 48. Relationship between gate voltage V_g and LED's forward current I_{led} for $V_{dd} = 2.124$ V.....	83
Figure 49. Relationship between the driver's power efficiency, η_{tx} , and the modulation voltage, r V_{mod} , for different values of buck converter's output voltage, V_{dd}	83
Figure 50. Experimental setup to evaluate the driver's bandwidth. (a) photograph of the setup. (b) schematic diagram of the setup.....	84
Figure 51. Normalized frequency response of the LED driver.....	85
Figure 52. Experimental setup to measure the frequency response of the receiver in the reader. (a) photograph of the setup. (b) schematic diagram of the setup.....	86
Figure 53. Normalized frequency response of the receiver. Passive components used in this receiver (see Figure 52) are $R_1 = 20$ k Ω , $R_2 = 300$ k Ω , $R_3 = R_4 = 15$ k Ω , $R_5 = 75$ k Ω , $C_1 = 750$ nF, and $C_2 = 100$ pF.....	87
Figure 54. Experimental setup to measure the tag's bandwidth. (a) Photograph of the setup. (b) Schematic diagram of the setup.	88
Figure 55. Normalized frequency response of the OFID module.....	89
Figure 56. Experimental setup that evaluates the noise reduction performance of the receiver. (a) photograph of the setup. (b) schematic diagram of the setup.	90
Figure 57. Measured PSD of V_{out} when the solar cell received various radiant power.	91
Figure 58. Measured PSD of V_{out} with and without the band-pass filter when the solar cell received an irradiance 2.5 mW/cm ² and generated a photocurrent of 12 mA.	91
Figure 59. Experimental setup to evaluate the impulse response of the PL modulator. (a) photograph of the setup. (b) schematic diagram of the setup.	92
Figure 60. Captured waveforms V_{in} , V_{out} , and V_{sc} for the impulse response measurement when the solar cell received an irradiance of 3 mW/cm ² and generated a photocurrent of 13 mA.	93
Figure 61. PL modulator and its equivalent circuit when the transistor, M_1 is open or closed. (a) M_1 is closed. (b) M_1 is open.....	94

Figure 62. Measure and modelled cell's terminal voltage V_{sc}	95
Figure 63. Experimental setup for measuring cell's photoluminescence radiant power.....	96
Figure 64. Measured and modelled Φ_{lum} as a function of V_{sc}	96
Figure 65. Measured and modelled pulse response of the uplink communication system measured at V_{out}	98
Figure 66. Captured waveforms at V_{in} , V_{sc} , and V_{out} for the pulse response measurement under different received irradiance I_{in}	98
Figure 67. Captured waveforms at V_{in} , V_{sc} , and V_{out} for various pulse widths and for a received irradiance of 2.45 mW/cm ²	99
Figure 68. Captured waveforms V_{in} , V_{sc} , and V_{out} for various pulse amplitudes and for a received irradiance of 2.45 mW/cm ²	99
Figure 69. Experimental setup to capture the charging activity of the passive OFID tag. (a) photograph of the setup. (b) schematic diagram of the setup.	101
Figure 70. Captured charging profile in the cold startup when the solar cell received an irradiance of 10.3 mW/cm ² and generated a photocurrent of 41.2 mA.	102
Figure 71. Captured charging profiles during the cold startup process when the solar cell was illuminated with different irradiances. The plot also marks out the upper threshold voltage V_{upt} and lower threshold voltage V_{iot}	103
Figure 72. Captured charging profiles during the cold startup process for NVCM when the solar cell was illuminated with different irradiances. The plot also marks out the upper threshold voltage V_{upt} and lower threshold voltage V_{iot}	104
Figure 73. Captured charging profiles during the cold startup process when the FPGA was configured from an external flash memory or from an NVCM. The solar cell received an irradiance of 10.3 mW/cm ² and generated a photocurrent of 41.2 mA. The plot also marks out the upper threshold voltage V_{upt} and lower threshold voltage V_{iot}	105
Figure 74. Signal waveforms V_{out} and V_{ref} when the FPGA read programs from either the external flash or the NVCM.	105
Figure 75. Captured charging profile in the cold startup process for different capacitor values when the FPGA read program from NVCM. The solar cell received an irradiance of 10.3 mW/cm ² and generated a photocurrent of 41.2 mA.	106
Figure 76. An example DPIM waveform applied to V_{in}	108
Figure 77. Experimental setup for BER measurements in the downlink direction.	108
Figure 78. BER as a function of T_{s0}	109
Figure 79. Transmitted and received signal waveforms at V_{in} , V_{bp} , and V_{cmp} for $t_{pw} = 40 \mu s$, and for different different T_{s0} . (a) $T_{s0} = 300 \mu s$. (b) $T_{s0} = 125 \mu s$	110

Figure 80. The bit error rate as a function of T_{s0} for $t_{pw} = 40 \mu s$, and for three pulse amplitudes of V_{in} : $A = 200 \text{ mV}$, $A = 160 \text{ mV}$, and $A = 120 \text{ mV}$.	111
Figure 81. Transmitted and received signal waveforms at V_{in} , V_{bp} , and V_{cmp} for $t_{pw} = 40 \mu s$, and for two pulse amplitudes. (a) $A = 120 \text{ mV}$. (b) $A = 200 \text{ mV}$.	112
Figure 82. Experimental setup for BER measurements in the uplink communication scheme.	113
Figure 83. An example DPIM waveform applied to V_{in} .	114
Figure 84. BER as a function of T_{s0} for $I_{in} = 10.3 \text{ mW/cm}^2$ and $t_{pw} = 10 \mu s$.	114
Figure 85. Transmitted and received signal waveforms at V_{in} , V_{dfa} , and V_{cmp} for $I_{in} = 10.3 \text{ mW/cm}^2$ and $t_{pw} = 10 \mu s$ and two different T_{s0} . (a) $T_{s0} = 100 \mu s$. (b) $T_{s0} = 73 \mu s$.	115
Figure 86. The bit error rate as a function of T_{s0} when the solar cell received various irradiances.	116
Figure 87. State machine of the 4-ary DPIM encoder.	117
Figure 88. State machine of the 4-ary DPIM decoder.	118
Figure 89. The experimental setup, front and back views of the tag, and measured PLR as a function of the communication distance between the tag and reader. The PLR for each communication distance was evaluated using 1000 data packets. (a) photograph of the experimental setup. (b) front and back views of the tag. (c) measured PLR as a function of the communication range.	119
Figure 90. Typical example waveforms for one packet at a communication distance of 1.8 m. V_{tx} is the transmitted waveform at the tag's PL modulator while V_{ina} and V_{rx} are the received waveforms at the receiver's INA and comparator, respectively.	120
Figure 91. Typical example waveforms for one packet at a communication distance of 1.95 m. V_{tx} is the transmitted waveform at the tag's PL modulator while V_{ina} and V_{rx} are the received waveforms at the receiver's INA and comparator, respectively.	120

LIST OF ABBREVIATIONS

IoT	Internet of Things
RF	Radio Frequency
OWC	Optical Wireless Communication
OFID	Optical Frequency Identification
PL	Photoluminescence
EL	Electroluminescence
FPGA	Field Programmable Gate Array
PLR	Packet Loss Rate
BER	Bit Error Rate
ADC	Analog to Digital Converter
SWIPT	Simultaneous Wireless Information and Power Transfer
EH	Energy Harvesting
PV	Photovoltaic
DMM	Digital Multimeter
INA	Instrumentation Amplifier
TIA	Transimpedance Amplifier
DFA	Differential Amplifier
BPF	Band-pass Filter
CMP	Comparator
PCB	Printed Circuit Board
FCC	US Federal Communications Commission
LiFi	Light Fidelity
OCC	Optical Camera Communication

LiDAR	Light Detection and Ranging (LiDAR)
LED	Light Emitting Diode
MPP	Maximum Power Point
OC	Open Circuit
SC	Short Circuit
MRI	Magnetic Resonance Imaging
LC	Liquid Crystal
MRR	Modulated Retroreflector
RFID	Radio Frequency Identification
UART	Universal Asynchronous Receiver and Transmitter
I2C	Inter-Integrated Circuit
OOK	On-Off Keying
PPM	Pulse Position Modulation
DPIM	Digital Pulse Interval Modulation
EQE	External Quantum Efficiency
OP AMP	Operational Amplifier
I-V curve	Current-Voltage Curve
LCD	Liquid Crystal Device
LOS	Line of Sight

ABSTRACT

The Internet-of-Things (IoT) devices have experienced an explosive growth during the last decades. The number of IoT devices is predicted to reach 36.4 billion by 2025, resulting in an urgent demand for high-density and high-capacity network connectivity. Recently, self-powered optical wireless devices have attracted more attention from both academia and industry. Although radio frequency (RF) technologies are readily available for various wireless applications, the RF communication bands are becoming saturated due to the scarcity of the RF spectrum. Optical wireless communication (OWC) provides an attractive solution to overcome the shortage of RF bands. OWC is also attractive for low-power or even self-powered applications since optical energy is the most abundant in both indoor and outdoor scenarios.

This dissertation explores a new optical communication technique called optical frequency identification (OFID). This technique employs solar cells as an optical antenna, capable of harvesting energy and transmitting/receiving optical information. Transmission of information with a solar cell is achieved by modulating the cell's luminescent emissions. Two OFID system prototypes were designed, fabricated, evaluated, and discussed.

A series of experiments have been carried out to exploit the feasibility of using a solar cell's luminescence emissions for optical communication and evaluate proposed two OFID system prototypes. This dissertation firstly validated that luminescent emissions from a GaAs solar cell can be modulated for optical communications. Then, two photoluminescence (PL) modulators were proposed and compared in terms of their energy harvesting and communication performances. The first OFID system prototype, based on a dual-aperture reader and a microcontroller-based tag was validated and experimented for a remote temperature sensing application. The second prototype, based on a single-aperture OFID reader and an FPGA-based OFID module, was analyzed with an emphasis on the communication data rate, communication range, tag's cold-startup period and power consumption.

CHAPTER 1. INTRODUCTION

Internet-of-Things (IoT) wireless devices are expected to reach a number of 36.4 billion by 2025, as predicted by GSMA Intelligence (Kechiche, 2018). This unprecedented growth of IoT devices will enable a flourishing market of more than 1.3 trillion in a wide range of applications, such as smart city, industrial automation, healthcare, smart home, education, and precise agriculture (Ud Din et al., 2019). Fueled by the IoT vision, IoT devices have been evolved to achieve lower power consumption and long lifetime (Mamun & Yuce, 2019). A vast amount of IoT devices can currently operate seamlessly with an attached battery due to the advance in battery technologies. Although battery technologies provide an instant power solution, its drawbacks, including frequent recharging, limited recharging cycles, cost, and lack of sustainability, hinder the further bloom of IoT technology.

The simultaneous wireless information and power transfer (SWIPT) concept has been intensively explored to extend the lifetime of IoT devices (Krikidis et al., 2014). Although most research works have been carried out to use the radio frequency (RF) spectrum for both data transmission and energy harvesting (EH), only a few focused on the use of optical spectrum. Radio technologies based on unlicensed bands, such as Bluetooth, WiFi, Lora, and Zigbee, ease the deployment of IoT devices due to low cost, low complexity, unlicensed band, and abundant technical resources. However, these technologies are likely to slow down the growth of IoT networks due to several drawbacks, such as radio spectrum scarcity, radio interference, and security (Zhang et al., 2015). Therefore, exploring the SWIPT concept in the optical spectrum turns out to be significant due to its unregulated band, data security, high aggregate capacity, simplified design, and efficient spatial diversity (Fakidis et al., 2018).

The significance of using the optical spectrum for SWIPT is also favorably supported by the fact that light energy is the most abundant and readily available in the outdoor environment with a power density ranging from tens to more than a hundred mW/cm^2 (Gorlatova et al., 2010). The available ambient light is at least two orders of magnitude higher than those of ambient RF radiation (Pinuela, Mitcheson, & Lucyszyn, 2013). Recent advances in photovoltaic (PV) technology dramatically increase photovoltaic efficiency, reducing the cost per unit of harvested power. Additionally, a PV cell demonstrates the phototransduction property, effectively converting an optical signal to an electronic signal for wireless communication. Therefore,

exploring the use of existing photovoltaic cells for energy harvesting and data transfer becomes increasingly significant to achieve a next-generation self-powered IoT network without causing interference with an RF counterpart.

As solar cells' efficiency increases, approaching the Shockley-Queisser limit (e.g., 33.5 %), light extraction becomes a key engineering consideration, resulting in more substantial external luminescence emissions (Miller, Yablonovitch, & Kurtz, 2012). The strong photoluminescence from high-efficient GaAs solar cells was even captured using a commercial infrared camera in Leon-Salas and Fan (2018). By varying the bias voltage across solar cells, the photoluminescence emission changes accordingly and reaches its maximum when the cell is under the open-circuit condition (Rau, 2012). Therefore, photoluminescence emissions can be modulated to convey information. In addition to the luminescence property, solar cells also demonstrate photo-transconductance and photovoltaic properties for SWIPT (Fan & Leon-Salas, 2017). Full exploitation of these three solar cell properties has led to the creation of a new emerging wireless communication approach, firstly introduced in Leon-Salas and Fan (2018). This approach was named Optical Frequency Identification (OFID) technology, as an analog to the Radio Frequency Identification (RFID) technology. This dissertation focuses on the development of an OFID wireless system for low-power IoT applications. In an OFID system, mobile or sensing devices are equipped with solar cells as an optical antenna capable of harvesting energy and transmitting and receiving information. By reusing solar cells for multiple functionalities, the implementation of IoT devices with lower cost, size, and complexity is achievable.

1.1 Scope

The proposed optical frequency identification (OFID) technique has enabled a wide range of potential applications. Fueled by the OFID vision, OFID wireless devices can be integrated into everyday objects to monitor their health conditions and surrounding environments. **Figure 1** shows different application scenarios where the proposed OFID communication system can be employed.

Figure 1a demonstrates a bridge health monitoring application in which an OFID system is employed to monitor mechanical conditions, such as physical stresses, crack widths, and vibrations. **Figure 1b** shows an OFID system is employed to monitor environmental parameters

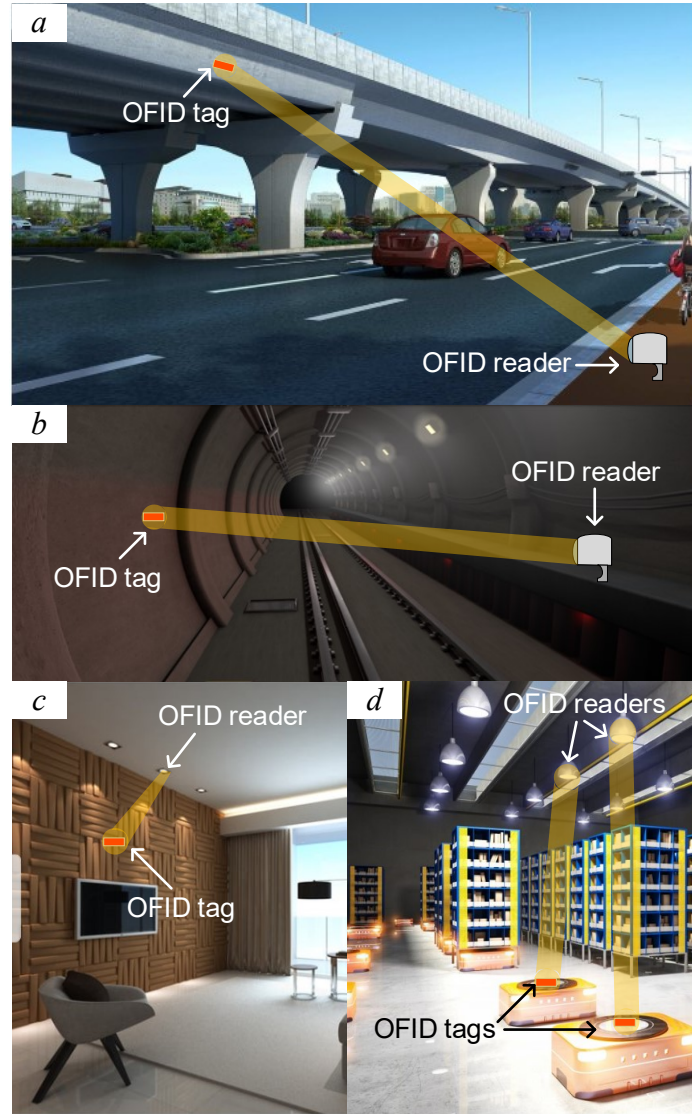


Figure 1. Possible applications of OFID systems.

in a tunnel, such as temperature, humidity, air quality, and illumination intensity. An ambient light source in the tunnel can be modified to work as an OFID reader. The deployment of OFID systems in a tunnel also reduces maintenance activities in replacing or recharging a battery.

Figure 1c shows an OFID system is installed in a smart home environment. Light bulbs in the room can be employed as an OFID reader. **Figure 1d** presents a warehouse environment where packages on moving robots are tracked and monitored using an OFID system. Besides environmental sensing applications mentioned above, one of the attractive advantages of the OFID system is that OFID tags can be localized using an imaging camera. Therefore, an OFID

reader can be replaced with a camera so that it can receive information from OFID tags while pointing out the precise location of each tag. Other applications were suggested in Leon-Salas and Fan (2018).

1.2 Significance

The significance of this dissertation is mainly highlighted by a developed proof-of-concept OFID communication systems. The developed system demonstrates the following advantages: 1) light can be easily collimated into a narrow beam with a compact optical system, delivering both power and information over a relatively long distance without dramatic signal attenuation. In contrast, in an RF transmitter it is much more difficult to achieve the same beam collimation levels, which is limited physically by the RF wavelength. 2) Unlike an RF-based receiver, a commercial camera can receive data from multiple OFID tags, simplifying the demand for collision avoidance mechanisms and minimizing optical interference from the background. In addition to data reception, a camera can also pinpoint the position of an OFID tag, reducing the dependence on other positioning systems (e.g., GPS, UWB). 3) OFID tags can harvest energy from sunlight, targeting a truly self-sustainable IoT network without the use of any power resources on earth. 4) OFID tags can be placed on or near metallic surfaces without any levels of degradation on their performance. RF-based devices require special mounts to avoid detuning effects, which in turn increases the cost and size. 5) OFID tags also overcome the RF interference challenges faced by RF counterparts. 6) Wireless communication via light makes it easy to secure data against casual eavesdropping since light cannot penetrate through opaque barriers (e.g., walls, containers). The deployment of OFID tags not only enlarges the capacity of existing wireless networks but also meets the emerging trend of developing energy harvesting capability. In both outdoor and indoor scenarios, battery replacement or recharging in this huge IoT network has imposed more challenges and maintenance costs. Fueled by the OFID concept, this problem will be tackled more effectively, sustainably, and efficiently.

1.3 Research Questions

The questions central to this study were:

- What are hardware architectures for both an OFID reader and an OFID tag?

- What are the highest data rate and communication range that can be achieved in the proposed OFID system?
- What are the minimum cold-startup period and power consumption in the proposed passive OFID tag?

The research questions were answered by taking following steps:

1. Reviewed previous publications regarding state-of-the-art circuit designs that are required to build an OFID system.
2. Summarized the advantages and disadvantages of previous works and proposed new circuits that can address limitations in previous works.
3. Designed and fabricated two OFID system prototypes.
4. Carried out quantitative experiments to characterize the fabricated OFID system.

1.4 Assumptions

The following assumptions regarding experiments were made to ease this study:

- Power supplies were reliable and stable during the experiments.
- The test equipment, such as digital multimeter (DMM), oscilloscope, function generator, spectrum analyzer, optical power meter, source meter, and current sensor, were as accurate as what had been reported in their user manuals.
- The methodology used in this study was appropriate to answer research questions.
- Characteristics of passive components used in the OFID system, such as resistors, capacitors, and inductors, did not change over time or with frequency.
- Characteristics of optical semiconductors used in an experiment, such as the LED, photodiode, and solar cell, did not change over time.
- Electrical parameters of electronic components (i.e., silicon chips) were stable during experiments.
- The impact of printed circuit board (PCB) on system performances, such as bandwidth, power consumption, and noise, was neglected.
- Solar cells used in this research work were made out of GaAs by Alta Devices.

1.5 Limitations

The following limitations were inherent to the pursuit of this study:

- The quality of collected data relied on the accuracy of the test equipment.
- As the proposed OFID system used off-the-shelf components, tolerances inherent in passive components, such as resistors, and capacitors, had an impact on the system performance.
- The switching activity in power supplies injected additional ripple noise into a system during experiments.
- Ambient noises from a fluorescent lamp in the test laboratory interfered with communication signals.
- Due to limited transmittance and reflectance of optical components (e.g., lens and mirrors), optical power losses in the reader became significant, resulting in less power delivery from the reader to an OFID tag.
- The size of proposed OFID tags was limited by that of selected off-the-shelf components.
- The power consumption and cold startup time of OFID tags were limited by selected off-the-shelf components.

1.6 Delimitations

This study was carried out with the following delimitations:

- This study did not involve optimizing optical systems.
- This study did not focus on comparing and evaluating off-the-shelf components.
- This study did not include evaluating optical communications using the EL emission from a solar cell.
- This study only characterized dominant noise sources, such as optical ambient noises and switching ripple noise, and did not focus on characterizing other noise sources (e.g., electronic noise, and thermal noise).

1.7 Contributions

The contributions of this dissertation were listed as follows:

- This dissertation validated the use of solar cells for three purposes, such as energy harvesting, data transmission and data reception.
- This dissertation introduced a simultaneous wireless information and power reception circuit based on a modified DC-DC converter.
- This dissertation presented two photoluminescence (PL) modulator \& energy harvesting (EH) circuits for concurrent energy harvesting and information transmission.
- This dissertation presented two OFID system prototypes and evaluates the performance of these two prototypes. The first prototype consisted of a dual-aperture OFID reader (see Section 3.2.1) and a microcontroller-based OFID tag (see Section 3.3.5). The second prototype consisted of a single-aperture reader (see Section 3.2.2) and an FPGA-based OFID module (see Section 3.3.6).
- This dissertation developed various optical testbeds for characterizing proposed OFID systems.
- This dissertation provided the theoretical analysis of the photoluminescence modulation, that was verified experimentally.
- This dissertation experimentally determined the highest data rate and the communication range under various luminance conditions.

1.8 Summary

This chapter included the scope, significance, research question, assumptions, limitations, delimitations, and contributions of this dissertation. The next chapter reviews previous works relevant to this research.

CHAPTER 2. REVIEW OF LITERATURE

Optical wireless communication (OWC) has attracted tremendous interest during the last decades in both industry and academia. Although radio frequency (RF) based technologies, such as WiFi, Zigbee, Bluetooth, and LoRa, are currently embedded in various wireless applications, the RF spectrum has become insufficient to serve the massive connectivity required by the internet of things (IoT) paradigm. The scarcity of the RF spectrum was predicted to be a major cause of heavy data traffic for the future connectivity (Tsonev, Videv, & Haas, 2015). Moreover, only a few unlicensed bands are available to the public. For example, the US Federal Communications Commission (FCC) provides only a few unlicensed bands, such as 900 MHz, 2.4 GHz, and 5.8 GHz. Additionally, severe interference occurs between two RF access points if they are too close (Jokanovic & Josipovic, 2011). To relieve the overloading RF spectrum, researchers have been actively exploring new communication spectra, such as millimeter and manometer waves, to accommodate the increasing number of physical wireless devices (Hanzo et al., 2012).

As a complementary technology to RF communication, OWC has been considered as a significant contributor to the future high-density and high-capacity IoT networks. Even if OWC is only applicable to limited applications, it provides unique advantages over RF-based technologies. **Table 1** shows a comparison of OWC and RF technologies in terms of their properties (Kahn & Barry, 1997). Different OWC technologies, such as light fidelity (LiFi), optical camera communication (OCC), and light detection and ranging (LiDAR), have been proposed and explored to meet the demand of IoT paradigm and other application requirements.

Table 1. Comparison between OWC and RF communication technologies

Property of Medium	RF	OWC
Available spectrum range	~ 300 GHz	~ 800 THz
Licensing requirement	Licensed	Unlicensed
Noise sources	Other RF sources	Ambient light
Security	Low	High
Electromagnetic interference	Wide	Limited
Signal-to-noise ratio	High	Low

LiFi technology, as analogous to WiFi technology, provides not only high-speed communication links but also illumination. As a result, LiFi technology can be integrated into current lighting infrastructure (Haas & Chen, 2015; Lu et al., 2017; Svilen & Harald, 2015). OCC takes advantage of existing camera systems and converts them to optical receivers. Consequently, a modified camera can perform both image sensing and optical communication (Goto et al., 2016; Yamazato et al., 2014; Zheng, Liu, & Hu, 2017). LiDAR utilizes remote sensing technology to find the range and other information associated with a distant object (Qin, Vu, & Ban, 2012; Queralta et al., 2019).

Besides the demand for high-density and high-capacity connectivity, the fast development of the IoT paradigm also requires low-power, ultralow-power, or even self-powered sensing devices. The lifetime of an IoT network can be extensively extended if sensing devices can harvest energy from the environment to support their power usage (J. Liu et al., 2019). A unique advantage of self-powered sensing devices is they can be placed at difficult to access locations to continuously monitor their surrounding environment without replacement or recharging of a battery (Park, Rosing, Todd, Farrar, & Hodgkiss, 2008). There are various energy sources from which energy is available to be harvested (Chalasani & Conrad, 2008). Sunlight has been commonly accepted as the most abundant, clean, reliable, and sustainable energy source, among others, including heat, vibration, radio radiation, and wind (Gorlatova et al., 2010). The most effective and efficient approach to converting light to electricity is using photovoltaic (PV) technology in which solar cells play an essential role. Over the past five years, advances in solar cells have promoted the cell's photovoltaic efficiency closer to the theoretical upper limit, defined by the Shockley-Queisser (SQ) formalism (Nayak, Mahesh, Snaith, & Cahen, 2019).

The unprecedented growth in PV technology prolongs the operation of low-power IoT devices and reduces their dependence on a battery. As a result of this encouraging trend, optical energy harvesting (OEH) has been widely accepted as a substitute to battery technology, reshaping the entire IoT network to be more environmentally friendly and sustainable (Omairi, Ismail, Danapalasingam, & Ibrahim, 2017).

Solar cells become one of the key solutions that integrate both optical wireless communication and energy harvesting (EH) in one IoT device. The rest of this chapter reviews recent progresses in OWC systems in which mobile devices are capable of harvesting energy.

2.1 Solar Cell Based SWIPT Systems

The simultaneous wireless information and power transfer (SWIPT) concept offers a framework in IoT paradigm (Krikidis et al., 2014). In this new concept, the exploration of SWIPT in the optical spectrum has attracted tremendous attention recently. An optically based SWIPT system provides some advantages over RF-based solutions. On one hand, sunlight provides the most abundant and sustainable power, two orders of magnitude higher than ambient RF radiation (Pinuela et al., 2013). On the other hand, advances in photovoltaic technology have enabled a mass deployment of PV cells, tremendously reducing the cost of using the optical SWIPT approach. Fueled by the rapid development of photovoltaic technology, the use of solar cells for SWIPT purposes has been intensively investigated.

Fakidis et al. (2014, 2018); Malik and Zhang (2015); Y. Wang et al. (2018); Z. Wang et al. (2014, 2015); Zhang et al. (2015) took a similar circuit design approach to extract both power and information from a solar cell. As illustrated in **Figure 2**, the proposed SWIPT system consists of a transmitter and a receiver. The transmitter was made of an LED driver and an LED, delivering both power and data to a receiver. The receiver consisted of a solar cell, an energy harvesting circuit branch, and a signal processing circuit. The energy harvesting circuit used an inductor L to pass DC signals and block AC signals for energy harvesting. The signal processing circuit employed a capacitor C to pass information encoded in AC signals and blocked DC signals. In the signal processing circuit, amplifiers and filters were used to further process received AC signals and converted them to a digital format acceptable by a digital system.

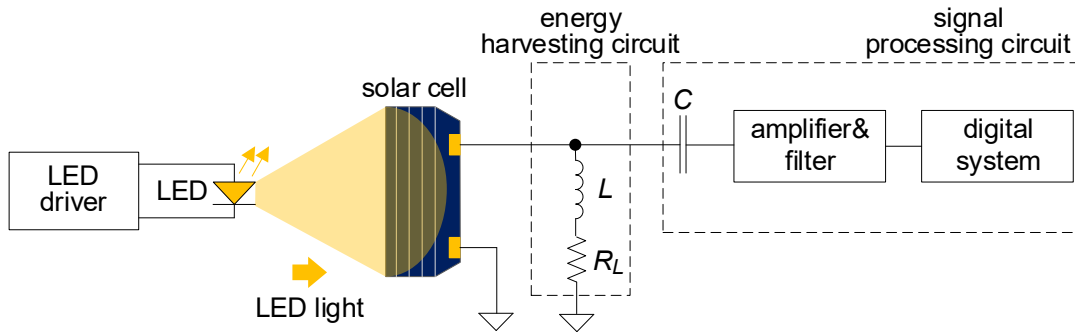


Figure 2. Solar cell enabled SWIPT system proposed by Fakidis et al. (2014, 2018); Malik and Zhang (2015); Y. Wang et al. (2018); Z. Wang et al. (2014, 2015); Zhang et al. (2015)

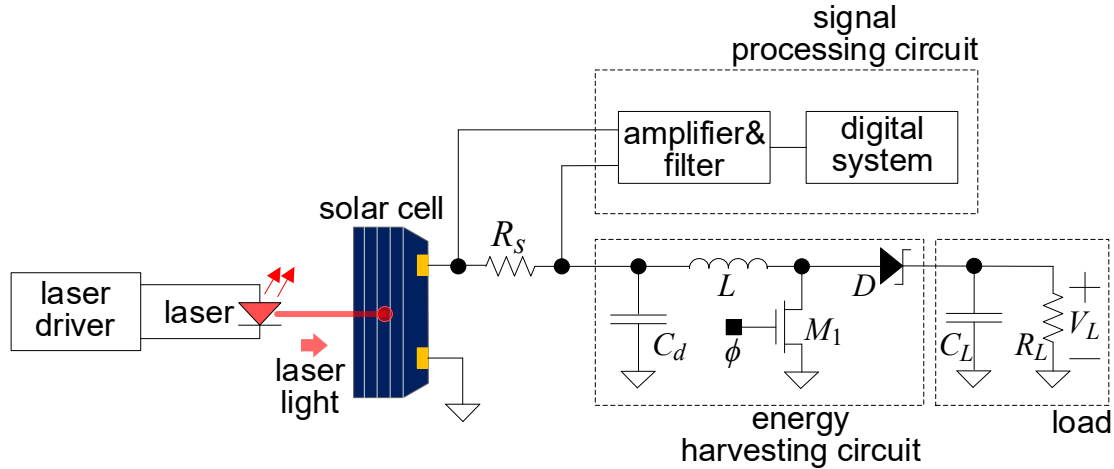


Figure 3. Solar cell enabled SWIPT system proposed by Fan and Leon-Salas (2017). impedance of the solar cell.

However, the voltage at the load R_L highly depended on the input optical power as well as the

Fan and Leon-Salas (2017) proposed an improved SWIPT receiver in which a modified DC-DC boost converter was employed. **Figure 3** shows the proposed SWIPT system. The use of DC-DC boost converter not only converted the low-level voltage at the solar cell (e.g., 0.3 V - 0.7 V) to a standard voltage acceptable by most electronic components but also extracted the most power from the cell by employing the maximum power tracking (MPPT) algorithms. The receiver employed a current sense resistor R_s to sense information as a form of current and converted it to a voltage difference, further processed by the signal processing circuit. The energy harvesting circuit (i.e., DC-DC boost converter) was capable of providing a higher voltage at the load, free from any fluctuations due to a change of either the input radiance level or load impedance.

2.2 Solar Cell Based Visible Light Identification System

As described in the previous section, research works that focused on the SWIPT system only studied the downlink communication in which information was transmitted from a transmitter to a receiver. It is viable and simple to achieve a two-way optical communication using two symmetric one-way data links (Al-Halafi & Shihada, 2018). However, an asymmetric OWC system is typically required in an IoT application where mobile or sensing devices are

2.3 Self-powered Microsystem Based on a Single LED

Haydaroglu and Mutlu (2015) proposed a microsystem that used a single LED as both the optical transmitter and receiver. The system consisted of three components: a storage capacitor, an LED, and an integrated chip. In order to meet challenges in designing miniaturized wireless systems for some biomedical applications, such as magnetic resonance imaging (MRI), OWC based technologies have demonstrated unique advantages over RF-based counterparts due to improved energy harvesting efficiency. The use of single LED for both energy harvesting and information transmission has gained an essential benefit in reducing the system size. An LED die with a peak emission of 770 nm was selected in this work as a result of its efficient energy harvesting capability over a small region of electromagnetic spectrum (Moayeri Pour, Benyhesan, & Leon-Salas, 2014). The microsystem communicated with an external reader that consisted of a laser as the transmitter and a photodiode as the receiver.

Since the same LED was used for both power reception and data transmission, light for both purposes should locate at different regions of the optical spectrum. As presented in the paper, the absorption and emission spectra of the LED were separated around 20 nm. Therefore, Haydaroglu and Mutlu (2015) chose a 660 nm laser to power the microsystem without causing interference with the LED's emission spectrum. However, LED only demonstrated around 10 % normalized absorption efficiency at 660 nm. Additionally, the LED consumed the most power for data transmission when compared to other circuit components.

2.4 Self-powered Optical Transceiver Based on Retro-VLC Technique

To further minimize the power consumption that is dominated by an active optical transmitter (e.g., an LED or a laser) in self-powered IoT devices, J. Liu et al. (2019); O'brien et al. (2009) employed a modulated retro-reflector (MRR) as the transmitter. **Figure 5** illustrates a schematic of the fabricated device, consisting of a photodiode-based power harvesting source, a storage capacitor, an optical receiver, an optical transmitter, and an integrated circuit die. The power harvesting source was implemented using a serial connected N-well/P-sub and T-well/N-well diode (J. J. Liu et al., 2014). On-chip diode, compatible with standard CMOS fabrication processes, supported smart dust that consumed power with a range of a few hundred nano Watts to a few micro-Watts. The transmitter consisted of a liquid crystal (LC), an LC modulator, a

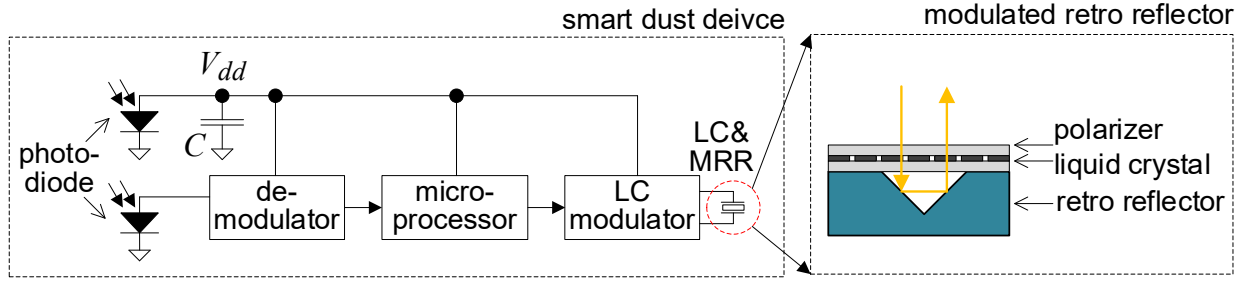


Figure 5. A Retro-VLC enabled smart dust device proposed in (J. Liu et al., 2019; O'brien et al., 2009).

polarizer, and a retro-reflector. Information was transmitted back to a reader by modulating the polarity of reflected light from the retro-reflector. The Retro-VLC is a type of backscattering technique with which most of the power used for information transmission comes from an optical power source (i.e., a reader). Therefore, nano-powered devices can be achieved using this technique.

However, Retro-VLC based smart dust suffered from several drawbacks. Firstly, the smart dust charged and discharged a liquid crystal for data transmission, resulting in a highly limited bandwidth (Li et al., 2015). The smart dust presented in (J. Liu et al., 2019; O'brien et al., 2009) only featured the uplink data rate of 10 bps. Secondly, the proposed system used three components for energy harvesting, data transmission, and data reception, preventing the system size from being further reduced. Finally, the diode used for the energy harvesting only provided an output between 0.5 V to 0.8 V. Such a low supply voltage might enforce the designers to design systems in sub-threshold regimes, complicating the matching of transistors in both analog and digital circuits (A. Wang, Calhoun, & Chandrakasan, 2006).

2.5 Solar Cell Enabled Optical Frequency Identification (OFID) Technique

In (Leon-Salas & Fan, 2018), which contains contribution of author to this dissertation, a new approach that uses solar cells as the optical antenna was proposed. Leon-Salas and Fan (2018) demonstrated both strong photoluminescence (PL) and electroluminescence (EL) generated from a GaAs solar cell. This research work also validated the use of PL emission for data transmission. Therefore, the same solar cell was proposed to achieve triple functionalities, such as energy harvesting, data transmission, and data reception. The proposed technique adopted the

similar working mechanism as compared to the radio frequency identification (RFID) technology. Therefore, authors in this paper named this technique as the optical frequency identification (OFID).

There are a few advantages of an OFID enabled IoT device over works that described in previous sections:

1. Solar cells are generally designed for harvesting energy from solar light so that they are highly efficient over a wide spectrum range. IoT devices that are equipped with a solar cell can work in a variety of lighting scenarios.
2. An OFID system uses the PL emission to transmit information from a tag to a reader. Modulating the PL emission can be simply carried out by connecting/disconnecting the load from solar cell via a MOSFET switch (Leon-Salas & Fan, 2019a). As a result, the power consumed in transmitting information is less than other approaches (e.g., modulating an active transmitter (Haydaroglu & Mutlu, 2015) or an LCD (J. Liu et al., 2019)).
3. Reusing the same solar cell for energy harvesting and bi-directional communication leads to further size reduction of a microsystem.
4. An OFID enabled sensing device can achieve an uplink data rate of a few tens of kbps, sufficient for most environmental and biomedical events (Hempstead, Lyons, Brooks, & Wei, 2008).

This dissertation explored the use of solar cells as a transmitter, aiming to develop an OFID system for IoT applications.

2.6 Summary

Optical wireless communication (OWC) has attracted significant interest from academia and industries recently due to the scarcity of radio frequency (RF) spectrum. Therefore, OWC has been accepted as one of the complementary technologies to RF-based counterparts. OWC is anticipated to achieve a high-density and high-capacity network, especially for IoT applications. As most IoT mobile or sensing devices are powered using a battery, they are designed to be low power, ultralow-power, or even self-powered. Integrating both OWC and energy harvesting (EH) on the same device provides a promising solution to meet challenges in developing self-powered IoT devices. These self-powered IoT devices are the best candidates to monitor harsh

environments where minimum human activities are involved. This literature review focuses on self-powered devices that use light for both energy harvesting and wireless communication.

Based on the literature review discussed, the use of a single solar cell as the optical antenna demonstrates its uniqueness in co-optimizing energy harvesting efficiency, device size, and power consumption in data transmission. The energy harvesting efficiency can be maximized by selecting a high-efficient cell (e.g., GaAs and CdTe) interfaced with a high-efficient DC-DC boost converter with the maximum power point tracking (MPPT) control. PL emission in a solar cell, triggered by external light, can be modulated to carry information. Accordingly, less energy is required for the PL modulation when compared to an active transmitter (e.g., an LED or an LCD) used in previous works. Reusing the same solar cell for triple functionalities, such as energy harvesting, data transmission, and data reception leads to a further reduction of the system size.

The next chapter provides the framework and methodology for developing an OFID communication system that uses solar cells as an optical antenna.

CHAPTER 3. RESEARCH METHODOLOGY

This chapter provides the framework and methodology essential for designing an optical OFID system that takes advantage of luminescence emissions from a solar cell. As analogical to an RFID system, the OFID system consists of an OFID reader and an OFID tag. Section 3.1 introduces the general system architecture of the OFID system. Section 3.2 and 3.3 explains the design of both OFID reader and tag in detail, respectively. Section 3.4 concludes this chapter.

3.1 OFID Communication System Architecture

Figure 6 shows the basic architecture of an OFID communication system. Similar to an RFID system, the OFID system consists of both an OFID reader and an OFID tag (Leon-Salas & Fan, 2019b). The reader, equipped with an optical emitter (e.g., an LED or a laser diode) and an electronic driver, produces light to fulfill the following tasks: 1) energizing an OFID tag; 2) exciting the tag's solar cell to generate the photoluminescent (PL) emission; and 3) conveying information to the tag via intensity modulation. The reader also contains a photodetector (e.g., a photodiode) and an electronic receiver that detects changes in the luminescent emissions from the reader. The received signal is then processed by a digital controller, such as a microcontroller or an FPGA. User-interface electronics are used to bridge the digital controller and users. For example, An LCD display can be used to visualize received information.

The OFID tag, equipped with a direct band-gap solar cell (e.g., GaAs or CdTe), contains several key features: 1) harvesting energy from received light; 2) exchanging information with

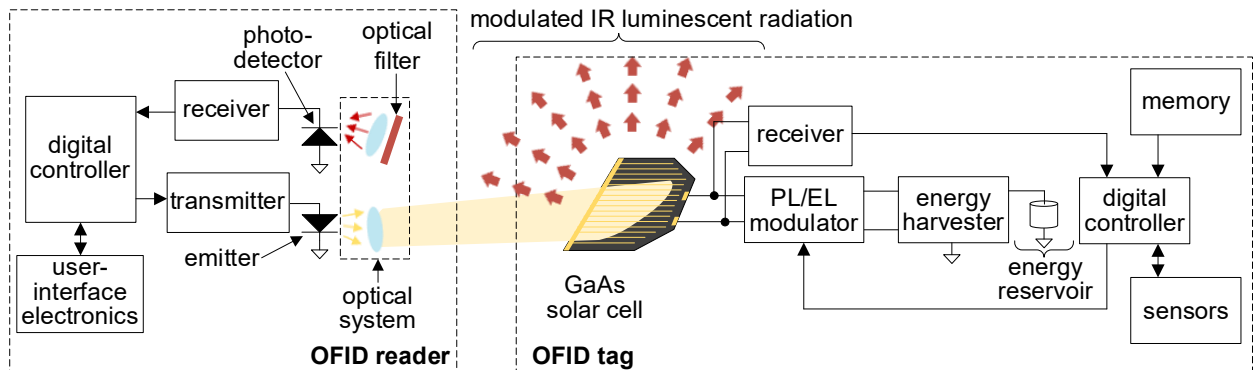


Figure 6. OFID system architecture (Leon-Salas & Fan, 2019b)

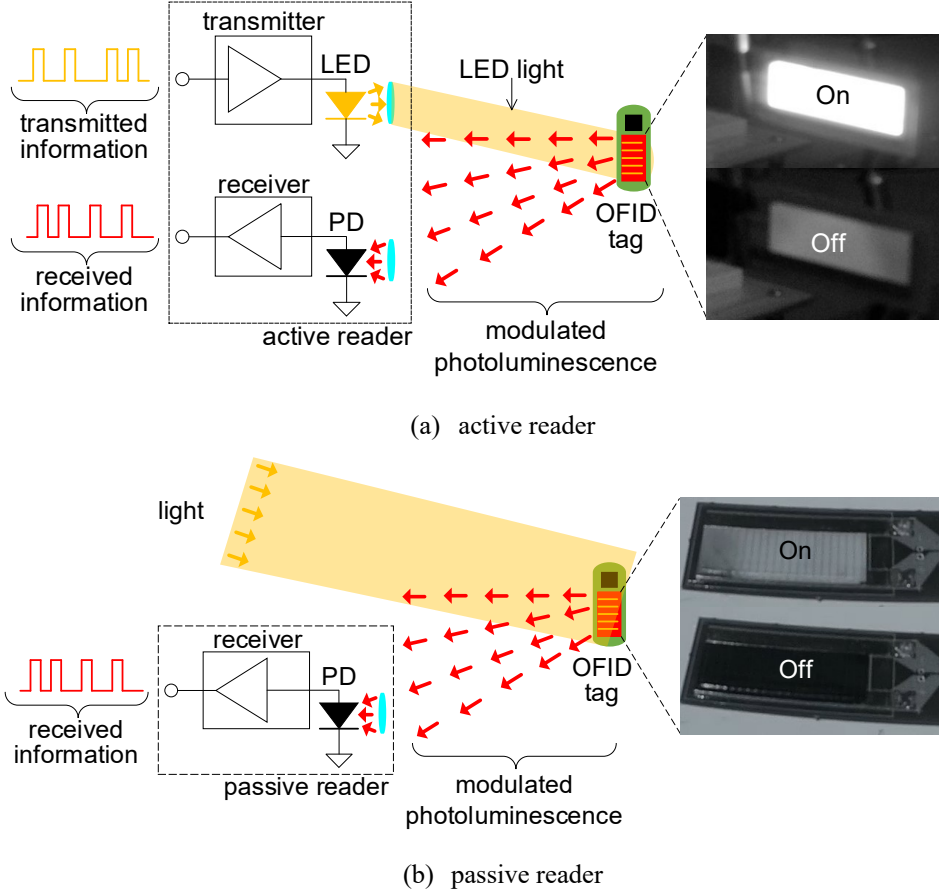


Figure 7. The proposed OFID reader topology by Leon-Salas and Fan (2019b). In both figures, the PL emission generated from an OFID tag is modulated in an on-off fashion.

the OFID reader via uplink and downlink optical channels; 3) monitoring environmental parameters (e.g., temperature, and humidity) using sensors; and 4) logging data into non-volatile memory. The OFID tag can either be active or passive depending on whether the energy reservoir is an active source, i.e., a battery. A passive tag, equipped with a passive energy reservoir (e.g., a capacitor or a supercapacitor), relies only on an external energy source, while an active tag can use energy from the energy reservoir even without the presence of the external energy source. The rest of this chapter explains the design of both reader and tag in detail.

3.2 OFID Reader

Leon-Salas and Fan (2019b) have proposed two types of reader topology: active reader and passive reader, as illustrated in **Figure 7**.

An active reader generally finds its applications in an indoor environment where ambient light (e.g., fluorescent light) is too weak to excite detectable PL emissions from an OFID tag. In this case, the PL emission can be excited using an active reader. The active reader is capable of transmitting both power and information.

As compared to an active reader, a passive reader does not illuminate OFID tag. As a result, the OFID tag produces the PL emission stimulated by ambient light (e.g., sunlight). Although the passive reader shows a few advantages over the active counterpart in terms of reduced complexity, power consumption, cost, and size, it does not transmit information. Hence, it is not possible to interrogate an OFID tag with a passive reader. In this dissertation, only the active topology is explored. Accordingly, two versions of the active reader (e.g., the single-aperture reader and the dual-aperture reader) have been implemented and discussed. The rest of the section introduces the design of both readers.

3.2.1 Dual-Aperture Reader

The first active OFID reader architecture, based on a dual-aperture optical architecture, was

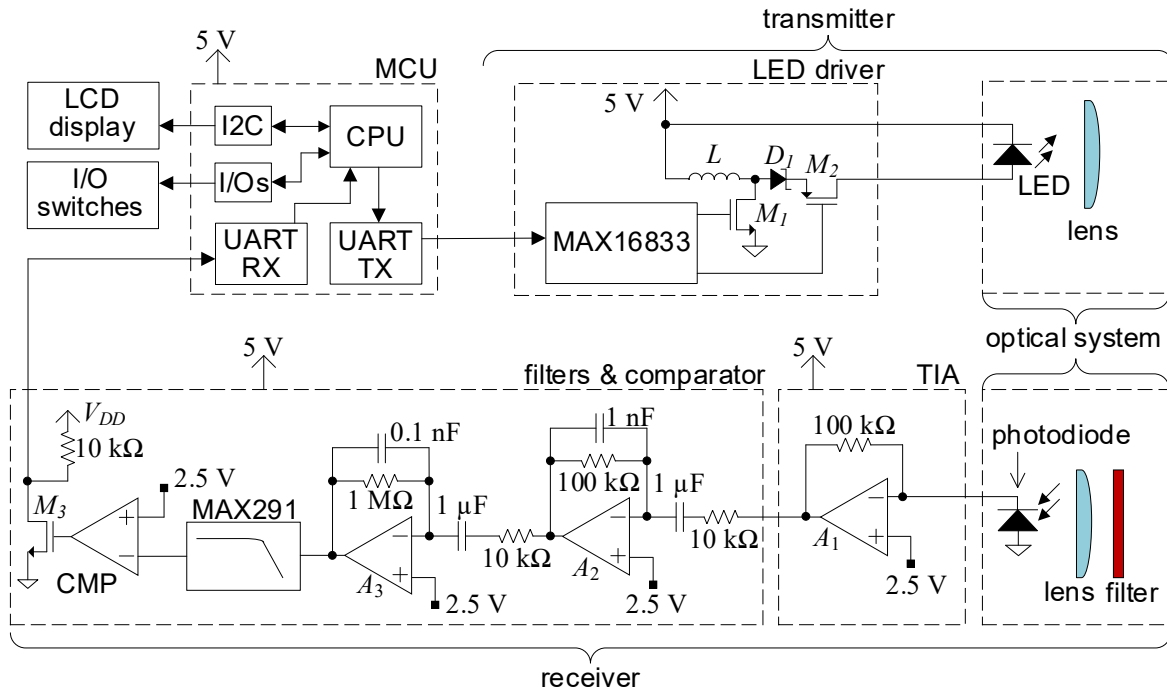


Figure 8. The system architecture of a dual-aperture OFID reader (Fan et al., 2019).

introduced by Fan et al. (2019) (see **Figure 8**). The reader contains separate optical apertures to transmit and receive information. The optical system in the transmitter consists of a high-power red LED (Cree XPEBRD) and a plastic plano-convex lens. This LED, mounted individually on an aluminum PCB board, generates light with an emission peak close to 625 nm. The plastic plano-convex lens was placed in front of the LED to focus the light beam on a target OFID tag. Both the LED and lens were housed in a modified flashlight head. The optical system in the receiver contains a photodiode (Vishay BPW34S), a plastic plano-convex lens, and a long-pass optical filter (ZOMEI 30mm-IR-850). The selected photodiode demonstrates nearly the highest relative spectral sensitivity to luminescent emissions (e.g., 886 nm) from the solar cell used in this dissertation. The plastic lens focuses the received light beam onto the photodiode. Featured in a cut-off wavelength at 850 nm, the long-pass filter passes received luminescent emissions, while reducing the optical interference from an ambient light source (e.g., an LED lamp). The photodiode, lens, and long-pass filter were housed in a separate flashlight head. **Figure 9** shows photographs of assembled and disassembled optical systems for both transmitter and receiver.

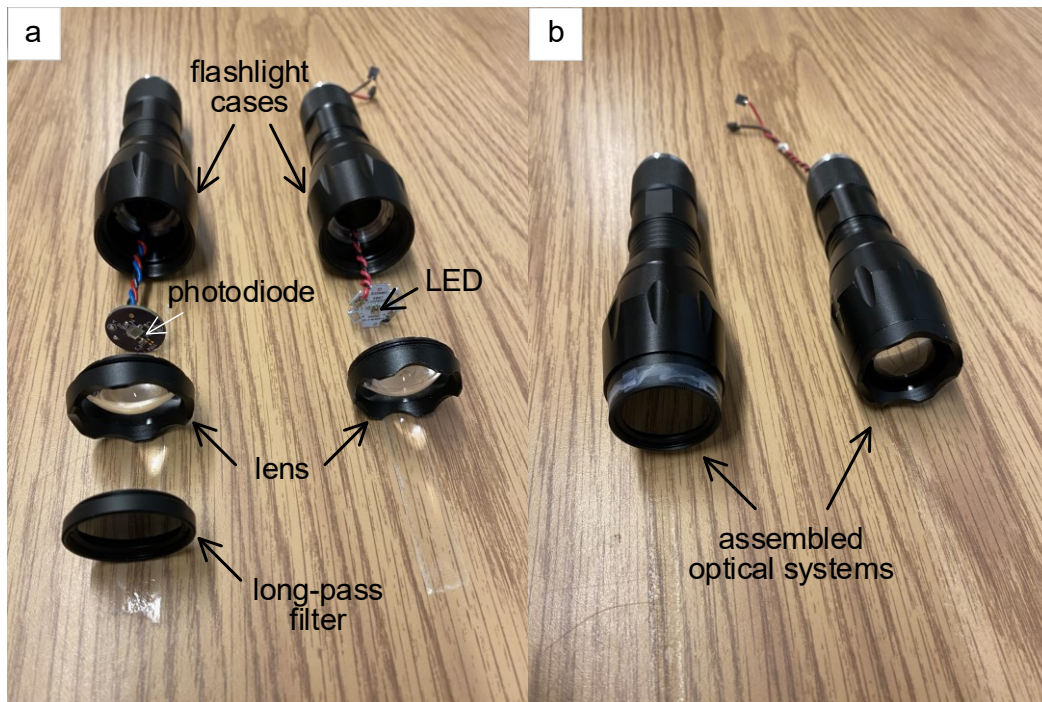
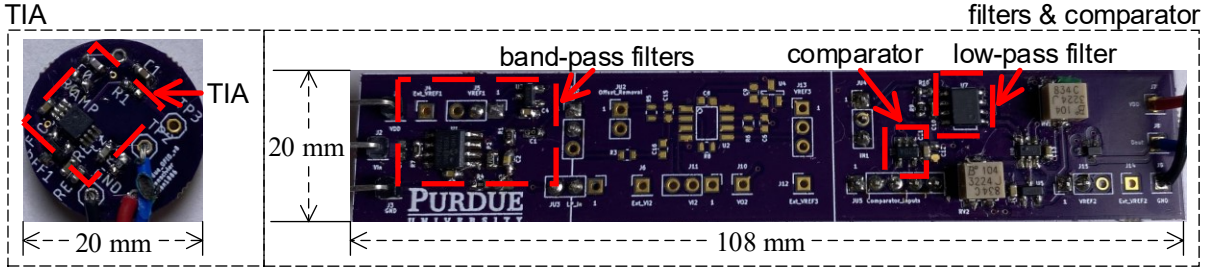
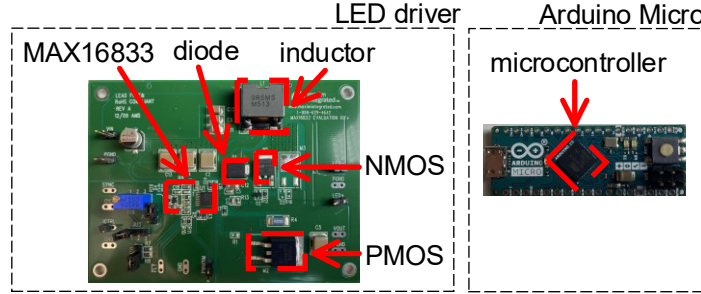


Figure 9. Real optical systems for both transmitter and receiver. a) disassembled optical systems. b) assembled optical systems.



(a) Receiver electronic system



(b) Transmitter electronic system and microcontroller

Figure 10. Real design of electronic systems on PCB boards.

Besides the optical system, the electronic system also plays an important role in building both transmitter and receiver. As shown in **Figure 8**, the transmitter employs an inductive-boost LED driver (Maxim Integrated MAX16833) to control the LED. The driver applies a pulse-width modulated (PWM) signal to the gate of the N-channel MOSFET M_1 , efficiently transferring power from a power source (not showing in the Figure) to the LED. In terms of the information modulation, the LED driver modulates the gate of the P-channel MOSFET M_2 in an on-off fashion according to a bit stream being transmitted. An evaluation board for MAX16833 from Maxim Integrated was selected, as shown in **Figure 10b**.

The receiver consists of a front-end transimpedance amplifier (TIA), two first-order active band-pass filters based on opamps (Microchip MCP6002), an 8th-order low-pass filter (Maxim Integrated MAX291), and a comparator (Texas Instruments LMV7239). The transimpedance amplifier (TIA), built with an opamp (Microchip MCP6002), amplifies the photocurrent generated from the photodiode. The TIA has a trans-impedance gain of 100 k Ω . Both TIA and photodiode were mounted on a circular PCB board with a diameter of 20 mm (see **Figure 10a**). The shape of PCB board was selected to fit into the modified flashlight head. The output of the TIA was connected to two cascaded first-order band-pass filters. Each band-pass

filter features a gain of 1000 V/V and -3 dB corner frequencies at 16 Hz and 1600 Hz, respectively. The lower and upper corner frequencies were selected to reduce the interference from ambient sources (e.g., a fluorescent lamp) (Narasimhan, Audeh, & Kahn, 1996), while providing a sufficient pass-band for communication signals. In order to secure a robust data link, the receiver's pass-band was suggested to cover the first null in the PSD of received signals for the OOK modulation (Kahn & Barry, 1997). As a result, the data rate of OOK signals is suggested to be equal to or less than the upper corner frequency of the receiver (Zhang, 2000). The 8th-order low-pass filter with the upper corner frequency of 10 kHz further reduces high-frequency noises. The corner frequency of this low-pass filter is adjustable using an external oscillator. The comparator performs the analog-to-digital (A/D) conversion using the thresholding technique, significantly reducing the demodulation complexity and power consumption as compared to the use of an analog-to-digital (ADC). The NMOS M_3 bridges the comparator with a microcontroller from Arduino by converting the comparator's output from push-pull type to the open-drain type. Filters and comparator were integrated on another customized PCB board, as illustrated in **Figure 10a**.

A microcontroller board (Arduino Micro) was employed to control the LED driver and receiver and communicate with other user-interface electronics, such as an LCD (Hiletgo HD44780) and several pushbuttons. Several internal software modules, such as the I2C, UART data transmission (TX) module, UART data reception (RX) module, and I/Os, were implemented with the microcontroller. The TX module converts binary information to an asynchronous bitstream that was sent to the LED driver. The RX module decodes the received asynchronous bitstream and extracts binary information accordingly. The I2C module communicates with the external LCD display to visualize received information. I/Os interact with external pushbuttons so that users can ask the reader to perform different tasks.

On-off keying (OOK) modulation was used for both uplink and downlink communications. The OOK is the most used technique in optical communications due to its simplicity. In OOK, the optical emitter (e.g., an LED or a solar cell) generates a rectangular pulse to represent the bit '1' and no pulse to represent the bit '0'. The bandwidth required by OOK approximately equals to the bit rate (Kahn & Barry, 1997). In the proposed dual-aperture reader, data was encoded in a four-byte packet. The data packet consists of one identification byte, a payload-type byte, a data byte, and a checksum byte. The identification byte contains the ID

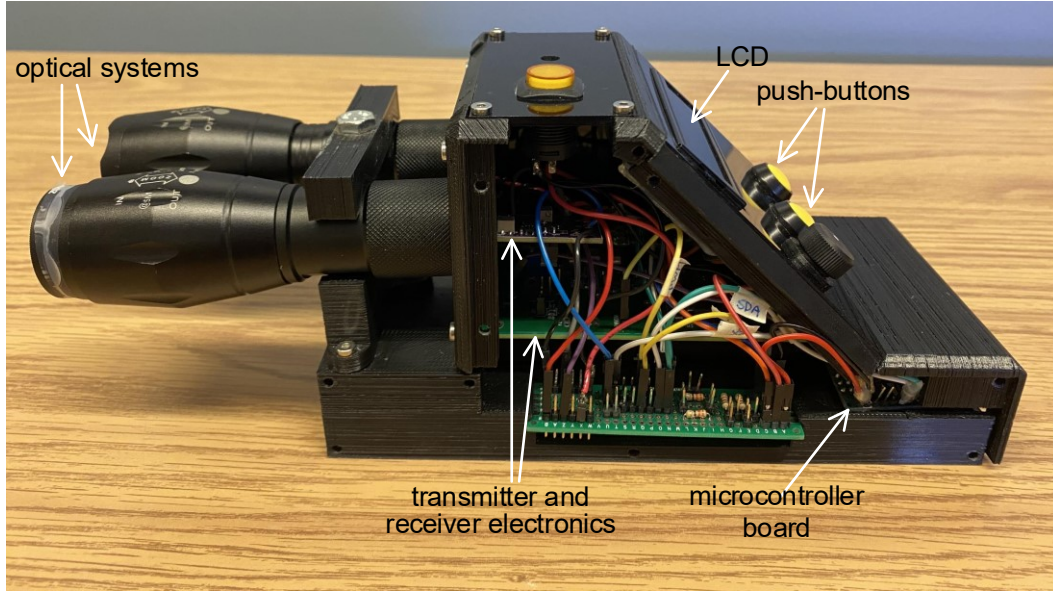


Figure 11. A photograph of fabricated dual-aperture reader.

number of a target OFID tag. Both payload-type byte and data byte contain information that command a tag to perform different tasks. Accordingly, the implemented tasks are: 1) data acquisition, which could request sensor data and battery status if a tag contains sensors and a battery, and 2) blinking, which commands the tag to blink its solar cell. The checksum byte calculates the sum of all three leading bytes, modulo 256.

Both optical systems and electronic systems were outfitted in a custom 3D printed enclosure, as illustrated in **Figure 11**. To successfully establish a communication link between the dual-aperture reader and an OFID tag, the tag must be present in the communication region (see **Figure 12**), i.e., an overlapping region between the uplink and downlink channels.

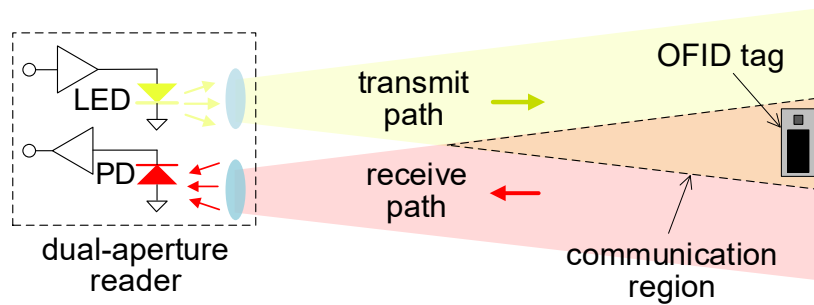


Figure 12. Conceptual diagram of the optical communication between the OFID reader and tag (Fan et al., 2021).

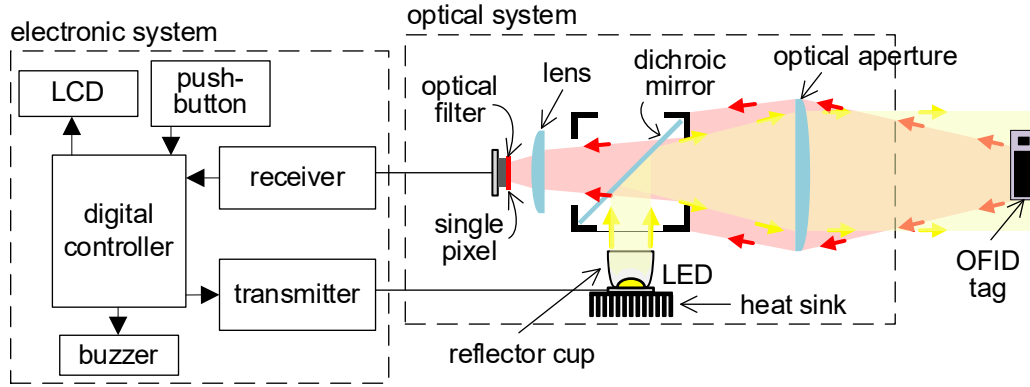


Figure 13. The schematic diagram of the single-aperture reader proposed in (Fan et al., 2021).

However, the size and location of the communication region highly depends on the relative angle between two apertures and the distance between the reader and the tag. To decouple the dependence of the communication region on these geometrical parameters, a single-aperture optical architecture should be used (Fan et al., 2021).

3.2.2 Single-Aperture Reader

The single-aperture reader was described in (Fan et al., 2021) and is shown in **Figure 13**. The reader design improves the alignment between the tag and the reader compared to the dual-aperture reader. The single-aperture reader consists of both optical and electronic systems. The optical system was built with off-the-shelf optical elements. The electronic system contains a

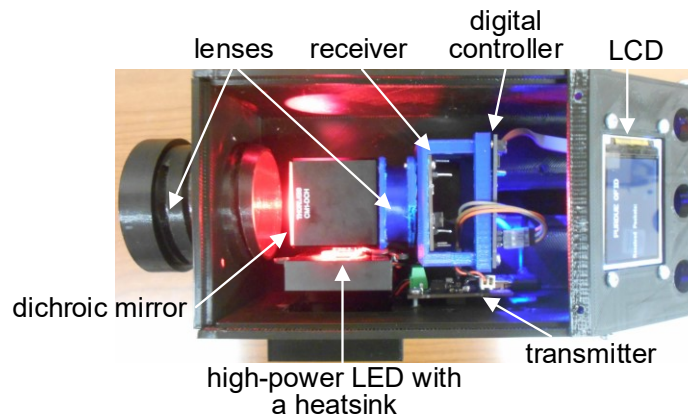


Figure 14. The photograph of the proposed single-aperture optical system

mix of customized PCB boards made for the receiver, LED driver and digital controller, and other user-interface electronics, such as pushbuttons, LCD screen, and buzzer. **Figure 14** shows a prototype of the single-aperture reader. The rest of this section describes both optical and electronic systems in detail.

3.2.2.1 Optical System

A high-power far-infrared (Cree XPEBFR) with the peak emission at 720 nm has been selected for the OFID reader. There are a few reasons to support the selection of this wavelength. Firstly, the GaAs solar cell from Alta Devices used in the research demonstrates the highest external quantum efficiency (EQE) at the far-infrared wavelength (Alta Devices, 2014). Secondly, the emitted light from far-infrared LEDs still covers a small portion of the visible spectrum, providing a visual guide for the optical alignment between the reader and an OFID tag. A dome lens, mounted on top of the LED chip, maximizes light extraction and refines the emission pattern (Moreno, 2006). However, the half-power beamwidth is nearly 110 degrees, resulting in partial radiant energy being leaked in the optical system. In order to increase the light extraction efficiency of the optical system, a reflector (OPC OPC11COL) with a viewing angle of 7 degrees was used to narrow the light beam. A long pass dichroic mirror (ThorLabs DMLP805R), placed 45 degrees above the horizontal, bends the LED light beam by 90 degrees. The dichroic mirror, encapsulated in a cage cube (ThorLabs CM1-DCH), has a reflectance of 99.9 % at the LED's emission wavelength. A plano-convex lens (Thorlabs LA1050AB) focuses the reflected light beam on the OFID tag. The lens has a focal length of 100 mm and an antireflection coating in the 400 - 1100 nm range. The OFID tag generates the PL emission, which propagates back to the reader. Since the PL emission and LED light are located at different spectrum regions, no significant interference occurs between these two spectral components. The plano-convex reshapes the received PL emission so that it forms a narrower viewing angle. The dichroic mirror presents a nearly transparent window for the PL emission with a transmittance of 97 %. An aspheric lens located between the dichroic mirror and a photodiode (Vishay Semiconductors BPW34S) concentrates the PL emission onto the photodiode. An optical bandpass filter (Quanmin QM-NBF850-50), mounted on top of the photodiode, passes the PL emission while removing other spectrum components.

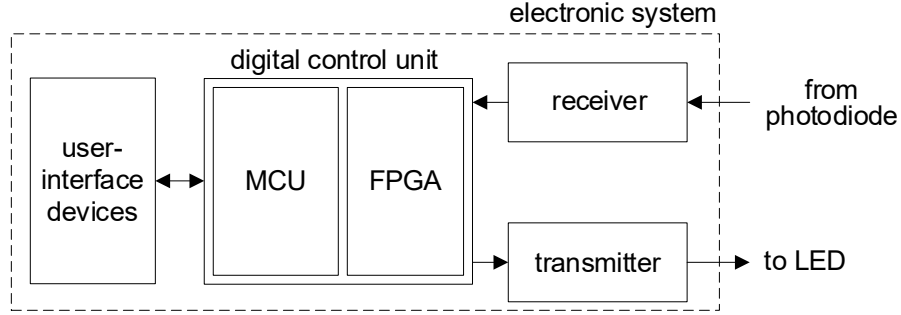


Figure 15. The schematic diagram of the electronic system architecture

3.2.2.2 Electronic System

As one of two essential systems in the proposed reader, the electronic system carries out multiple data processing tasks, such as modulation/demodulation, encoding/decoding and data visualization. The electronic system consists of three major functional subsystems: a LED driver, a receiver, and a digital control unit. These three subsystems have been implemented on different PCB boards. **Figure 15** shows the schematic diagram the electronic system.

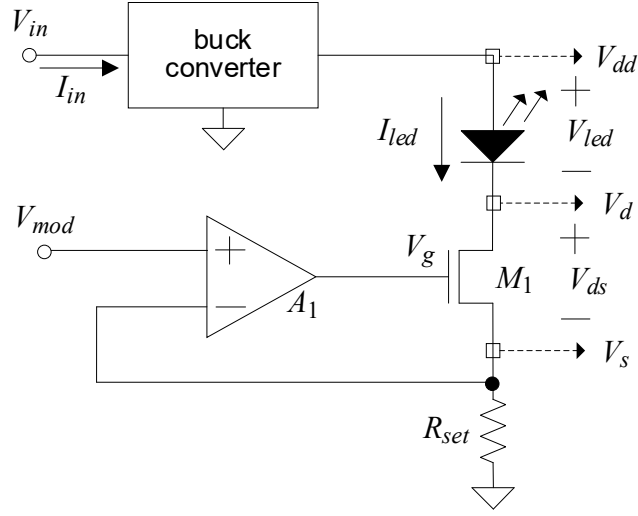
3.2.2.2.1 LED Driver

The LED driver controls the high-power LED to generate both power and information (Gioux et al., 2008). **Figure 16** shows both the circuit diagram and photograph of the LED driver. It consists of a buck converter (Texas Instruments TPS54719), a N-channel power MOSFET M_1 (STMicroelectronics STL6N2VH5), a $0.25\ \Omega$ power resistor R_{set} , and an operational amplifier A_1 (Analog Devices ADA4841). The rest of this section describes the circuit operation in detail.

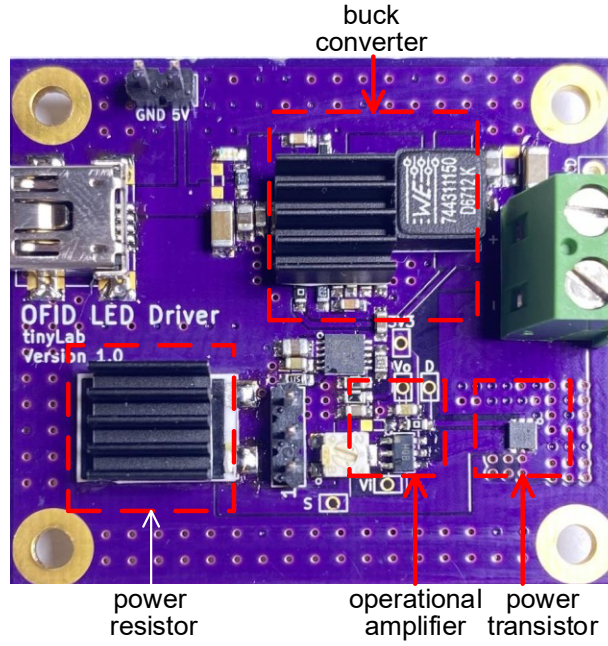
The power MOSFET M_1 along with the op amp A_1 form a feedback network, setting the LED's forward current I_{led} to $I_{led} = \frac{V_s}{R_{set}}$. Although the use of the power resistor R_{set} dissipates extra power, it enables a linear control over I_{led} . A linear LED driver is used as it is compatible with analog modulation techniques (Leon-Salas & Fan, 2019b). Due to the virtual ground property of the op-amp, I_{led} varies with the modulation voltage V_{mod} (Razavi, 2001):

$$I_{led} = \frac{V_{mod}}{R_{set}}$$

Equation 1. The relationship between I_{led} and V_{mod}



(a) Schematic



(b) Photograph

Figure 16. The circuit diagram and photograph of the proposed LED driver.

Therefore, I_{led} can be linearly controlled by V_{mod} .

The power efficiency of the LED driver η_{tx} , as one of critical system parameters, determines the battery lifetime. η_{tx} is the ratio of the LED's power usage P_{led} to the driver's input power P_{in} . P_{led} and P_{in} can be derived by multiplying the voltage and current across the

LED and the LED driver, respectively (e.g., $P_{led} = V_{led} \times I_{led}$ and $P_{in} = V_{in} \times I_{in}$). Therefore, η_{tx} can be formulated as follows:

$$\eta_{tx} = \frac{V_{led} \times I_{led}}{V_{in} \times I_{in}}$$

Equation 2. Power efficiency calculation

3.2.2.2.2 Receiver

The receiver performs multiple signal processing tasks, such as amplification, filtering, and A/D conversion. **Figure 17** shows the circuit diagram of this receiver. The photodiode PD (BPW34s) converts the received optical signal into an electrical signal and is reverse-biased to ensure a linear optoelectronic transduction (Sze & Ng, n.d.). The front-end TIA (Texas Instruments) with a transimpedance gain of R_1 converts I_{ph} to a pseudo-differential voltage output. The TIA is followed by a fully-differential amplifier (DFA) (Texas Instruments THS4551) to convert the pseudo-differential signal to a fully-differential signal. A third-order band-pass filter, made of three cascaded DFAs, amplifies the input signal and filters it by removing low-frequency and high-frequency components. The pass-band of the filter depends on the target application. The instrumentation amplifier (INA) (Texas Instruments INA331) performs the differential-to-single-ended conversion. A comparator (LMV7235) employs the thresholding technique to demodulate the input analog signal.

The gain of the receiver is configurable by selecting gain-setting resistors for each stage of amplifications. The TIA offers two possible gains (e.g., 5 kV/A and 20 kV/A). Compared to the gain of 5 kV/A, the gain of 20 kV/A provides a higher signal-to-noise ratio (SNR) and fourfold amplification of input signals. However, the larger gain might saturate the TIA, distorting received signals. The DFA, right after TIA, generates a fully-differential output. The gain of DFA G_{dfa} is determined by:

$$G_{dfa} = \frac{R_3}{R_2}$$

Equation 3. The gain of DFA

The DFA's gain should be small in order to prevent the output being saturated. The band-pass filter, consisting of three cascaded DFAs, not only determines the passband of the receiver but also further amplifies the output from the previous stage. The gain of this filter at the passband is given by:

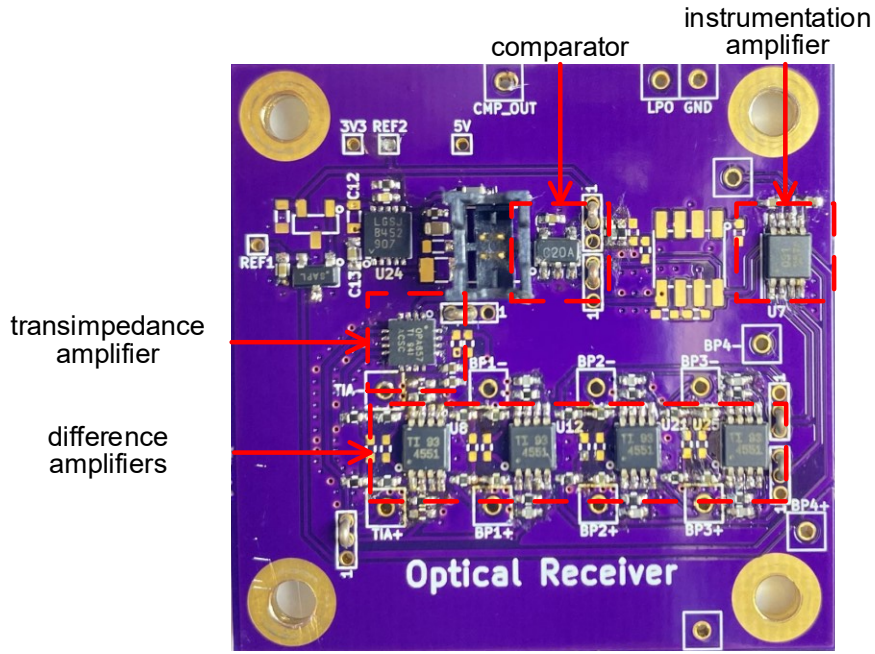
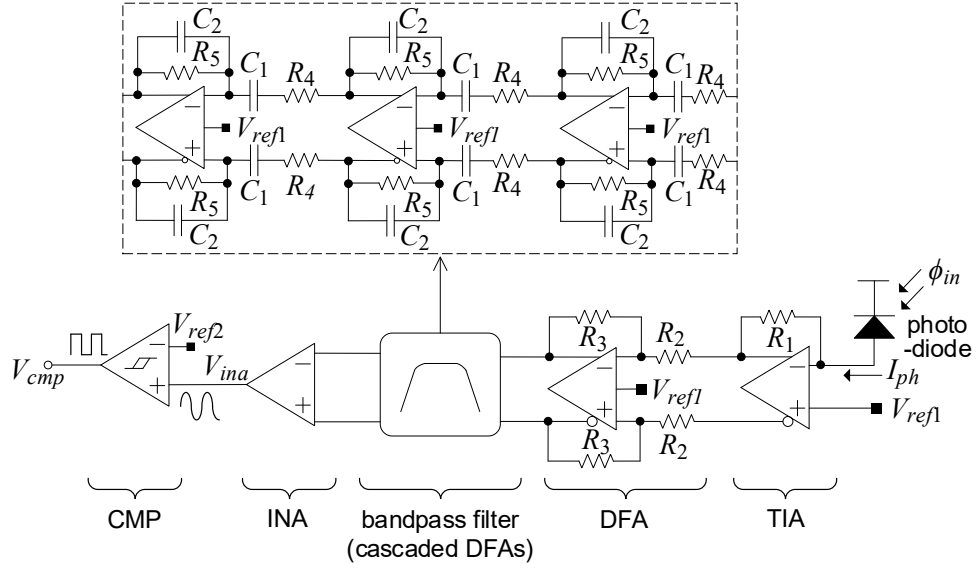


Figure 17. The circuit diagram and photograph of the proposed receiver

$$G_{bp} = \left(\frac{R_5}{R_4} \right)^3$$

Equation 4. The gain of the band-pass filter

The instrumentation amplifier (INA) carries out differential-to-single-ended conversion and the

INA's gain G_{ina} is determined using an external resistor, R_g .

The band-pass filter determines the pass-band and corner frequencies for the receiver. Corner frequencies should be adjusted to minimize the ambient optical noise that is coupled by the photodiode. As an example of a typical office environment, fluorescent lamps driven by electronic ballasts generate an infrared periodic signal that is modulated at a rate of tens of kilohertz (Narasimhan et al., 1996). For an indoor application, the pass-band of the filter should be customized to reduce the ambient noise from a fluorescent lamp. The transfer function $H_{bp}(f)$ of this filter is given by:

$$H_{bp}(f) = - \left(\frac{\frac{R_5}{C_2} (j2\pi f)}{R_4 R_5 (j2\pi f)^2 + \left(\frac{R_5}{C_1} + \frac{R_4}{C_2} \right) (j2\pi f) + \frac{1}{C_1 C_2}} \right)^3$$

Equation 5. The transfer function of the band-pass filter

To validate the **Equation 5**, the transfer function was plotted in MATLAB and compared with the simulation result from Multisim. **Figure 18** shows transfer functions extracted from both equation 3.6 and the SPICE simulation. The result shows that the modelled and the measured frequency responses agree fairly well demonstrating the validity of the derived analytical model. The filter has -3 dB corner frequencies at 27.7 Hz and 10.7 kHz for $R_4 = 15 \text{ k}\Omega$, $R_5 = 75 \text{ k}\Omega$, $C_1 = 750 \text{ nF}$, and $C_2 = 100 \text{ pF}$.

3.2.2.2.3 Data Processing Unit and User Interface Electronics

As shown in **Figure 15**, the digital control unit contains a microcontroller, and an FPGA. The FPGA (Lattice ICE5LP4K) is mainly responsible for data decoding and exchanging data with the microcontroller (Atmel ATmega328P), as well as controlling the LED driver and receiver. **Figure 19** shows a photograph of the digital control unit.

When the reader gets ready to interrogate an OFID tag, the microcontroller generates several data packets and sends them to the FPGA via a UART interface. The FPGA decoder received data packets using a custom digital pulse interval modulation (DPIM) decoder. The FPGA can be used to implement a variety of digital modulations, such as Manchester coding, OOK, pulse position modulation (PPM), and DPIM.

When the reader receives data packets generated by the OFID tag, the reader's receiver circuit filters and amplifiers the received signal and passes it to the decoder in FPGA. During the

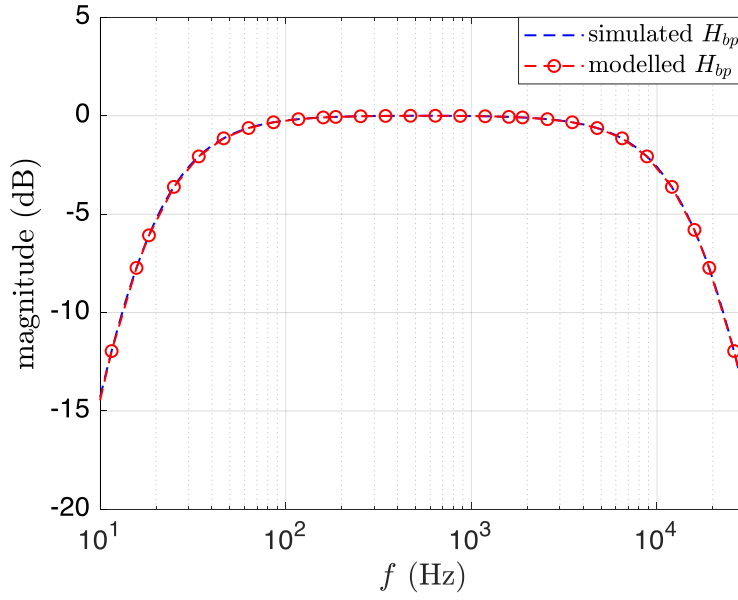


Figure 18. Modelled and simulated frequency responses of the third-order bandpass filter for $R_4 = 15 \text{ k}\Omega$, $R_5 = 75 \text{ k}\Omega$, $C_1 = 750 \text{ nF}$, and $C_2 = 100 \text{ pF}$.

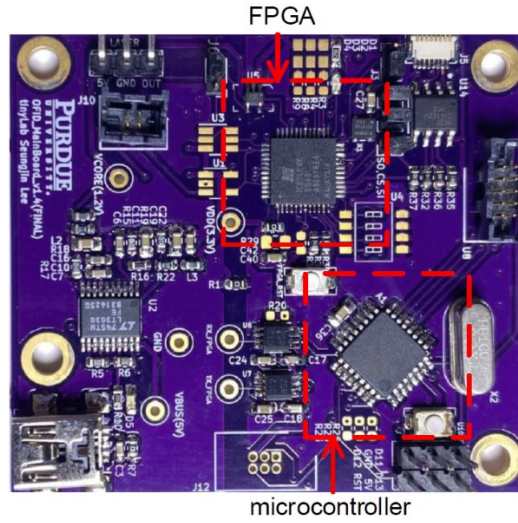


Figure 19. The photograph of the digital control unit.

microcontroller via a UART interface. Information is then processed by the microcontroller and displayed on the LCD screen.

3.3 OFID Tag Design

This section provides the methodology for the design of an OFID tag. Similar to an RFID tag, an OFID tag can harvest energy from an external energy source and communicate with a reader via a bi-directional communication link. The OFID tag can be either active or fully passive. An active tag can be energized using either a battery or an external energy source, while a passive tag can only be activated by the reader's emitted radiation. The rest of this section introduces the feasibility of using a solar cell as a wireless transmitter, the required circuit components for an OFID tag system, and two implemented tag designs.

3.3.1 High-efficiency Solar Cells as Wireless Transmitter

An antenna converts electromagnetic waves to an electrical signal and vice versa. As a result, information can be transmitted and/or received with the antenna. When equipped with a rectifier circuit, an antenna can be used to harvest energy (McSpadden, Lu Fan, & Kai Chang, 1998). The antenna's triple functionalities, such as information transmission/reception and energy harvesting, have been fully explored in the radio frequency identification (RFID) technology (Want, 2006). As compared to an RF antenna, solar cells made out of direct bandgap semiconductor such as GaAs or CdTe also demonstrates potential capabilities in transmitting/receiving information and harvesting energy. The use of solar cells for simultaneous wireless information and power transfer (SWIPT) technology has been extensively explored during the decades (Bialic, Maret, & Ktenas, 2015; Fakidis et al., 2014, 2018; Fan & Leon-Salas, 2017; Haas, Videv, Das, Fakidis, & Stewart, 2019; Lee, 2015; Y. Liu et al., 2016; Malik & Zhang, 2015; Z. Wang et al., 2014, 2015; Zhang et al., 2015). Solar cell-based SWIPT technology aims to achieve fully self-powered electronic devices to decouple their dependence on cumbersome and costly battery maintenance service (Fan & Leon-Salas, 2017). Recent progresses in direct bandgap solar cells (e.g., III-V solar cells) have made the cell's efficiency approach to the Shockley-Queisser limit, a theoretical value reflecting the only loss mechanism from the radiative recombination (William & Hans, 1961). High-efficiency solar cells tend to be good emitters due to the enhanced radiative recombination process (Miller et al., 2012). Direct bandgap solar cells, such as GaAs and CdTe, demonstrated strong luminescent emissions with a peak in the infrared spectrum (Raguse & Sites, 2015). Additionally, the cell's luminescent

intensity varies as the cell's terminal voltage changes (Rau, 2012; Schick, Daub, Finkbeiner, & Wurfel, 1992). Therefore, the solar cell can be employed to transmit information optically when modulating its terminal voltage (Leon-Salas & Fan, 2018). The three different operation modes of GaAs or CdTe solar cells (i.e., energy harvesting, reception and transmission of information) demonstrate tremendous potentials when used as an optical antenna.

3.3.2 Luminescent Emissions of Solar Cells

Leon-Salas and Fan (2018) experimentally captured both strong photoluminescent (PL) and electroluminescent (EL) emissions in infrared from a GaAs single junction solar cell (Alta Devices). Both luminescent emissions are generated as a result of radiative recombination inside the solar cell. However, electroluminescence (EL) is stimulated by an applied external electric field, while photoluminescence (PL) is stimulated by external light.

The EL process occurs when injected electrons generated by an external source move to the valence band and recombine radiatively with holes. Therefore, solar cells produce EL emission when they are stimulated by a certain current in direct bias. Direct bandgap solar cells, such as GaAs solar cells, demonstrate stronger EL emission than indirect bandgap counterparts (Williams & Hall, 1978). **Figure 20** shows a GaAs solar cell being stimulated by a red flashlight (b) and being stimulated by a voltage source (c). The luminescent response of the solar cell was captured with a full-spectrum camera.

The PL process begins when the solar cell absorbs photons and generates electron-hole pairs. Then, electrons and holes move to the conduction band and valence band, respectively. After some time, electrons in the conduction band fall back to the valence band and recombine with holes, generating photons with energy matching the cell's bandgap, i.e., E_g (Williams & Hall, 1978). Leon-Salas and Fan (2018) demonstrated both strong and weak PL emissions when the cell's terminal is under open and short conditions, respectively. The experiment validated the use of luminescent radiation from a solar cell (e.g., PL or EL) for digital optical communications.

Leon-Salas and Fan (2019b) developed a circuit model for the luminescent emission process in a solar cell, as illustrated in **Figure 21**. Both theoretical analysis and experimental results demonstrated an exponential relationship between the luminescent radiant flux Φ_{lum} and the cell's terminal voltage V_d , formulated as (Leon-Salas & Fan, 2019b):

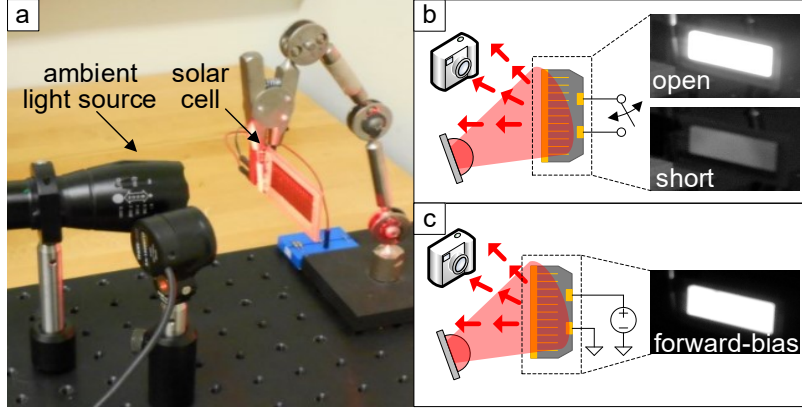


Figure 20. Experiments showing luminescent emissions from a solar cell. a) The real experiment setup; b) Demonstrated PL emission when the cell was under both open circuit and short circuit conditions; c) Demonstrated EL emission when the cell was biased by an external power source with an output of 1.05 V (Leon-Salas & Fan, 2018).

$$\Phi_{lum} = \eta \kappa R \left(QE(\lambda_i) \Phi_{in} - \frac{E_{ph}^e}{q} + \frac{E_{ph}^e I_s e^{V_D/nV_T}}{q} \right)$$

Equation 6. The relationship between Φ_{lum} and V_d .

where, η is the fraction of photons generated inside the solar cell that escape the solar cell, κ is the fraction of the recombined electrons that recombine radiatively, R is the fraction of the photo-generated electrons that recombine inside the solar cell and do not contribute to the current, $QE(\lambda_i)$ is the quantum efficiency at the wavelength of λ_i , q is the electron's charge, E_{ph}^e is the energy of a photon that is generated in the solar cell, I_s is the reverse saturation current, n is the diode ideal factor, and V_T is the thermal voltage.

The solar cell generates PL emissions if the cell's terminal voltage V_{sc} is less than or equal

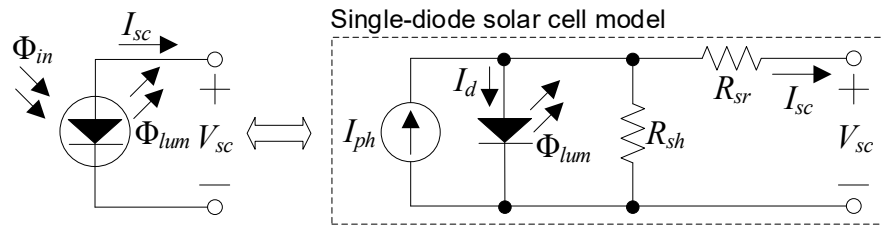


Figure 21. A circuit model for the luminescent emission process in a solar cell (Leon-Salas & Fan, 2019a).

to its open-circuit voltage V_{oc} . In this case, the cell operates in the photovoltaic region and supplies power to external loads. The EL emission occurs when $V_{sc} > V_{oc}$. As a result, the solar cell consumes power from an external supply.

As indicated by the relationship between the luminescent, radiant flux and the cell's terminal voltage, both digital and analog modulation techniques can be employed to modulate the luminescence emissions. Leon-Salas and Fan (2019a) have proposed a circuit, based on a step-up DC-DC converter, to modulate the cell's PL emission. The circuit supports digital modulations in which the cell can be modulated either in between open-circuit (OC) and short-circuit (SC) conditions or in between the maximum power point (MPP) and OC conditions. The circuit also supports analog modulations since the intensity of PL emission varies with the duty cycle of the DC-DC converter. Leon-Salas and Fan (2019a) successfully generated eight distinguishable luminescent levels, with each level representing three binary bits.

3.3.3 Simultaneous Information and Power Reception Circuit for OFID Tags

The circuit for simultaneous information and power reception (SIPR) consists of two basic subcircuits: the energy harvester and the receiver.

The energy harvester, based on a step-up DC-DC converter, converts a low-voltage input to a high-voltage output. The harvester ideally fits in solar-powered electronic applications since it boosts up the low-voltage output from a solar cell (e.g., 0.3 V to 0.7 V) to a few volts, accepted by most of the integrated circuits. Although some efforts have been taken to stack up multiple cells in order to boost up the voltage (Bialic et al., 2015; Y. Liu et al., 2016), the output is unstable due to varied ambient light and load impedance. Therefore, the use of energy harvester becomes important in energy harvesting applications. Additionally, the harvester can bias the solar cell at its maximum power point (MPP) using a variety of maximum power point tracking (MPPT) algorithms (Aquib, Jain, & Agarwal, 2020; Pillai, Rarn, Ghias Mahmud, & Rajasekar, 2020; Selvakunar, Madhusmita, Koodalsamu, Simon, & Sood, 2019; Subuhi & Pradhan, 2019). Consequently, the extraction of maximum power from a solar cell becomes independent of ambient light intensity and load impedance.

Fan and Leon-Salas (2017) proposed a circuit that simultaneously receives power and data from a solar cell. Data is received using a current sense resistor, placed in front of an inductive-boost DC-DC converter (see **Figure 22**). The converter transfers harvested power from

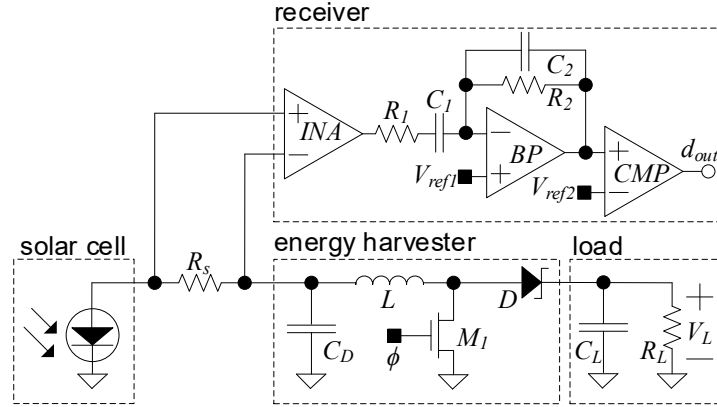


Figure 22. A simultaneous information and power reception circuit (SIPR) proposed by Fan and Leon-Salas (2017).

a silicon solar cell (ANY SOLAR Ltd KXOB22-12X1L) to a load R_L via the inductor L . The power harvesting process involves two phases, determined by the switching state of M_1 . When M_1 is on, the inductor and the capacitor C_D are charged. When M_1 is off, energy stored in the inductor is transferred to R_L . M_1 is modulated by a PWM signal for the periodic power transferring. The duty cycle of the PWM signal determines the equivalent input impedance of the converter and therefore the cell's operation point (Leon-Salas & Fan, 2019a). If the received optical power changes, the duty cycle can be adjusted to keep the cell operating at its maximum operating point (MPP). The switching action of M_1 generates current ripples, interfering with received signals. The value of C_D introduces a trade-off between the strength of switching ripples and the circuit bandwidth. A large C_D reduces the switching ripples, but it also reduces the circuit bandwidth. The energy harvester draws the most power from the solar cell when the load voltage V_L reaches its maximum. In this case, the harvester's power efficiency η_{eh} is given by:

$$\eta_{eh} = \frac{V_L^2}{R_L V_{mpp} I_{mpp}}$$

Equation 7. Power efficiency of the energy harvester.

where, V_L is the voltage at the load, R_L is the load impedance, and V_{mpp} and I_{mpp} are the cell's voltage and current at the MPP, respectively.

The receiver consists of an INA, an active band-pass filter, and a comparator for the A/D conversion. The INA amplifies the current that flow through the current sense resistor, R_s , and outputs a proportional voltage signal. The band-pass filter attenuates the ripple noise introduced

by the switching action of the energy harvester and DC noise induced by an ambient source (e.g., an office fluorescent lamp). The comparator converts the analog signal to a digital signal using the thresholding technique.

When a solar cell is loaded with an external circuit, received information can be extracted using either cell's output current (Fan et al., 2019; Fan & Leon-Salas, 2017; Leon-Salas & Fan, 2018, 2019b) and cell's output voltage (Z. Wang et al., 2014, 2015; Zhang et al., 2015). **Figure 23** shows the small-signal equivalent circuit of a loaded solar cell. As illustrated in the figure, a sense resistor is inserted between the cell and the load to extract information from the cell's output current i_{sc} . The resistor is not required when sensing information using the cell's terminal voltage v_{sc} . As proposed in (Leon-Salas & Fan, 2019b), the diode in the cell's model can be replaced by an equivalent resistor r_d after expanding the diode equation using Taylor series. r_d is given by:

$$r_d = \frac{nV_T}{I_s e^{\bar{V}_{sc}/nV_T}}$$

Equation 8. Expression for the equivalent resistor r_d .

where, I_s is the reverse saturation current, n is the quality factor, V_T is the thermal voltage, and \bar{V}_{sc} is the DC operating point of the cell's terminal voltage. Parameters in the solar cell model can be extracted from measured I-V curves using the curve fitting technique (Ghosh, Wang, & Leon-Salas, 2014). An experiment was carried out to extract solar cell's model parameters under a certain light condition. In the experiment, a far-red LED (Cree XPEBFR) with an emission wavelength of 720 nm was used to illuminate a GaAs solar cell that was located at a distance of 50 cm. The solar cell received an optical power density of 3.45 mW/cm², measured using an optical power meter (Thorlabs S120C). Accordingly, the I-V characteristics curve of the illuminated solar cell was recorded using a source meter (Keithley 2041). **Figure 24** shows the

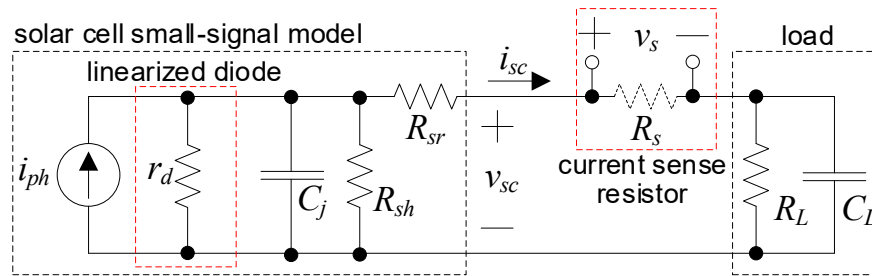


Figure 23. Small-signal model of a loaded solar cell.

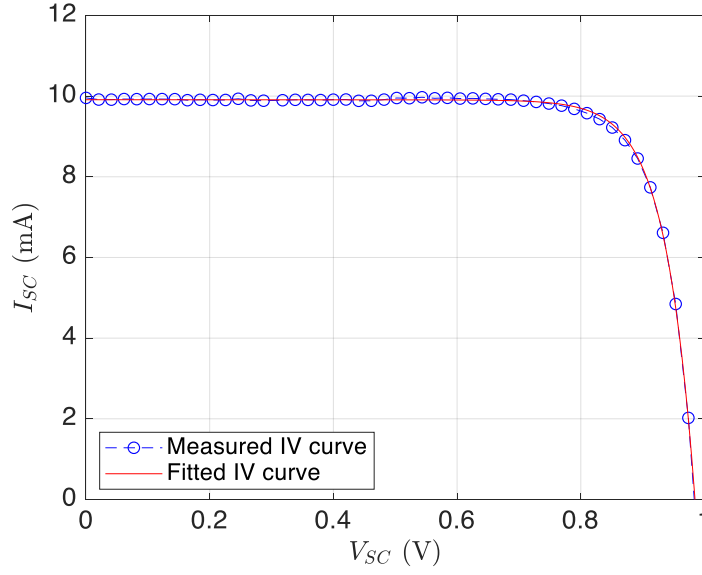


Figure 24. Measured and fitted IV curve of a GaAs solar cell.

Table 2. Model parameters of the GaAs solar cell

Model parameter name	Value
I_{ph}	10.1 mA
R_{sh}	9.206 k Ω
R_{sr}	0 Ω
n	1.847
I_s	0.01 nA
V_{mpp}	0.851 V
I_{mpp}	9.4 mA

measured and fitted I-V curves of a GaAs solar cell used for this study. **Table 2** shows the fitted solar cell model parameters. Since the IV measurement was carried out using DC sweeping technique, the impact of the junction capacitance C_j on results is neglected and cannot be measured (Moayeri Pour et al., 2014). The value of C_j can be estimated using the time-domain technique proposed by Kumar, Suresh, and Nagaraju (2003).

A numerical analysis has been carried out to compare responses of solar cell's terminal voltage and current to an input signal when the cell is biased at MPP (Kadirvelu et al., 2021).

Two transfer functions, including $H_1 = \frac{i_{sc}}{i_{ph}}$ and $H_2 = \frac{v_{sc}}{i_{ph}}$:

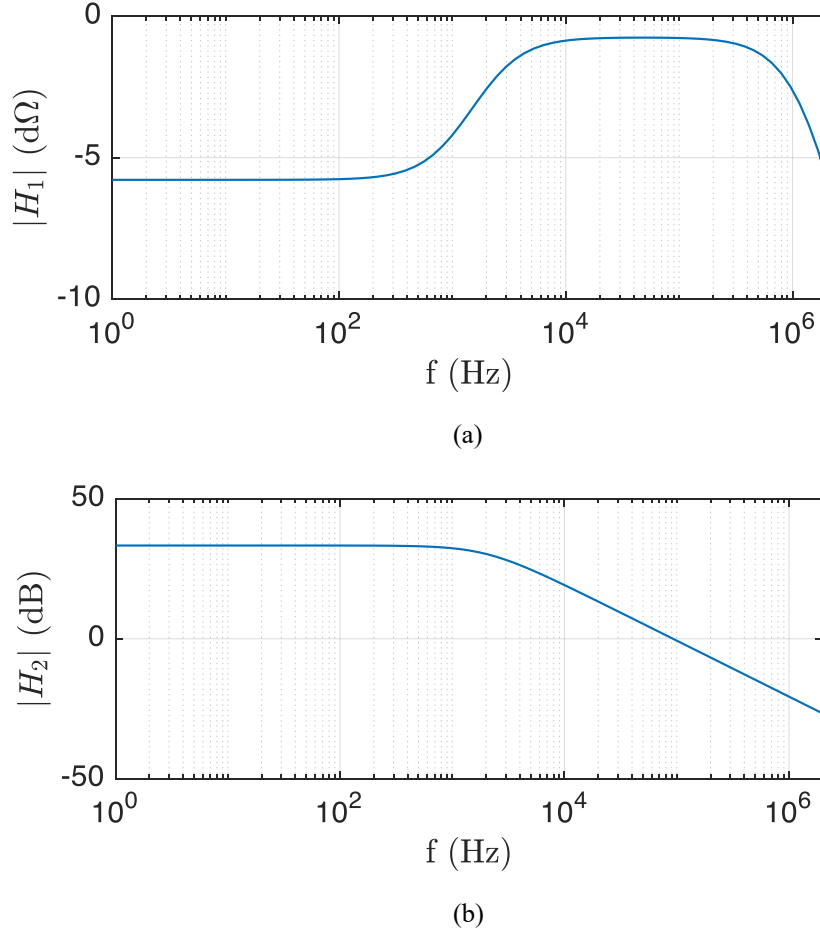


Figure 25. Magnitude plots of transfer function $H_1 = \frac{i_{sc}}{i_{ph}}$ and $H_2 = \frac{v_{sc}}{i_{ph}}$.

$$H_1 = \frac{Z_d}{Z_d + Z_L}$$

Equation 9. The frequency response of $\frac{i_{sc}}{i_{ph}}$.

$$H_2 = \frac{Z_d Z_L}{Z_d + Z_L}$$

Equation 10. The frequency response of $\frac{v_{sc}}{i_{ph}}$.

where, $Z_d = R_{sh} || r_d || 1/sC_j$, $Z_L = R_L || 1/sC_L$, and $s = j2\pi f$ (with f being the frequency in Hz).

Figure 25 shows the magnitude plot of these two transfer functions for cell's model parameters in **Table 2**, $V_{sc} = V_{mpp} = 0.851$ V, $C_j = 798$ nF and $C_L = 10$ μ F. Notably, the transfer function H_1 demonstrates a much wider pass-band compared to H_2 . The same conclusion was also drawn

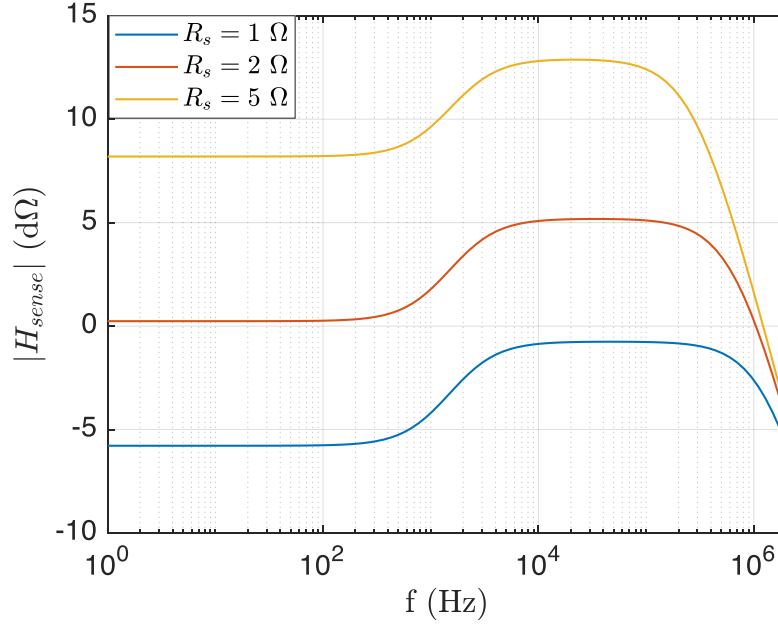


Figure 26. The magnitude plot of the transfer function H_{sense} under different R_s for cell's model parameters in **Table 2**. $V_{sc} = 0.851$ V, $C_j = 798$ nF, $R_L = 90.5$ Ω and $C_L = 10$ μ F.

from (Kadirvelu et al., 2021). Due to the wide pass-band feature of H_1 , this research work uses the cell's output current to extract received information. As illustrated in **Figure 23**, a current sense resistor R_s is employed to sense a received signal. The transfer function $H_{sense} = v_s/i_{ph}$ can be derived (Kadirvelu et al., 2021):

$$H_{sense} = \frac{Z_d R_s}{Z_d + R_{sr} + R_s + Z_L}$$

Equation 11. The frequency response of v_s/i_{ph} .

The impact of circuit parameters, such as R_s , R_L , and C_L , on the transfer function H_{sense} is evaluated using **Equation 11**. **Figure 26** shows the transfer function H_{sense} under different values of R_s . Apparently, the pass-band gain increases with the value of R_s but at the expense of reduced bandwidth. Kadirvelu et al. (2021) suggested the small value of R_s as it reduces the dissipated power. **Figure 27** shows the transfer function H_{sense} for different values of C_L . Even if a larger value of C_L boosts up the pass-band gain for a certain frequency range, the circuit's bandwidth reduces accordingly. Additionally, the value of C_L reveals a trade-off between the harvested power and bandwidth for the circuit proposed in Fan and Leon-Salas (2017). **Figure 28** plots the transfer function H_{sense} for three different value of the external load R_L . R_L is

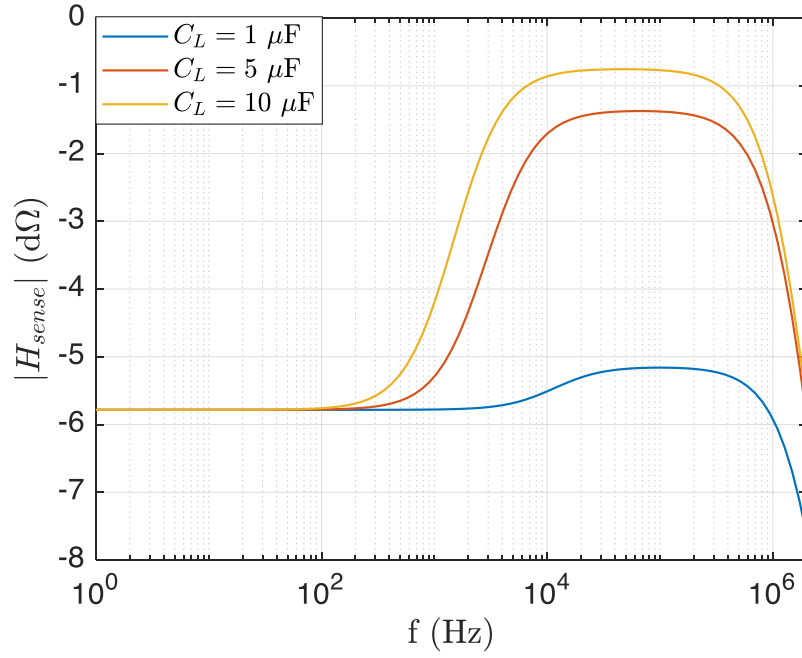


Figure 27. The magnitude plot of the transfer function H_{sense} under different C_L for cell's model parameters in **Table 2**, $R_s = 1 \Omega$, $V_{sc} = 0.851 \text{ V}$, $C_j = 798 \text{ nF}$, and $R_L = 90.5 \Omega$.

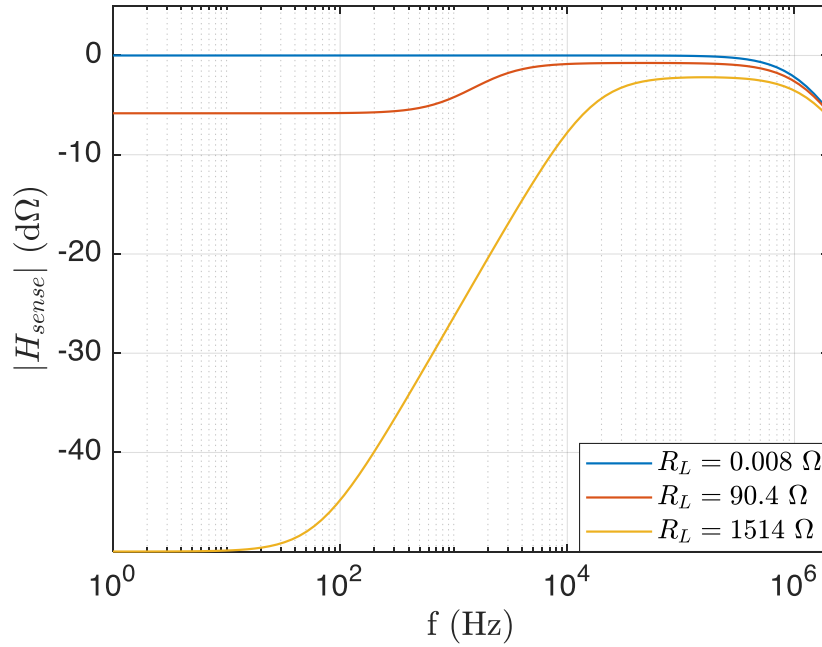


Figure 28. The magnitude plot of the transfer function H_{sense} under different R_L for cell's model parameters in **Table 2**, $R_s = 1 \Omega$, and $C_j = 798 \text{ nF}$. V_{sc} varies with R_L .

selected purposely so that the solar cell works at the short-circuit ($R_L = 0.008 \Omega$), maximum power point (MPP) ($R_L = 90.5 \Omega$), and open-circuit ($R_L = 1514 \Omega$) conditions, respectively. As illustrated in the figure, the pass-band gain reduces as the load value increases. Although the pass-band gain reduces by the maximum of -6 dB for the MPP condition, the solar cell maximizes the harvested energy, providing the best trade-off for energy harvesting applications.

3.3.4 Luminescence Modulator Circuits

As explained in section 3.3.2, high-efficiency solar cells (e.g., GaAs and CdTe) emit strong luminescence under external stimuli. The EL emission is stimulated by an external current, while the PL emission is excited by an external optical source. For an OFID application, the use of PL and EL is determined by the strength of optical excitation. If the PL emission is strong enough to cover a certain communication range, it is used as the main information carrier. However, if the PL emission is not strong enough to support the required communication range, the EL emission is used instead.

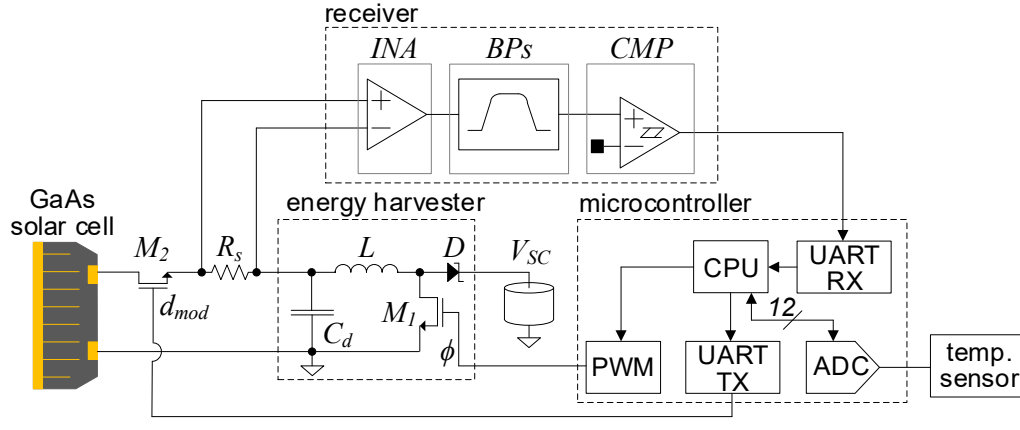
Leon-Salas and Fan (2019b) proposed two photo-luminescence modulation circuits based on an inductive-boost DC-DC converter. The first modulator (Modulator 1) employs a N-channel MOSFET M_2 in front of the boost DC-DC converter. M_2 connects and disconnects the converter from the solar cell according to a binary bit stream d_{mod} .

The second modulator (Modulator 2) uses an AND gate to mix the bit stream d_{mod} and the PWM signal ϕ from a pulse width modulator. When $d_{mod} = 1$, the AND gate outputs ϕ , which bias the operating point of the solar cell to the MPP. When $d_{mod} = 0$, the AND gate outputs a 0, disables the converter.

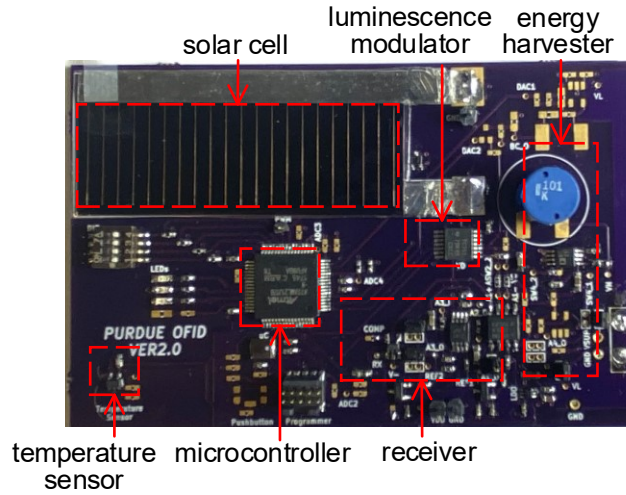
As for the normal operation of two circuits, Leon-Salas and Fan (2019b) suggested the bit rate to be lower than the frequency of the PWM signal ϕ . Experiments results showed that Circuit 2 harvested more power than Circuit 1. However, the swing of PL emission in Circuit 1 is larger, resulting in a higher signal-to-noise (SNR) at a reader.

3.3.5 A Microcontroller-based OFID Tag for Temperature Sensing

The first OFID tag design was introduced in (Fan et al., 2019) for remote temperature sensing applications. The tag performs multiple tasks, including energy harvesting, data



(a) Schematic



(b) Photograph

Figure 29. The circuit diagram and photograph of the proposed OFID tag.

transmission/reception, and temperature sensing. **Figure 29** shows both the circuit diagram and photograph of this OFID tag. The tag consists of several functional hardware modules, such as an energy harvester, a data receiver, a microcontroller, and an analog temperature sensor. The energy harvester, based on a boost DC-DC converter, took the design conceived in (Fan & Leon-Salas, 2017). In the harvester, the switch M_1 is controlled by a PWM module in the microcontroller. The receiver contains one instrumentation amplifier, two active band-pass filters, and one comparator. A simple receiver design minimizes its power consumption while providing sufficient computing power for the signal processing and analog-to-digital (A/D) conversion. The use of the current sense resistor R_s demonstrates an improved system bandwidth

which is proportional to the ambient temperature. An analog-to-digital (ADC) converter in the microcontroller digitizes the analog output from the temperature sensor. Information was encoded in several data packets that were then transmitted back to a reader using the PL emission. The on-off keying (OOK) technique was used for the communication between the tag and reader. In the microcontroller, information was encoded and decoded using the UART module.

3.3.6 An FPGA-based OFID Module for Sensing Applications

Our second tag design used an FPGA-based OFID module to support a wide range of low-power IoT sensing solutions. The module, implemented on a 20 mm x 15 mm PCB board, includes several core features, such as energy harvesting, data transmission/reception, cold startup, power management, data processing, and logic control. When interfacing the OFID module with external hardware components, such as a GaAs solar cell, an energy reservoir (e.g., a battery or a supercapacitor), and some peripheral electronics, a fully functional OFID tag can be implemented. **Figure 30** shows both the schematic and photograph of the proposed OFID module. The OFID module consists of a power management unit, a data receiver, a 12-bit ADC, an FPGA, a PL modulator, and an EL modulator.

3.3.6.1 Power Management Unit

In an OFID module, the power management unit consists of an energy harvester (Analog Devices ADP5090), capable of harvesting power from the solar cell to the power reservoir, and a multi-channel buck converter (Maxim MAX17270), providing two voltage levels (e.g., 3.3 V and 1.2 V). The energy harvester, with its architecture illustrated in **Figure 31**, contains the following features that are essential to an OFID tag (Analog Devices, 2014): 1) inductive-boost converter with a fractional open-circuit voltage maximum power point tracking (MPPT) algorithm; 2) a typical quiescent current in hundreds of nanoamps for ultra-low-power applications; 3) minimum input voltage of 80 mV; 4) cold startup with an internal charge pump; 5) programmable output voltage control for overcharging and overdischarging protections; 5) shutdown control using an external digital controller (e.g., a microcontroller). As shown in **Figure 31**, the energy harvester consists of several internal subcircuits such as a charge pump, an

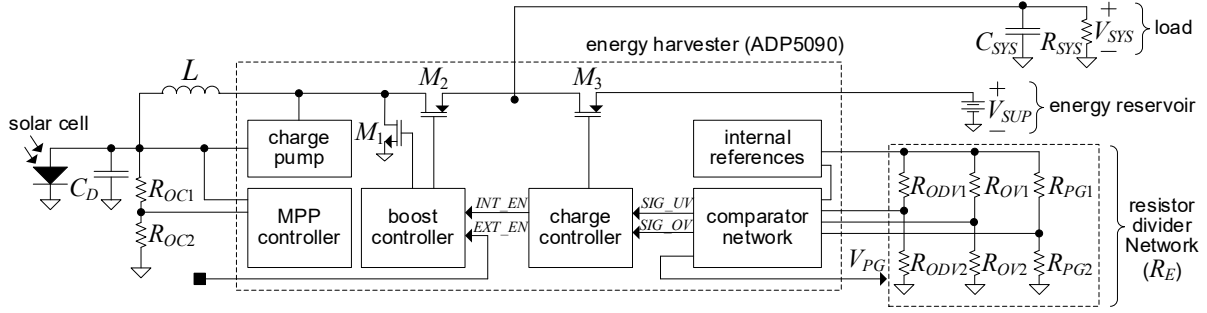


Figure 31. The schematic diagram of the energy harvester ADP5090

MPP controller, a boost controller, a charge controller, internal references, and comparators.

The charge pump is automatically enabled when its input voltage is above 380 mV, and the voltage at the energy reservoir is below 1.93 V. To complete the cold startup, the solar cell must generate sufficient power that compensates for the loss during this process. The time period for the cold startup depends on the available optical power at the solar cell and power losses in the energy harvester, energy reservoir, and external load. In order to reduce the cold startup period, we can either select the energy reservoir with low internal losses or operate the load in the shutdown mode.

Both the boost controller and charge controller are enabled once the energy harvester completes the cold startup process. The boost controller controls switches M_1 and M_2 in the pulse frequency mode (PFM), transferring power from the solar cell to the energy reservoir. To extract nearly maximum power from the cell, the boost controller and MPP controller form a control loop that sets the cell's voltage to the fraction of the cell's open-circuit voltage. The use of fractional open-circuit maximum power point algorithm relies on the fact that the cell's voltage at MPP shows a linear dependence with respect to the open-circuit voltage for different optical and temperature levels. The fractional factor is typically 0.7 - 0.8, depending on characteristics of solar cells (Ahmad, 2010).

The MPP controller samples the cell's open-circuit voltage at a time interval of 19 seconds during which the boost controller is disabled. The sampled open-circuit voltage is used to determine the cell's MPP voltage, temporarily stored in an external capacitor after each sampling event. The MPP voltage V_{MPP} is configured using an external voltage divider and is given by:

$$V_{MPP} = V_{OC} \left(\frac{R_{OC2}}{R_{OC1} + R_{OC2}} \right)$$

Equation 12. The MPP voltage V_{MPP} calculation.

The charge controller provides protection against overcharging or overdischarging the energy reservoir. When the voltage at the energy reservoir V_{SUP} exceeds the overcharging voltage, the charge controller disables the boost controller. When V_{SUP} drops below the overdischarging voltage, the charge controller disables the switch M_3 and prevents a deep discharge of the energy reservoir. Both overcharging and overdischarging protection voltages are configurable via an internal comparator network and external voltage dividers. The overcharging voltage V_{OV} and overdischarging voltage V_{ODV} are determined by (Analog Devices, 2014):

$$V_{OV} = \frac{3}{2} V_{REF} \left(1 + \frac{R_{OV1}}{R_{OV2}} \right)$$

Equation 13. The overcharging voltage V_{OV} calculation.

$$V_{ODV} = V_{REF} \left(1 + \frac{R_{ODV1}}{R_{ODV2}} \right)$$

Equation 14. The overdischarging voltage V_{ODV} calculation.

where V_{REF} is an internal reference voltage with a value of 1.21 V. The charge controller also monitors V_{SUP} and set/reset a power good (PG) signal V_{PG} when V_{SUP} reaches pre-defined thresholds (e.g., upper threshold and lower threshold). The PG signal is used to enable or disable the load. Both upper threshold $V_{SUP_UP_THR}$ and lower threshold $V_{SUP_LO_THR}$ are programmable via an external voltage divider and are given by (Analog Devices, 2014):

$$V_{SUP_UP_THR} = V_{REF} \left(1 + \frac{R_{PG1}}{R_{PG2}} \right)$$

Equation 15. The upper threshold voltage $V_{SUP_UP_THR}$ calculation.

$$V_{SUP_LO_THR} = V_{HI_THR} \frac{R_{PG_SYS}}{R_E}$$

Equation 16. The lower threshold voltage $V_{SUP_LO_THR}$ calculation.

where, V_{REF} is the internal reference voltage with a value of 1.21 V, R_{PG1} and R_{PG2} are resistors in the voltage divider, R_{PG_SYS} is the internal resistor with a value of 103.5 k Ω , and R_E is the equivalent resistance of the voltage divider network (see **Figure 31**).

The multi-channel buck converter, directly interfaced with the energy harvester (see **Figure 30a**), provides two voltage levels (e.g., 3.3 V and 1.2 V) required by other electronics.

The buck converter is enabled or disabled by the PG signal from the energy harvester. When the buck converter is enabled, it transfers power from the energy reservoir to other hardware modules, such as receiver, FPGA, and peripheral electronics. When the buck converter is disabled, it stops the power transfer to prevent the energy reservoir being depleted.

3.3.6.2 Receiver

A current sense resistor R_s , placed between the energy harvester and the solar cell, senses the received signal in a form of current and converts it to a voltage difference, further processed by the receiver. The receiver, made of an INA, two active first-order band-pass filters, and a comparator. The INA contains two ultra-low power operational amplifiers (Maxim Integrated MAX40006). The gain of INA G_{ina} is determined by (Analog Devices, 2009):

$$G_{ina} = 1 + \frac{R_1}{R_2}$$

Equation 17. The gain of INA G_{ina} calculation.

The band-pass filter, based on two identical first-order active band-pass filters, consisting of two operational amplifiers (Maxim integrated MAX40006) and peripheral resistors and capacitors. The transfer function of this filter is $H_{bp} = H_{bp1} \times H_{bp2}$. Both H_{bp1} and H_{bp2} are given by (Kadirvelu et al., 2021):

$$H_{bp1} = H_{bp2} = \frac{-A(s)(R_4 \parallel 1/sC_2)}{(1 + A(s))\left(R_3 + \frac{1}{sC_1}\right) + R_4 \parallel 1/sC_2}$$

Equation 18. The transfer function of the band-pass filter H_{bp} .

where, $A(s)$ is the open-loop transfer function of the op amp. The upper and lower frequencies (e.g., f_{upper} and f_{lower}) of each band-pass filter are given by:

$$f_{upper} = \frac{1}{2\pi R_3 C_1}$$

Equation 19. The upper corner frequency calculation.

$$f_{lower} = \frac{1}{2\pi R_4 C_2}$$

Equation 20. The lower corner frequency calculation.

Two corner frequencies reduce noise present in the receiver while providing sufficient bandwidth for communication signals. As experimentally observed and validated in (Leon-Salas & Fan,

2019b), the energy harvester in an OFID tag produces the ripple current which manifests as interference to received signals. Therefore, the filter's upper corner frequency should be lower than the ripple's frequency. Additionally, the lower corner frequency of the filter is set so that it reduces the interference from DC signal and prevents the receiver's output being saturated. The receiver adopts the thresholding technique for the direct A/D conversion as those proposed in (Fan et al., 2019; Fan & Leon-Salas, 2017; Leon-Salas & Fan, 2018, 2019b).

3.3.6.3 Digital Controller

The use of FPGA eases the implementation of the logic control for the tag system and provides enough resources to achieve various digital modulations for optical communications (e.g., OOK, PAM, PPM, and DPIM). Additionally, FPGA is useful in emulating the behavior of a digital system before implementing it on an ASIC (Markovic et al., 2017). An ultra-low power FPGA (Lattice ICE5LP4K) has been selected for the OFID tag. The FPGA contains 3520 look up tables (LUTs), providing enough logic resources for OFID based applications. In the standby mode, the FPGA only consumes around 71 μ A current. Besides the ultra-low power feature and adequate logic resources, the FPGA provides extra hardware resources, including two internal oscillators, two I2C cores, two SPI cores, one DSP block, and 80 kbits block RAMs.

The digital controller of the OFID tag is implemented on the general-purpose FPGA fabric. The digital controller consists of five functional modules, including an I2C module, an DPIM encoder and decoder, and a logic control unit. The I2C module communicates with external ICs, such as I2C based sensors, and a non-volatile memory, i.e., EEPROM. The encoder and decoder process information that are exchanged with the OFID reader. The logic controller provides controls over the power management unit, receiver, and some peripheral electronics, such as switches and LEDs. Additionally, the logic controller schedules events and exchanges information with other FPGA modules.

3.3.6.4 PL and EL Modulator

The proposed OFID tag provides the capability of modulating both photoluminescent (PL) and electroluminescent (EL) emissions. The PL modulator is implemented by adding an NMOS transistor M_1 across terminals of the solar cell (see **Figure 30a**). By modulating M_1 in open and close conditions, information can be transmitted via the modulated PL emission. The

EL modulator consists of a buck converter (Texas Instruments TPS62353) and a PMOS transistor M_2 . The buck converter employs the pulse frequency modulation (PFM) technique to optimize the power efficiency for a light load. The output voltage of the buck converter is programmable with a resolution of 12.5 mV using an I2C interface from 0.75 V to 1.54 V (Texas Instruments, 2008). Featured with an enable pin, the buck converter can be enabled or disabled by the FPGA. During the EL modulation, the switch M_2 connects or disconnects the buck converter with the solar cell according to binary information being transmitted.

3.3.7 Summary

This chapter provided the framework and methodology required to design an OFID system, including an OFID reader and an OFID tag. The OFID system takes advantage of the feasibility of using a direct bandgap solar cell (e.g., GaAs or CdTe) as an optical antenna, capable of harvesting energy as well as establishing a two-way communication link with the reader. Introduced as a new communication technique for energy harvesting applications, the proposed OFID system aims to tackle emerging challenging applications where radio-based energy harvesting solutions are not available. To the author's best knowledge, the concept of using solar cells as an optical antenna for both energy harvesting and two-way communications is proposed for the first time.

CHAPTER 4. RESULTS

This chapter presents various experiments to validate the OFID concept and evaluate system performances of a proof-of-concept OFID communication prototype. The first OFID prototype, reported in (Fan et al., 2019), consists of a dual-aperture OFID reader and a microcontroller-based OFID tag. The second OFID prototype, as an upgraded version to the first one, contains a single-aperture reader and an OFID tag that is powered by an FPGA-based OFID module. Section 4.1 provides experimental evidence that demonstrates the feasibility of using luminescent emission from a GaAs solar cell for optical communication. Section 4.2 compares two photoluminescence (PL) modulator circuits and discusses their performances in energy harvesting and data transmission. Section 4.3 presents experiments and results to validate the first prototype. Section 4.4 experimentally analyzes the second prototype with an emphasis of a single-aperture reader, an FPGA-based OFID module, and their communication performance. The last section concludes the chapter.

4.1 Validation of Luminescent Emissions in a GaAs Solar Cell

A set of experiments were carried out in (Leon-Salas & Fan, 2018) to explore the potential of using solar cell's luminescent emissions for optical communication. The experiment setup consisted of a white LED flashlight, an optical sensor (Thorlabs S120C), a source meter (DIGILENT Explore), a digital CMOS camera (HausBell HDV-5052STR) with a mounted 850 nm long-pass filter, and a single-junction GaAs solar cell (Alta Devices) with a size of 5 cm x 1.7 cm. The distance between the solar cell and flashlight was set to 32.5 cm. During experiments, the solar cell received an illuminance of 6350 lux and generated a photocurrent of 40 mA.

In the first experiment, the digital camera captured strong luminescent emissions from the solar cell (see **Figure 20**). As a result, two conclusions were drawn from experiment results: 1) the solar cell in this experiment demonstrated both strong PL and EL emissions; 2) the solar cell generated two distinguishable PL emission levels when the cell was biased in open-circuit and short-circuit conditions, respectively.

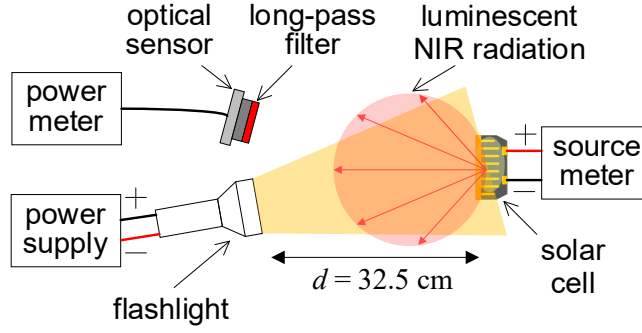


Figure 32. The experimental setup to evaluate the relationship between the luminescent radiant power and the bias voltage across the solar cell.

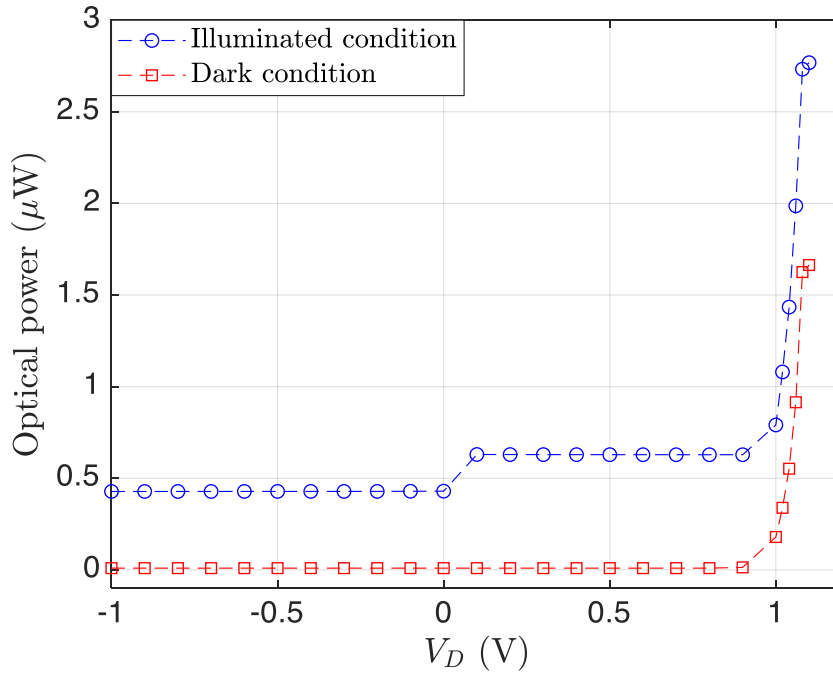


Figure 33. The measured optical power of luminescent emissions when the solar cell was under illuminated and dark conditions.

The second experiment involved demonstrating the relationship between the power level of luminescent emissions and the bias voltage across the solar cell. **Figure 32** shows the experimental setup. The optical sensor was employed to sense the power level of luminescent emissions. An 850 nm long-pass filter was attached to the sensor to remove visible light interference since luminescent emissions are located in the infrared spectral region. The source meter was used to bias the solar cell from -1.0 V to 1.14 V. **Figure 33** shows the measured

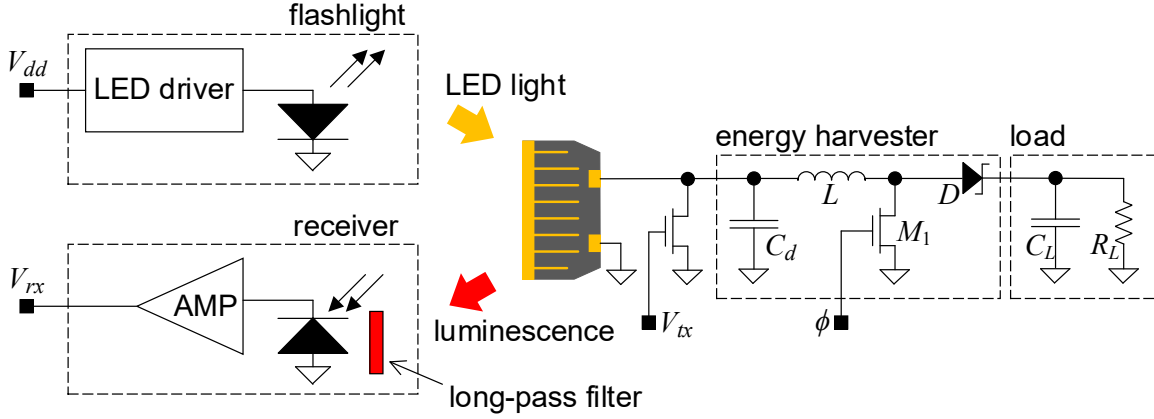


Figure 34. Conceptual diagram of the experiment setup to validate the information transmission via the modulated PL emission.

optical power. Experiment results revealed that the illuminated solar cell generated luminescence across all operation regions, such as the reverse bias region, photovoltaic region, and forward-bias region. In particular, the power level of luminescent emissions increased dramatically when the solar cell was biased close to or in the forward-bias region.

The last experiment demonstrated the feasibility of transmitting information via the modulated PL emission. **Figure 34** shows a conceptual diagram of the experiment setup. The same LED flashlight was used to illuminate the solar cell. A photodiode (Vishay BPW34S), equipped with an 850 long-pass filter, was placed right next to the flashlight to detect optical signals. The solar cell was attached to a boost DC-DC converter, transferring the power from the solar cell to a load. An N-channel MOSFET M_1 was used to modulate the luminescence. In the experiment, the solar cell operated at the short-circuit (SC) condition and maximum power point (MPP) alternatively according to an applied signal (i.e., a 10 kHz PWM signal with the duty cycle of 50 %) at the gate of M_1 . The receiver amplifies an output signal from the photodiode. In order to verify the feasibility of using luminescence to transmit data, the receiver's output signal was captured and compared with the transmitted signal. **Figure 35** shows both transmitted and received signal waveforms. Information can be extracted digitally using either a comparator or an analog-to-digital converter (ADC). As shown in **Figure 35**, the received signal waveforms are in close agreement with the transmitted counterpart when the data rate is low (e.g, 0.5 kbps, and 1 kbps). However, the received waveform starts to get distorted when the data rate is high (e.g., 5 kbps and 10 kbps).

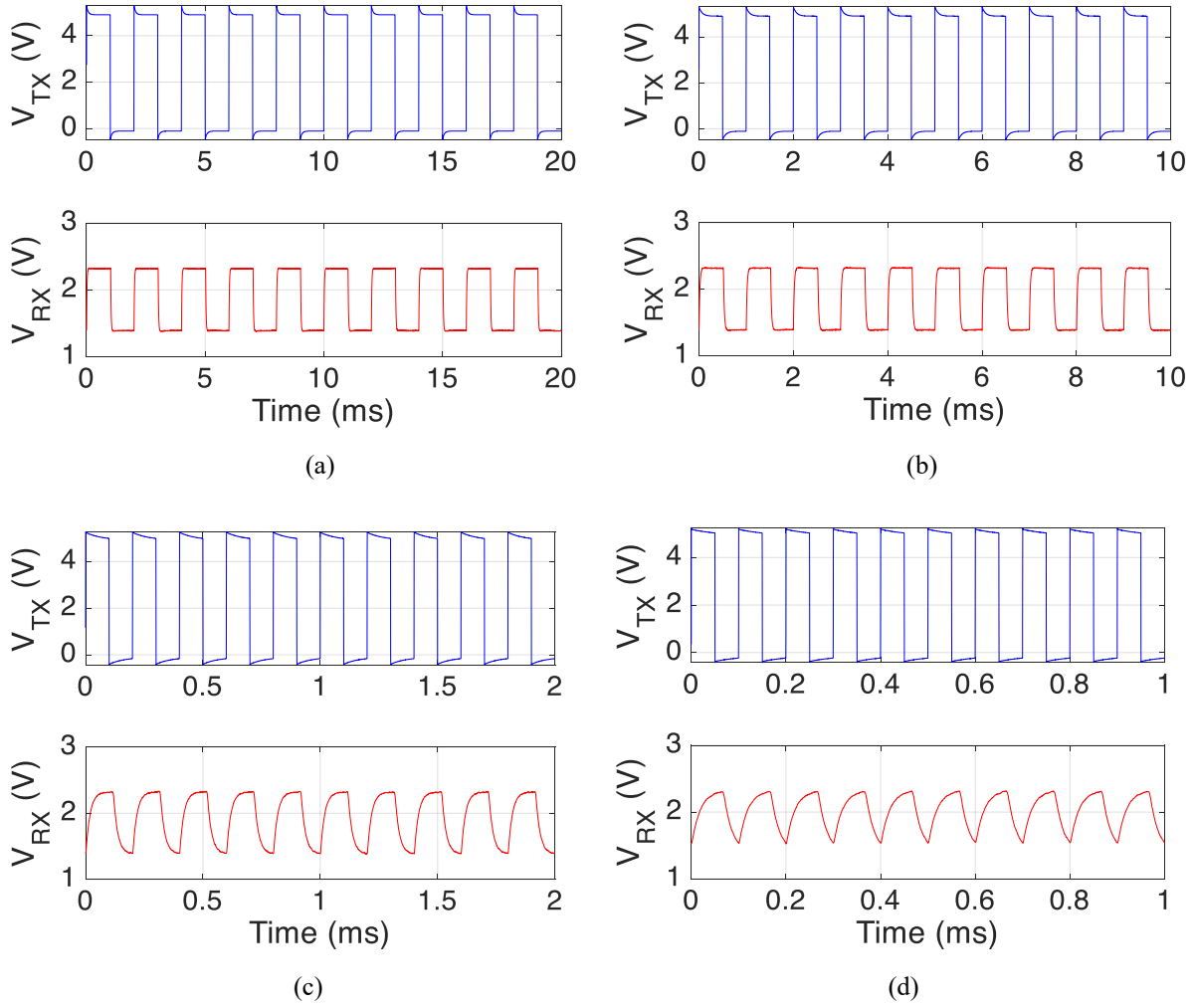
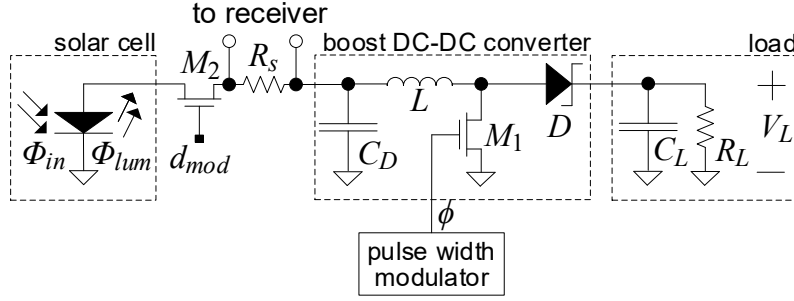


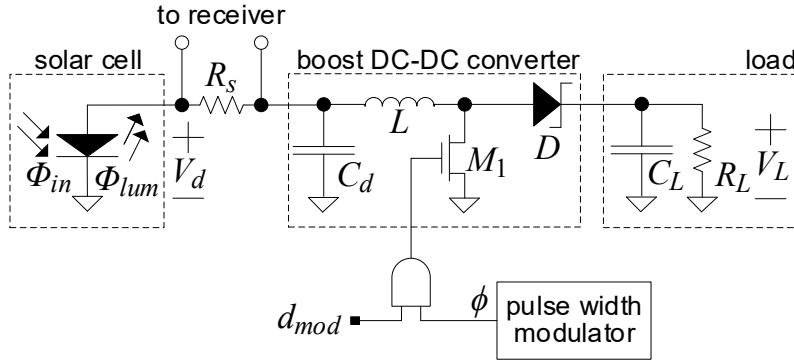
Figure 35. Recorded waveforms at V_{TX} and V_{RX} when data was transmitted at different data rates. (a) 0.5 kbps. (b) 1 kbps. (c) 5 kbps. (d) 10 kbps.

4.2 Comparison of two PL Modulator Circuits

As discussed in (Leon-Salas & Fan, 2019b), two PL modulator & EH circuits (see **Figure 36**) can be integrated into a DC-DC converter-based SWIPT system. Accordingly, experiments were designed to compare their performances regarding energy harvesting and communication. **Figure 37** shows both schematic and a photograph of the experimental setup. The setup employed a 623 nm LED (Cree XPERED), placed inside a focusable flashlight head, a GaAs solar cell from Alta Devices, PL modulator & energy harvesting (EH) circuit, a field programmable gate array (FPGA) board (Altera DE2), a photodiode (Vishay BPW34S) and a receiver circuit. The photodiode was housed in another flashlight head. The receiver contains a



(a) PL modulator & EH circuit 1



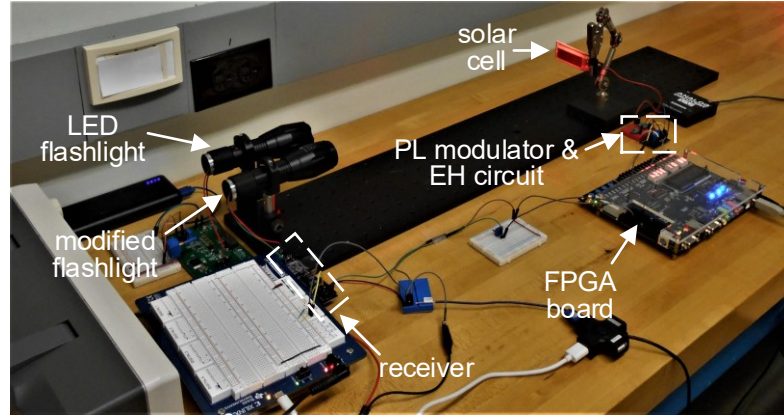
(b) PL modulator & EH circuit 2

Figure 36. Photo-luminescence modulation circuits proposed in (Leon-Salas & Fan, 2019b).

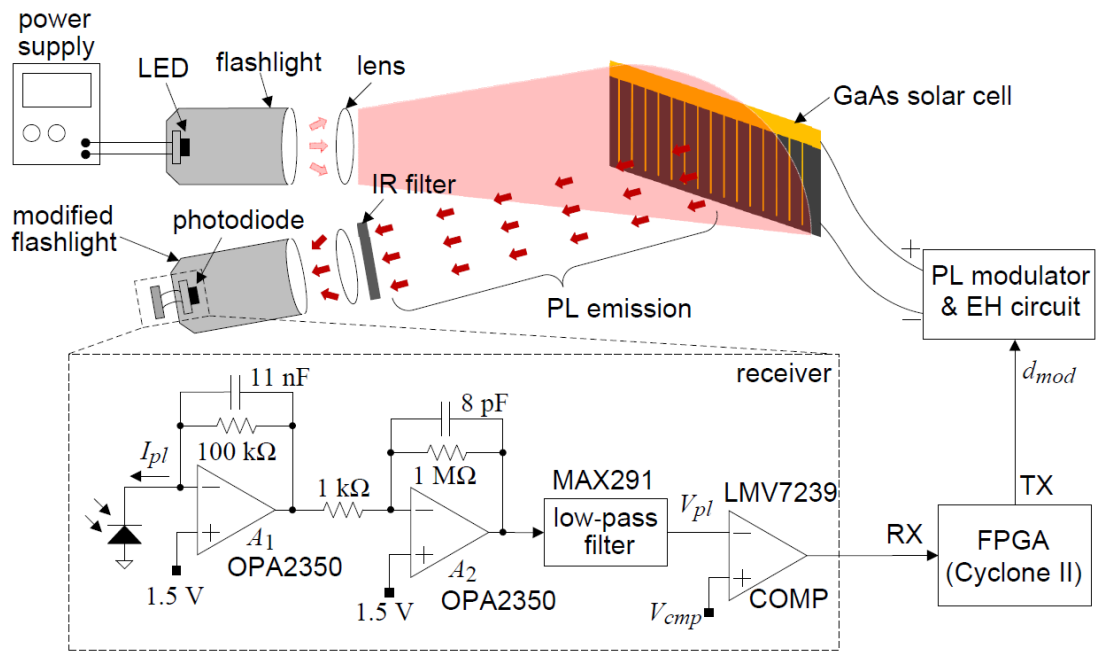
transimpedance amplifier, an inverting amplifier, and an 8th order low-pass filter (MAX291) and provides a trans-impedance gain of $10^8 \Omega$. The FPGA board generates both a PWM signal and a modulation signal d_{mod} for the PL modulator & EH circuits.

The experiment recorded transmitted and received signal waveforms to validate the communication link between the reader and each PL modulator & EH circuit. In the experiment, the solar cell was placed away from the reader at a distance of 51 cm. In order to make a fair comparison between two PL modulator & EH circuits, same circuit parameters were used for both, as shown in **Table 3**.

The signal d_{mod} , comprised of a periodic sequence of alternating '0' and '1', was applied the PL modulator & EH circuit at a data rate of 5 kbps. The symbol '0' means the solar cell is disconnected to the EH circuit (i.e., open-circuit condition), while the symbol '1' represents the solar cell is connected to the EH circuit (i.e., maximum power point). Therefore, both PL modulator & EH circuits featured concurrent energy harvesting and data transmission. The received signal waveform V_{pl} was captured at the output of the low-pass filter MAX291.



(a)



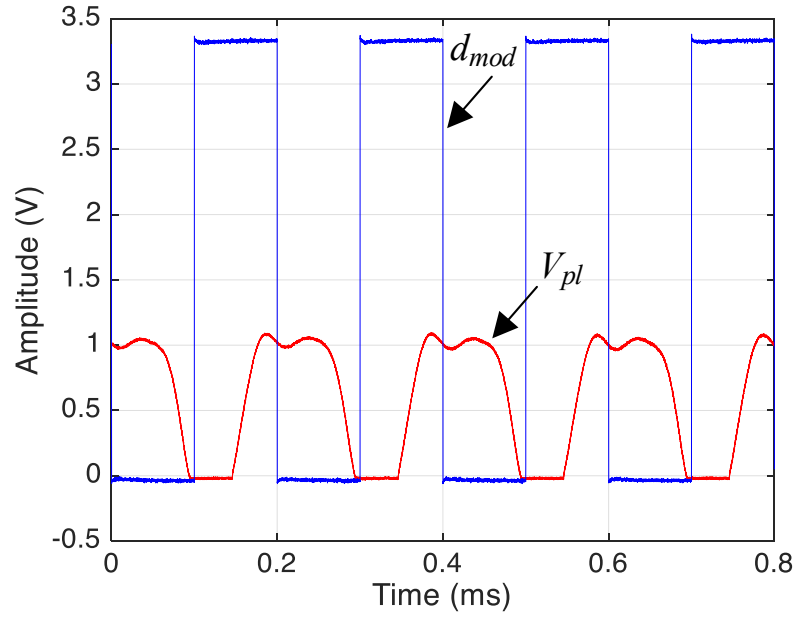
(b)

Figure 37. Photograph and schematic diagram of the experimental setup. (a) photograph of the setup. (b) schematic diagram of the setup (Leon-Salas & Fan, 2019b).

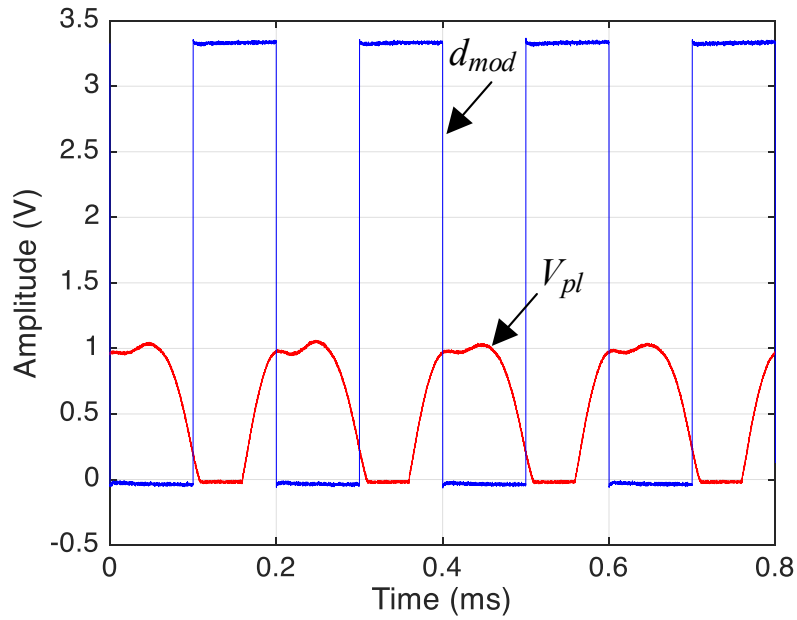
Table 3. Circuit parameters for both PL modulator & EH circuits

Parameter Name	Value
R_L	5.1 k Ω
C_D	1 μ F
L	68 μ H
C_L	10 μ F

Figure 38 shows transmitted and received waveforms for both circuits.



(a)



(b)

Figure 38. Transmitted and received waveforms captured from both PL modulator & EH circuits (see **Figure 36**). (a) PL modulator & EH circuit 1. (2) PL modulator & EH circuit 2.

As illustrated in the figure, the transmitted waveform d_{mod} in both circuits can be reconstructed after thresholding the received waveform V_{pl} . The experiment also compared the maximum

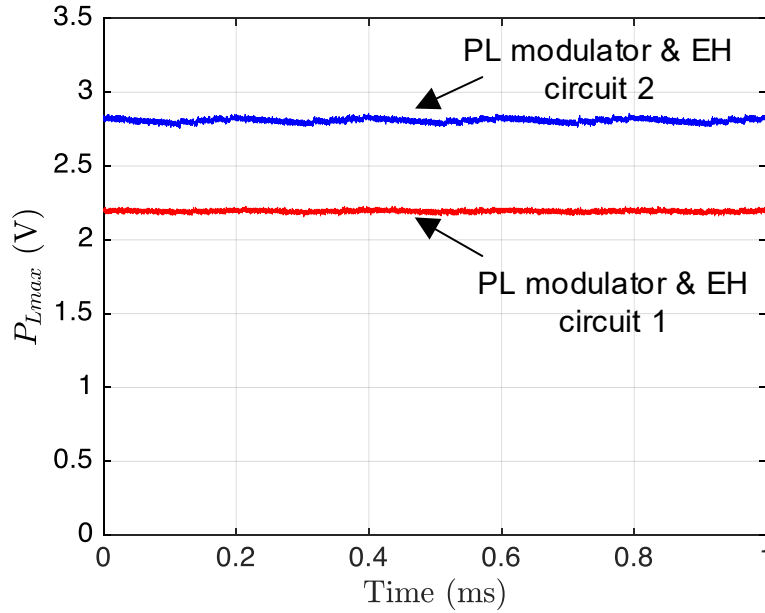


Figure 39. A comparison of the maximum harvested power P_{Lmax} between two proposed PL modulator & EH circuits during data transmission.

harvested power between both PL modulator & EH circuits. The maximum harvested power is given by:

$$P_{Lmax} = \frac{V_L^2}{R_L}$$

Equation 21. The maximum harvested power P_{Lmax} calculation.

where, V_L is the voltage across the load and R_L is the load resistance. Therefore, the maximum harvested power can be derived using the maximum V_L . **Figure 39** shows time waveforms of the maximum harvested power P_{Lmax} when both PL modulator & EH circuits transmitted information. Notably, the PL modulator & EH circuit 2 harvested more power from the solar cell than the PL modulator & EH circuit 1, which can be explained by the following reasons: (1) the capacitor C_D . continued accepting charges from the solar cell even if a '0' was transmitted; (2) the MOSFET M_1 . in the PL modulator & EH circuit 1 consumed power due to its on-resistance.

Another experiment was arranged to evaluate the communication performance of both PL modulator & EH circuits in transmitting information. The bit error rate (BER) was employed as the figure of merit. The distance between both circuits and the reader was adjusted from 12 cm to 70 cm. The FPGA board was employed to generate 10^6 pseudo-random bits at a rate of 15 kbps.

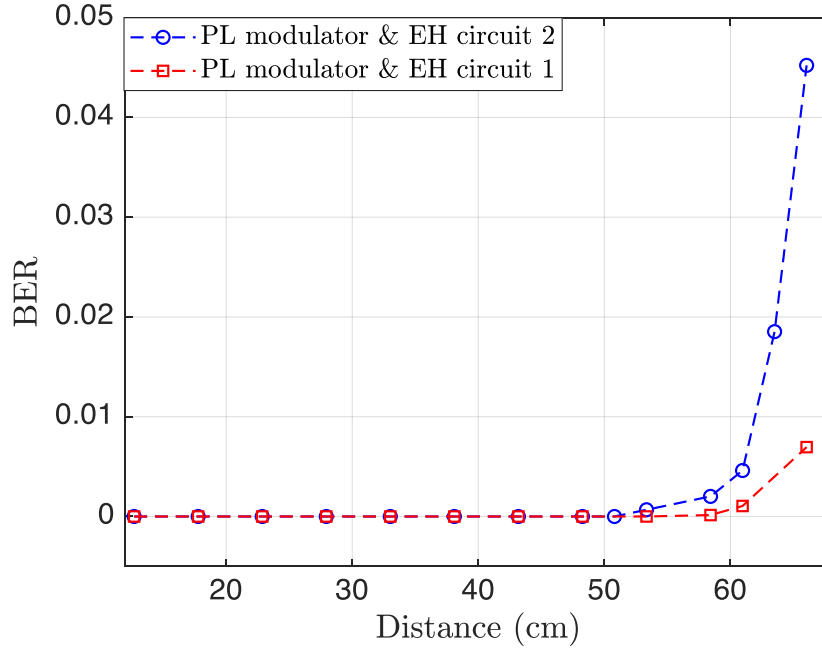


Figure 40. The measured BER versus distance for both circuits.

Accordingly, error bits were screened out by comparing transmitted and received bits in the FPGA. **Figure 40** shows the measured BER versus distance for both circuits. At a communication distance of 53 cm, the PL modulator & EH circuit 2 has a BER of 6.8×10^{-4} while no error bits were present in the PL modulator & EH circuit 1. Beyond the communication distance of 53 cm, the PL modulator & EH circuit 1 still demonstrates lower BER than the PL modulator & EH circuit 2.

4.3 The First OFID System Prototype

The first OFID system prototype was reported in (Fan et al., 2019). The OFID system contained a dual-aperture reader (i.e., the first reader prototype shown in **Figure 11**) and a microcontroller-based OFID tag (i.e., the first tag prototype shown in **Figure 29**). The design of both reader and tag were explained in section 3.2.1 and section 3.3.5, respectively. The OFID system was tested to verify the two-way communication and energy harvesting functionalities.

In order to validate the first tag prototype's capability to harvest ambient energy while transmitting information, the tag was programmed to carry out two tasks: (1) control the energy harvester circuit (i.e., a boost DC-DC converter) to harvest the most power from a GaAs solar

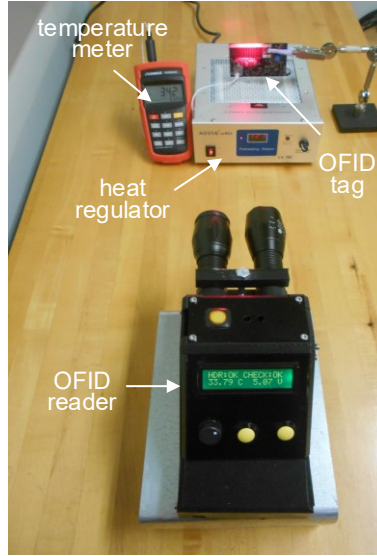


Figure 41. OFID system setup that demonstrated the wireless sensing functionality. The setup contained the first OFID reader prototype and the first OFID tag prototype.

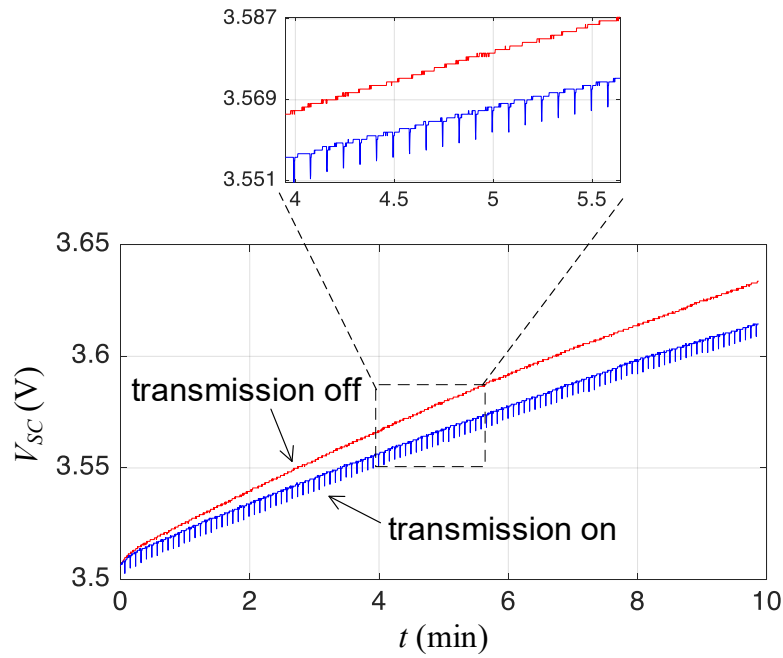


Figure 42. Recorded charging profiles of the tag's supercapacitor with and without the data transmission event.

cell; (2) sense the voltage level at the supercapacitor and ambient temperature and transmitted information back to the reader repeatedly at a time interval of 5 seconds. **Figure 41** shows a

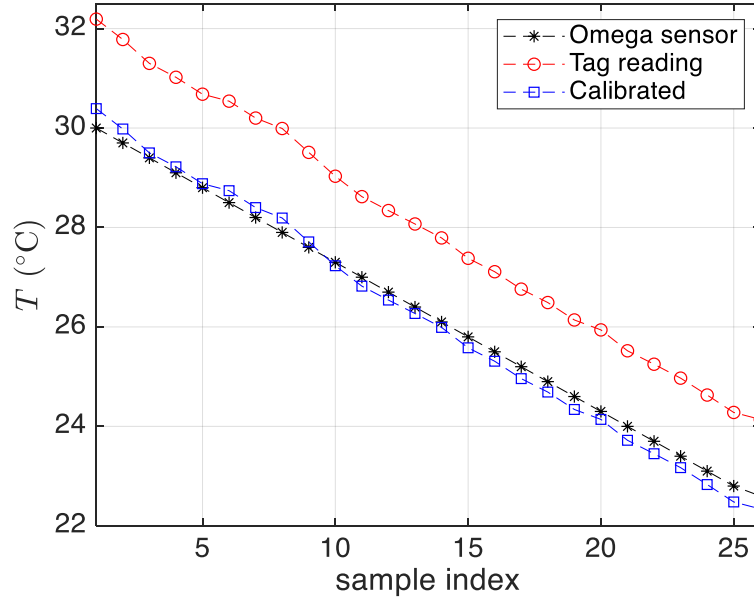


Figure 43. Recorded temperature samples from the temperature meter and OFID reader.

photograph of the experimental setup that demonstrates the wireless sensing with the first OFID communication prototype. In this experiment, the OFID tag was placed at a distance of 1 m away from the OFID reader. The energy harvesting functionality was verified by observing if the voltage V_{SC} at the tag's supercapacitor increases or not. The experiment also compared two charging cases with and without the data transmission event. **Figure 42** shows waveforms captured at the tag's supercapacitor. Initially, two charging curves had the same voltage of 3.506 V. When the OFID tag transmitted data, V_{SC} reached 3.618 V after a charging period of 10 mins as opposed to 3.634 V when the OFID tag did not transmit data. Experimental results revealed that an OFID tag could still harvest energy while transmitting information, but the harvested energy decreased. This is because the PL emission was modulated when the solar cell was biased at the maximum power point (MPP) and open-circuit (OC) conditions. During the time period when the solar cell was left in the OC condition, the tag did not harvest energy.

The same experiment also showed that the OFID tag could be used to sense the ambient temperature and transmit digitized temperature data back to the OFID reader. As shown in **Figure 41**, a heat regulator was employed to regulate the temperature under the OFID tag. A precision temperature meter (Omega Engineering HH804) was used as the temperature reading reference. During the experiment, the heat regulator initially increased the ambient temperature

up to 30 °C and stopped its operation so that the ambient temperature then dropped down slowly back to the room temperature (~ 22 °C). During the cooling down process, temperature information was recorded using readings from both the temperature meter and OFID reader. An offset of 1.8 °C was applied to the result read from the OFID reader, resulting in a maximum error of 0.39 °C with respect to the temperature meter. **Figure 43** shows recorded temperature samples from both the temperature meter and OFID reader.

4.4 The Second OFID System Prototype

The second OFID system prototype, consisting of a single-aperture OFID reader (see **Figure 14**) and an OFID tag equipped with an FPGA-based OFID module (see **Figure 30b**), has been proposed. The rest of this section presents various experiments that evaluate performances of the proposed OFID system.

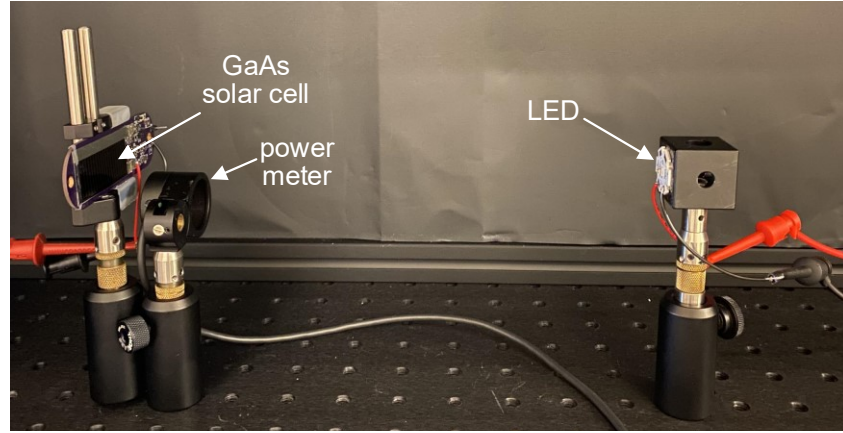
4.4.1 Single-aperture OFID Reader

The single-aperture OFID reader overcomes the optical alignment issue rooted in a dual-aperture OFID reader. As a result, the single-aperture reader eases the implementation of a line-of-sight (LOS) communication link with an OFID tag. This subsection evaluates the single-aperture OFID reader in different perspectives.

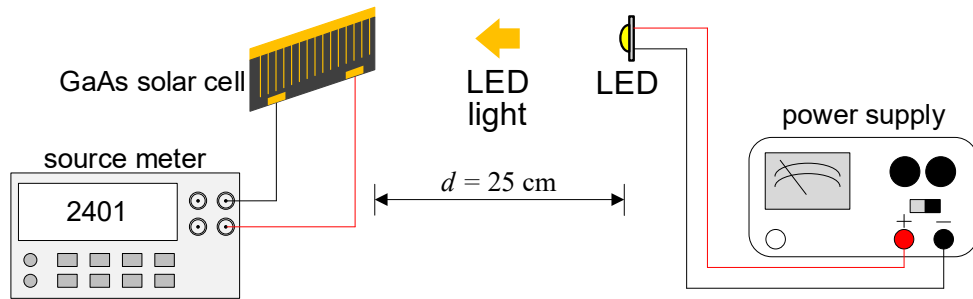
4.4.1.1 Wavelength Selection of Reader

An LED is the light source used in the reader and it transmits both power and information to an OFID tag, stimulating the solar cell to generate the PL emission. The GaAs solar cell used for this research demonstrates different harvesting efficiencies when reacting to different LED wavelengths (). Two criteria have been adopted to guide the LED wavelength selection: (1) the selected LED should maximize the cell's harvesting efficiency; and (2) the LED wavelength should locate within the human visible region in order to ease the optical alignment of a reader to a tag.

An experiment was designed to evaluate the harvesting efficiency of the GaAs solar cell when it received the same radiant power that were generated by LED light of different wavelengths/colors, such as blue, green, amber, red, and far red. **Figure 44** shows the



(a)



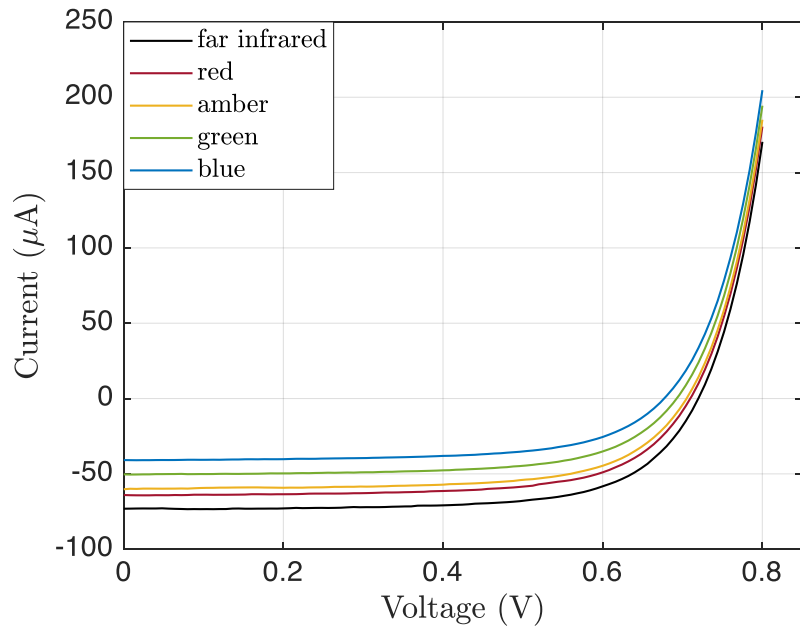
(b)

Figure 44. Experimental setup to measure harvested power when the solar cell was illuminated under different LED light. (a) photograph of the setup. (b) schematic diagram of the setup.

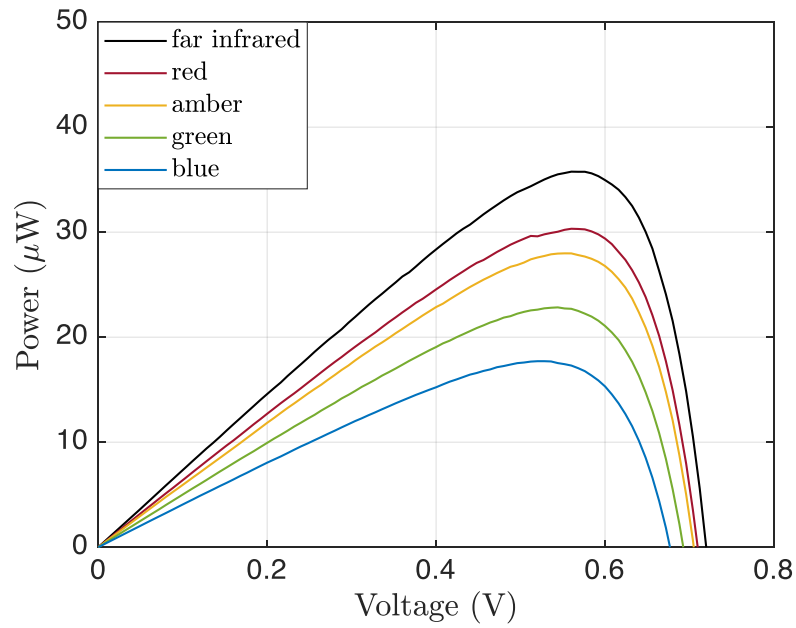
experimental setup. A precision power supply (BK PRECISION 9103) was used to supply power to the selected LED. An optical power sensor (S120C) was employed to measure the radiant power at the solar cell. In this experiment, the forward-biased voltage at each LED was adjusted so that the optical power sensor read the same radiant power of $178.5 \mu\text{W}$. A source meter (Keithley 2401) was employed to measure I-V characteristics of the solar cell. **Figure 45** shows both I-V characteristic and P-V characteristic curves. Notably, the most power was harvested when the solar cell was illuminated by far red light. With a size of $1.7 \text{ cm} \times 5 \text{ cm}$, the solar cell achieved a maximum harvesting efficiency of 20 %.

4.4.1.2 LED Driver Linearity and Power Efficiency

This section discusses the linearity and power efficiency. Accordingly, an experimental



(a)



(b)

Figure 45. Measured I-V and calculated P-V characteristic curves when the solar cell received the same radiant power generated by different LEDs.

setup, as shown in **Figure 46**, was built to evaluate these two properties.

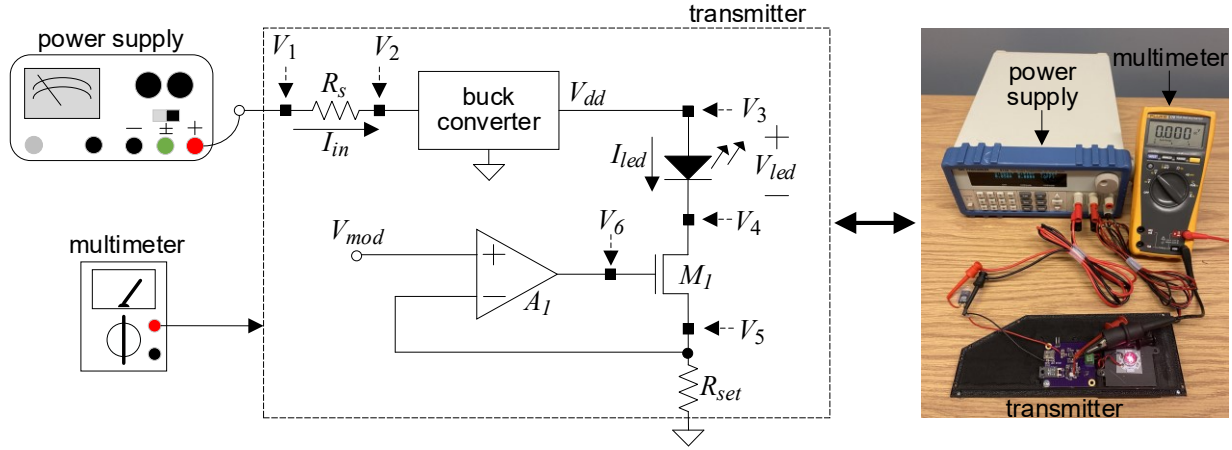


Figure 46. The conceptual and real experimental setups for evaluating both linearity and power efficiency of the LED driver.

To measure linearity, the modulation voltage V_{mod} of the LED driver was swept from 10 mV to 230 mV at an interval of 10 mV. Accordingly, voltages at six points (V_1 to V_6) were monitored. The LED's forward current I_{led} was then calculated as:

$$I_{led} = \frac{V_5}{R_{set}}$$

Equation 22. The LED's forward current I_{led} calculation.

Figure 47 shows the relationship between I_{led} and V_{mod} for different buck converter's output voltages V_{dd} . As shown in the figure, I_{led} is a linear function of V_{mod} . However, the linear range gets reduced as V_{dd} is decreased. For $V_{dd} < 2.20$ V, V_{dd} saturates and does not increase even as V_{mod} keeps increasing. In order to explain the root cause of the limited modulation range, the gate voltage V_g of the MOSFET M_1 was measured as a function of I_{led} for $V_{dd} = 2.124$ V (see **Figure 48**). This plot shows that I_{led} saturates when V_g reaches 3.3 V, i.e., the upper voltage limit at the output of the operational amplifier A_1 (Analog Devices ADA4841). Therefore, the LED driver operated in the linear modulation region as long as the output of A_1 was not saturated.

As explained in Subsection 3.2.2.2, the buck converter's output voltage V_{dd} determines the driver's power efficiency. **Figure 49** plots the power efficiency η_{tx} as a function of V_{mod} for different V_{dd} values. For each V_{dd} value, η_{tx} increases with V_{mod} , and reaches a maximum

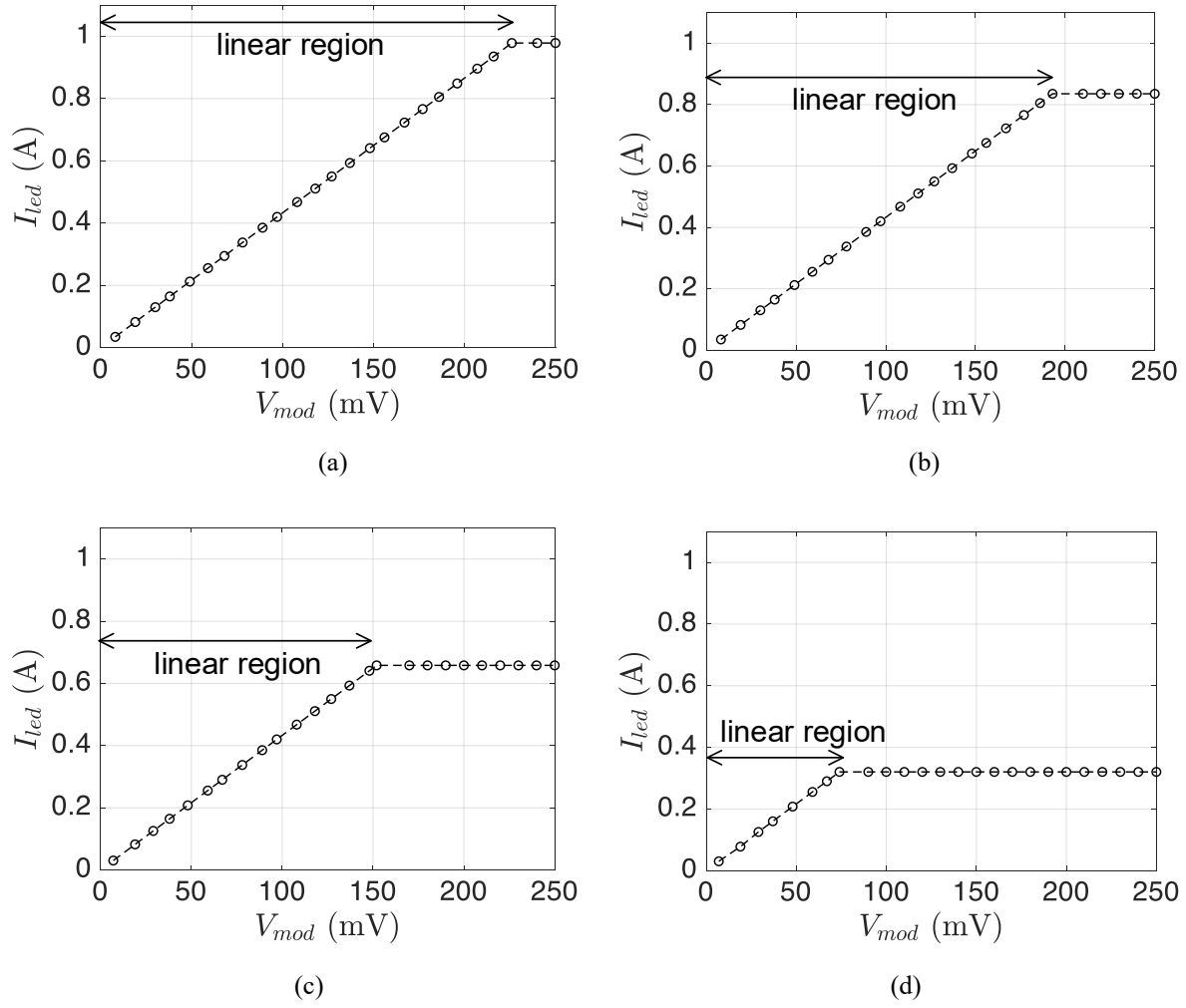


Figure 47. The relationship between the LED's forward current I_{led} and modulation voltage V_{mod} for different converter's output voltage V_{dd} . (a) $V_{dd} = 2.2$ V. (b) $V_{dd} = 2.124$ V. (c) $V_{dd} = 2.027$ V. (d) $V_{dd} = 1.819$ V.

when I_{led} saturates. **Figure 49** also reveals that a lower V_{dd} results in a higher η_{tx} at a given V_{mod} .

4.4.1.3 Reader LED Driver Circuit Bandwidth

The bandwidth of the LED driver in an OFID reader determines how fast information can be transmitted. An experiment was designed to evaluate the driver's bandwidth. The experimental setup is illustrated in **Figure 50**. A high-speed photodetector (Thorlabs PDA015A/M), featuring a bandwidth of 380 MHz, was placed at the distance of 50 cm away

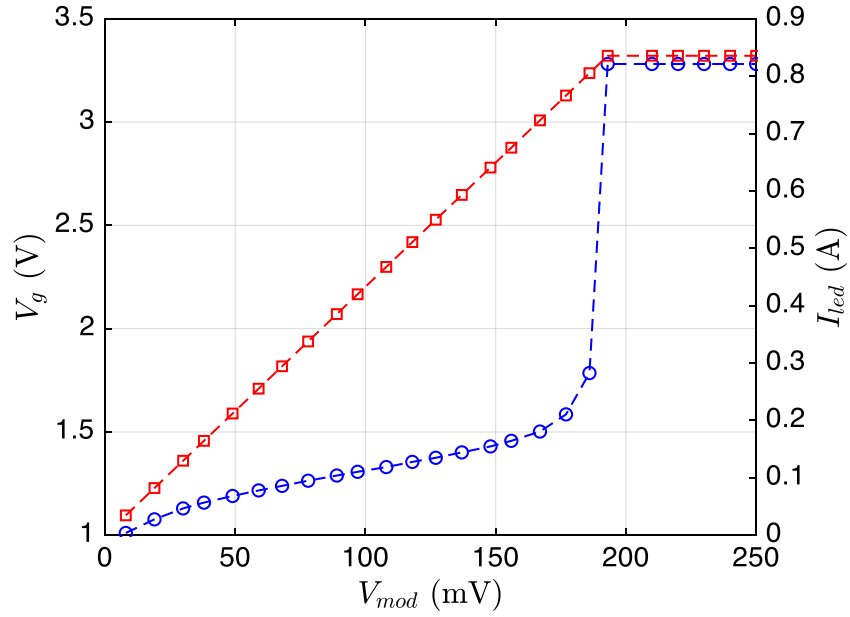


Figure 48. Relationship between gate voltage V_g and LED's forward current I_{led} for $V_{dd} = 2.124$ V.

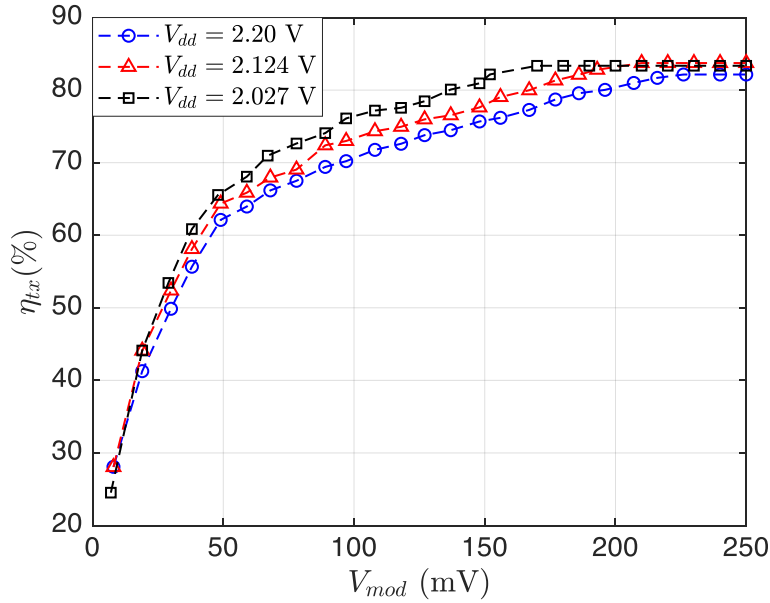
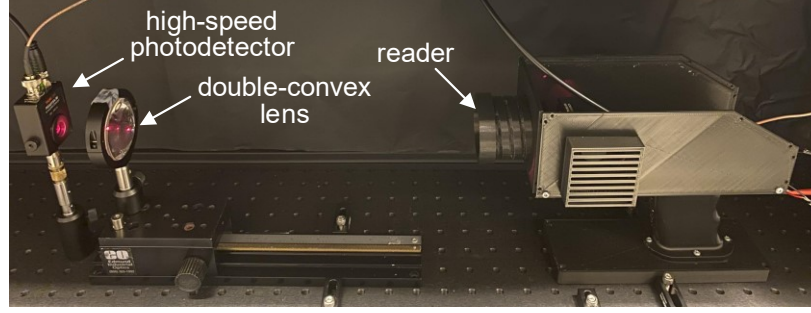
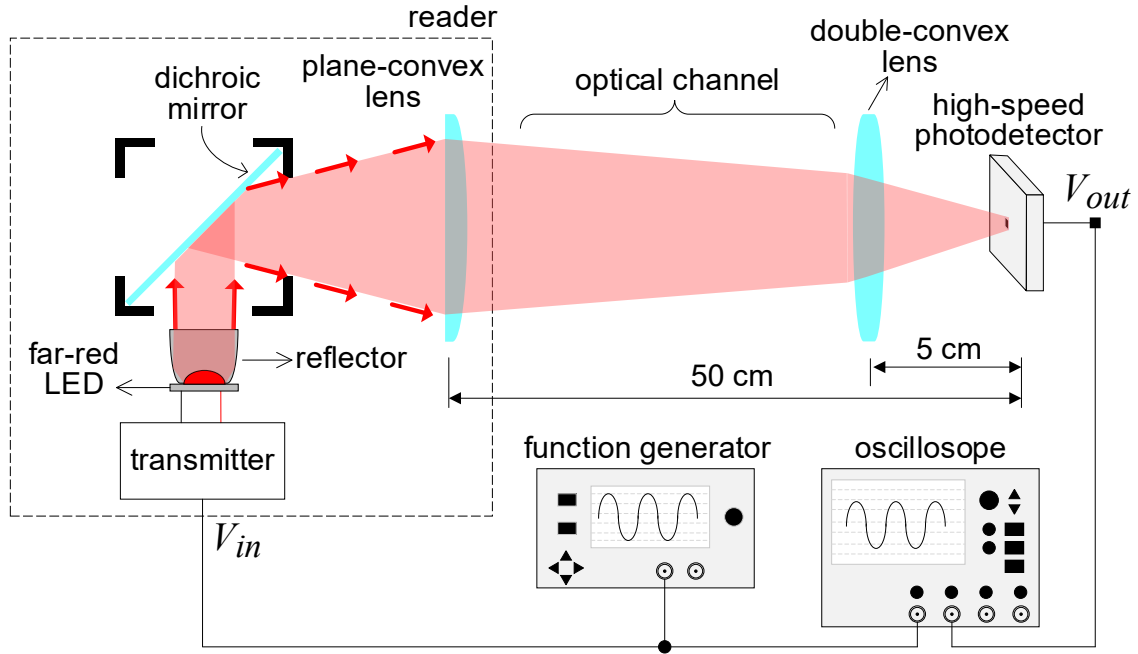


Figure 49. Relationship between the driver's power efficiency, η_{tx} , and the modulation voltage, V_{mod} , for different values of buck converter's output voltage, V_{dd} .

from the reader. A double-convex (Edmund 76284) with a focal length of 44 mm and a diameter of 54.7 mm was employed to focus light to the high-speed photodetector. A function generator



(a)



(b)

Figure 50. Experimental setup to evaluate the driver's bandwidth. (a) photograph of the setup. (b) schematic diagram of the setup.

(Rigol DG4102) fed a signal waveform V_{in} to the LED driver. To measure the frequency response, a frequency sweep from 10 Hz to 30 MHz and a constant frequency interval in the log space applied to V_{in} . An oscilloscope (SIGLENT 1104X-E) was employed to capture both transmitted and received waveforms V_{in} and V_{out} . A MATLAB script was written to compute the frequency response from the V_{in} and V_{out} waveforms. The calculated frequency response is shown in **Figure 51**. The frequency response shows that the LED driver has a bandwidth of 3 MHz.

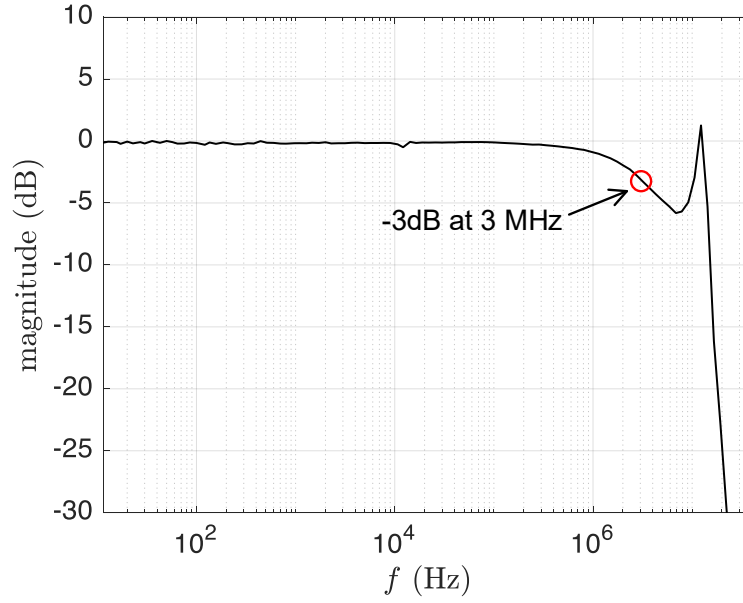


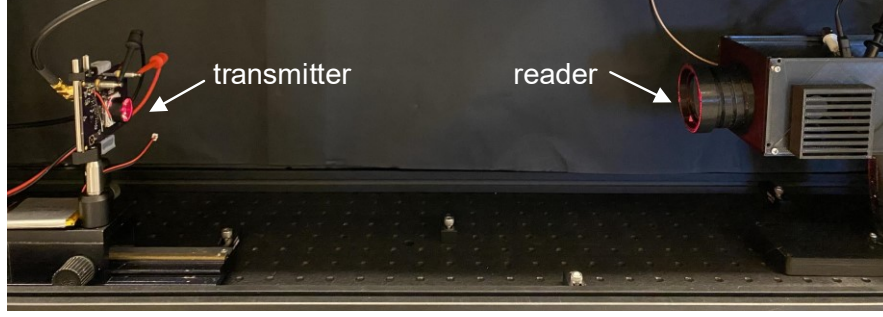
Figure 51. Normalized frequency response of the LED driver.

4.4.1.4 Reader Receiver Circuit Bandwidth

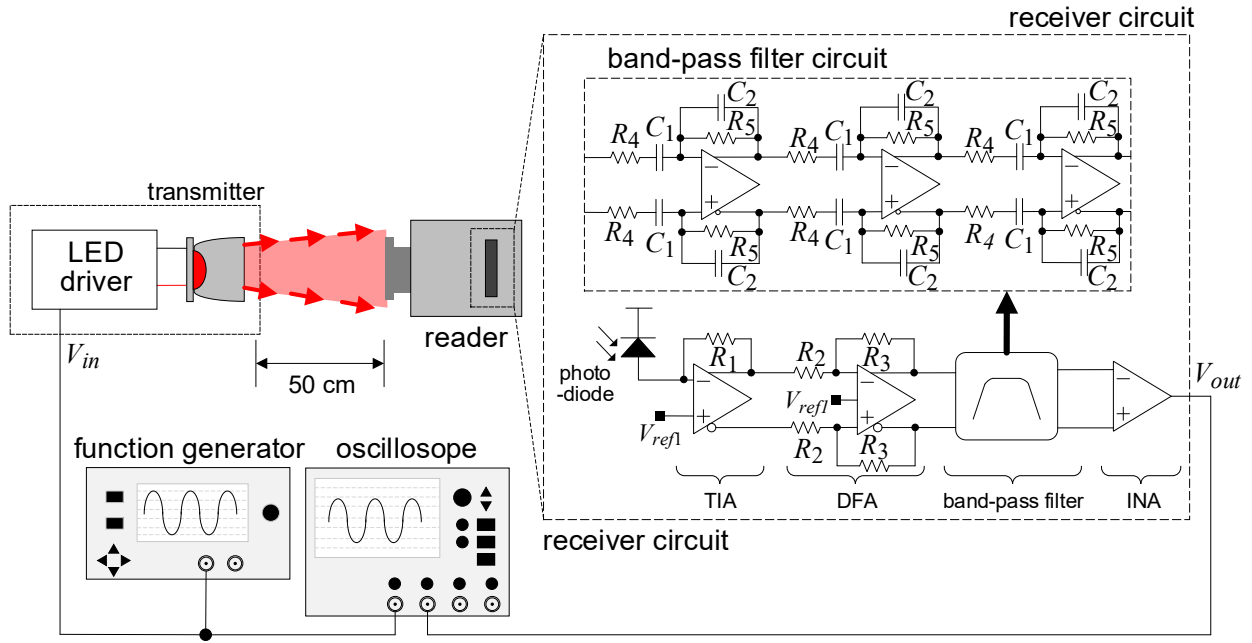
As discussed in Subsection 3.2.2.2, the receiver consists of a TIA, four DFAs, an INA, and a comparator. Three difference amplifiers were employed to build a third-order band-pass filter. The corner frequencies of the filter were selected to filter out both DC and ambient noise from fluorescent light (Fan et al., 2021), while providing a sufficient bandwidth for uplink communications.

An experimental setup was built to measure the receiver bandwidth as illustrated in **Figure 52**. An LED and an LED driver were placed at a distance of 50 cm away from the reader. The LED driver is the same as that of the reader's driver. A high-power LED (Cree XPEBFR) with an emission wavelength of 720 nm was used for this experiment.

A function generator (Rigol DG4102) fed a signal V_{in} to the LED driver. A frequency sweep from 10 Hz to 30 kHz was applied to V_{in} . The transmitted and received signal waveforms at V_{in} and V_{out} were recorded using an oscilloscope (SIGLENT 1104X-E). MATLAB was used to calculate the frequency response. **Figure 53** shows the calculated frequency response of the receiver. Values of passive components used in this receiver (see **Figure 52**) are $R_1 = 20 \text{ k}\Omega$, $R_2 = 300 \text{ k}\Omega$, $R_3 = R_4 = 15 \text{ k}\Omega$, $R_5 = 75 \text{ k}\Omega$, $C_1 = 750 \text{ nF}$, and $C_2 = 100 \text{ pF}$. The result



(a)



(b)

Figure 52. Experimental setup to measure the frequency response of the receiver in the reader.
(a) photograph of the setup. (b) schematic diagram of the setup.

shows that the receiver has lower and upper corner frequencies at 30 Hz and 10.7 kHz, respectively. Both modelled and simulated frequency responses of the band-pass filter circuit are plotted in **Figure 18** using same values of passive components. The result shows a well-matched corner frequency in both the modelled frequency response of the band-pass filter circuit and the measured frequency response of the receiver, and indicates the band-pass filter determines the bandwidth of the receiver.

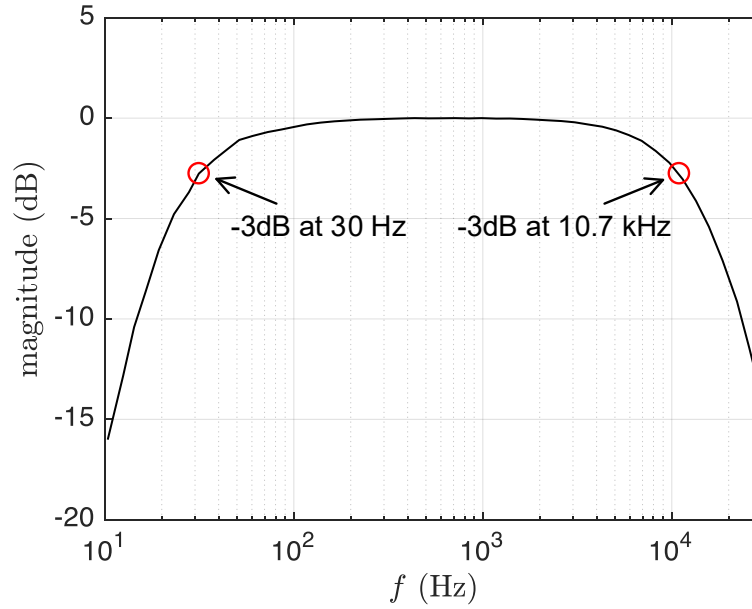


Figure 53. Normalized frequency response of the receiver. Passive components used in this receiver (see **Figure 52**) are $R_1 = 20 \text{ k}\Omega$, $R_2 = 300 \text{ k}\Omega$, $R_3 = R_4 = 15 \text{ k}\Omega$, $R_5 = 75 \text{ k}\Omega$, $C_1 = 750 \text{ nF}$, and $C_2 = 100 \text{ pF}$.

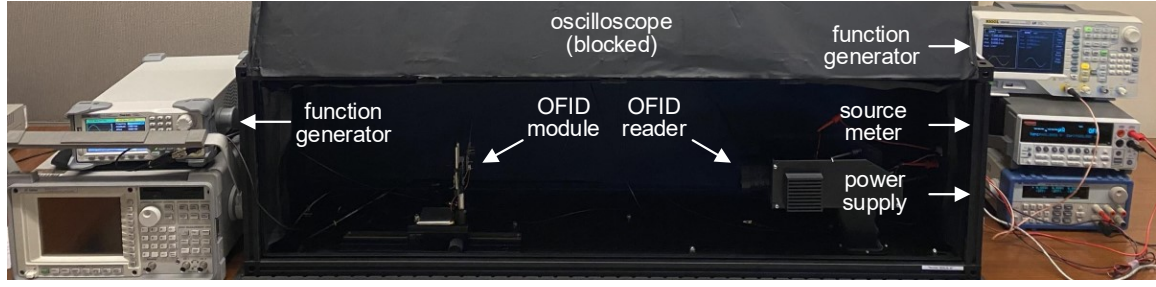
4.4.2 FPGA-based OFID Module

This subsection evaluates the proposed FPGA-based OFID module. With this module, both passive and active OFID tags can be implemented. Various experiments were designed to evaluate the module's performance. This subsection also discusses how to operate the module in order to improve both power consumption and communication performances.

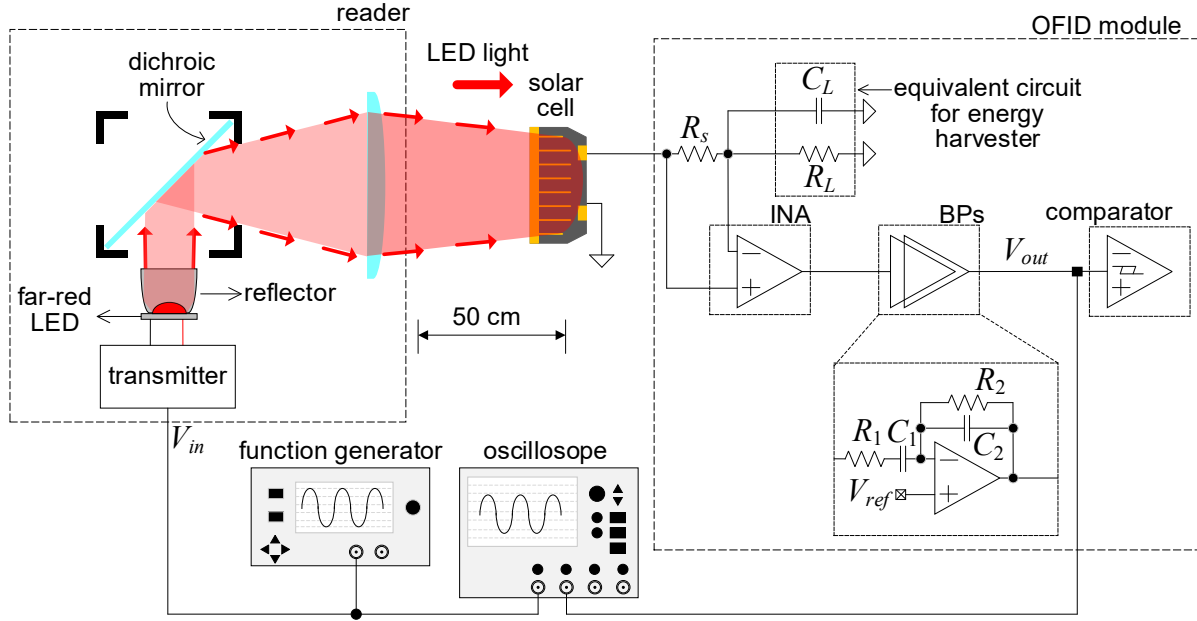
4.4.2.1 Reader Receiver Circuit Bandwidth

The tag senses received signal using a current sense resistor R_s , as explained in Subsection 3.3.3. R_s converts a current into a voltage difference, further amplified using a receiver circuit. The tag receiver circuit is made out of an INA, a second-order bandpass filter, and a comparator. The receiver's bandwidth was chosen to reduce noise, while providing a sufficient bandwidth for signal reception (Kadirvelu et al., 2021).

An experiment was designed to evaluate the OFID module's bandwidth in receiving information. **Figure 54** shows this experimental setup. An equivalent EH circuit, consisting of an RC network, was employed instead of the EH circuit. The use of equivalent EH circuit



(a)



(b)

Figure 54. Experimental setup to measure the tag's bandwidth. (a) Photograph of the setup. (b) Schematic diagram of the setup.

eliminates the switching noise from the EH circuit and allows measurement of the frequency response (Kadirvelu et al., 2021). The value of R_L was selected to bias the solar cell at MPP in order to achieve the loading effect as the EH circuit.

To measure the frequency response of the OFID module, the solar cell was illuminated by a far-red LED and an LED driver. The OFID module and the LED were placed at a distance of 50 cm. A function generator (Rigol DG4102) generated an input signal, V_{in} . The DC component of the input V_{in} was set to 150 mV. The illuminated solar cell received an irradiance of 8.2 mW/cm^2 and generated a photocurrent of 31.8 mA. Accordingly, the resistor value R_L was adjusted to bias the solar cell at MPP. The experiment was carried out for $R_L = 29 \Omega$,

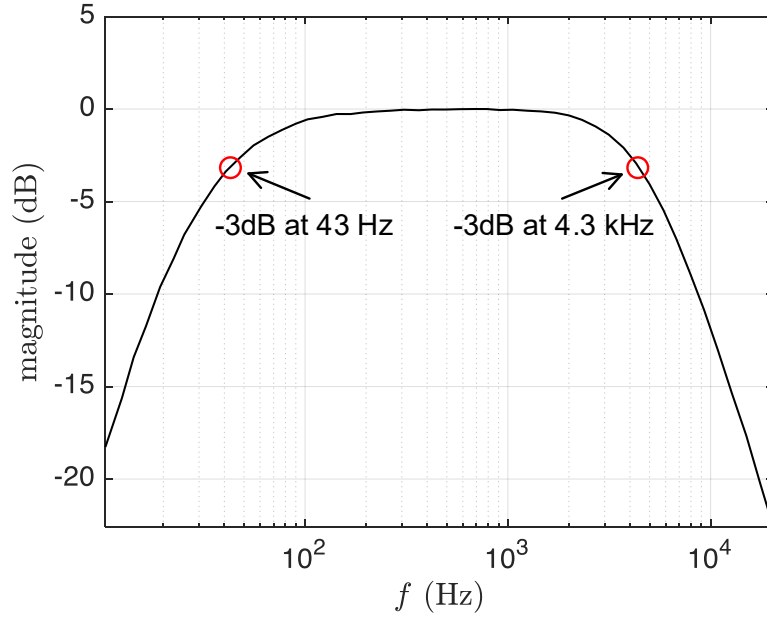


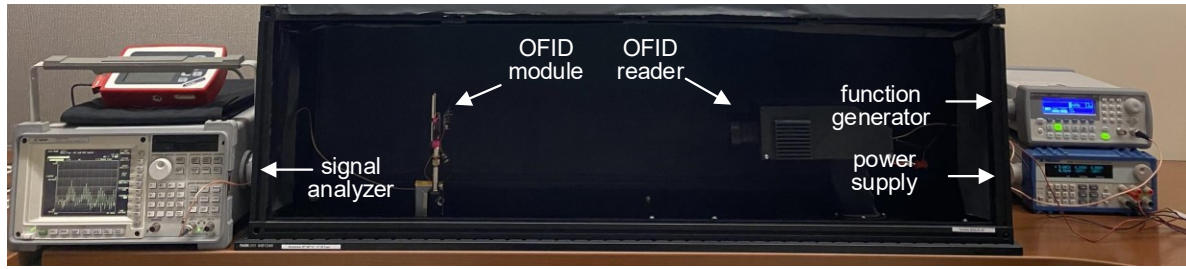
Figure 55. Normalized frequency response of the OFID module.

$R_s = 1.5 \, \Omega$, $C_L = 2.2 \, \mu\text{F}$, $R_1 = 100 \, \text{k}\Omega$, $R_2 = 200 \, \text{k}\Omega$, $C_1 = 68 \, \text{nF}$, and $C_2 = 68 \, \text{pF}$. To measure the frequency response, a frequency sweep from 10 Hz to 20 kHz with a DC level of 150 mV was applied to V_{in} . The transmitted and received waveforms at V_{in} and V_{out} were recorded using an oscilloscope (SIGLENT 1104X-E). Frequency responses were computed in MATLAB using captured waveforms. **Figure 55** shows the calculated frequency response.

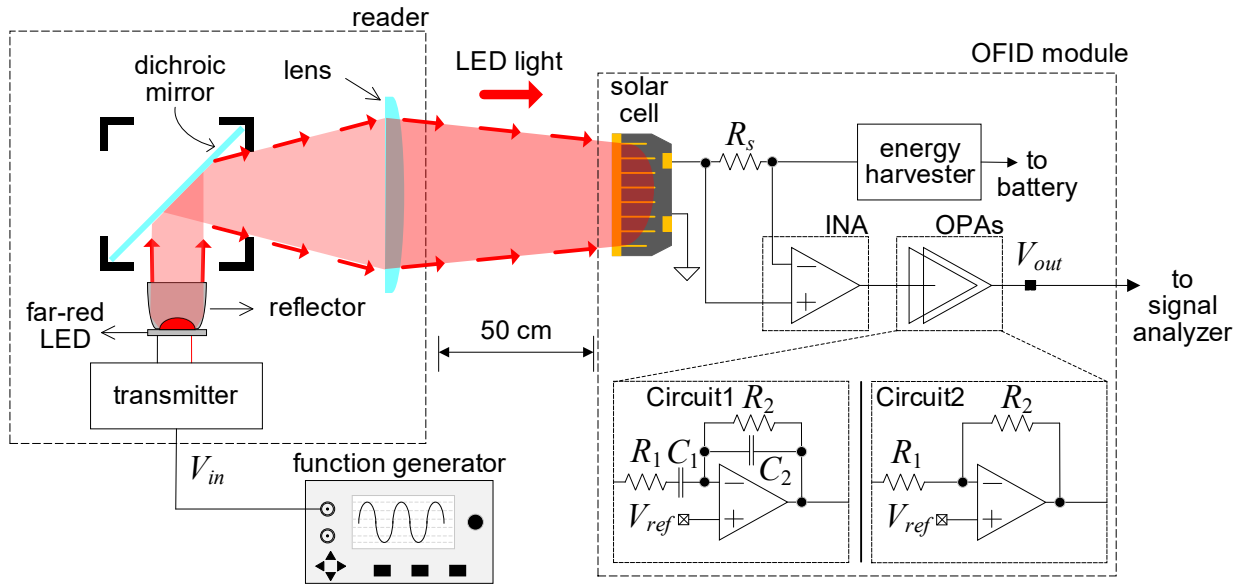
4.4.2.2 Noise Reduction Due to Band-pass Filter

As mentioned in the previous subsection, the bandwidth of the tag's receiver was selected to reduce two dominant noises in the system: DC noise and ripple noise caused by the switching activity in the energy harvester circuit (Analog Devices ADP5090). Accordingly, an experiment was designed to measure the noise reduction due to the band-pass filter in the tag's receiver.

Figure 56 shows the experimental setup that compared receiver's output noise levels before and after using the band-pass filter. Accordingly, a reference circuit (Circuit 2) was built by removing all capacitors (i.e., C_1 and 2) from a band-pass filter circuit (Circuit 1). A function generator (Rigol DG4102) was employed to provide a constant voltage at V_{in} to set the output radiant power of the LED to a constant value. The OFID module, equipped with a GaAs solar



(a)



(b)

Figure 56. Experimental setup that evaluates the noise reduction performance of the receiver. (a) photograph of the setup. (b) schematic diagram of the setup.

cell, was placed away from the reader at a distance of 50 cm. The signal analyzer Agilent 34570A was used to capture the signal waveform, V_{out} . The first experiment aimed to find out if the noise level at V_{out} changes as the solar cell receives different radiant power. Accordingly, Circuit 2 was built in the module's receiver. **Figure 57** shows measured power spectral density (PSD) of V_{out} when the solar cell received various irradiances, I_{in} . The figure shows that the ripple noise due to the switching activity of the energy harvester has a frequency of nearly 10 kHz. The noise level increases as the solar cell receives more irradiance (i.e., larger generated photocurrent). Another approach to compare noise levels is to convert PSD results to the RMS voltage.

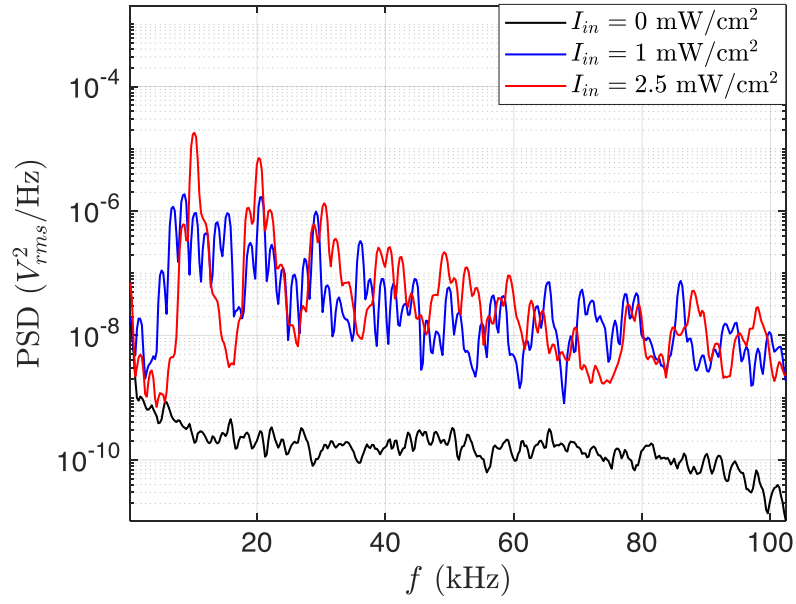


Figure 57. Measured PSD of V_{out} when the solar cell received various radiant power.

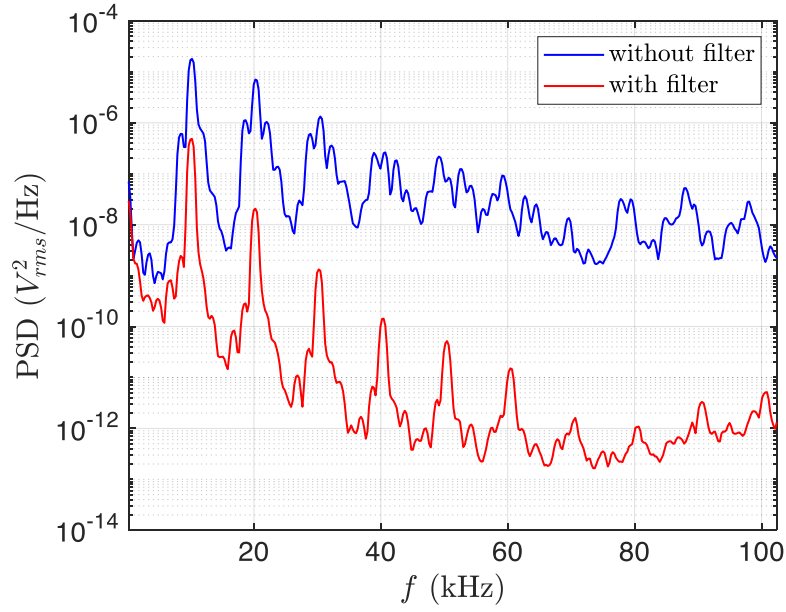


Figure 58. Measured PSD of V_{out} with and without the band-pass filter when the solar cell received an irradiance 2.5 mW/cm^2 and generated a photocurrent of 12 mA .

Experiment results show a V_{rms} of 0.107 V at $I_{in} = 1 \text{ mW/cm}^2$ and 0.187 V at $I_{in} = 2.5 \text{ mW/cm}^2$.

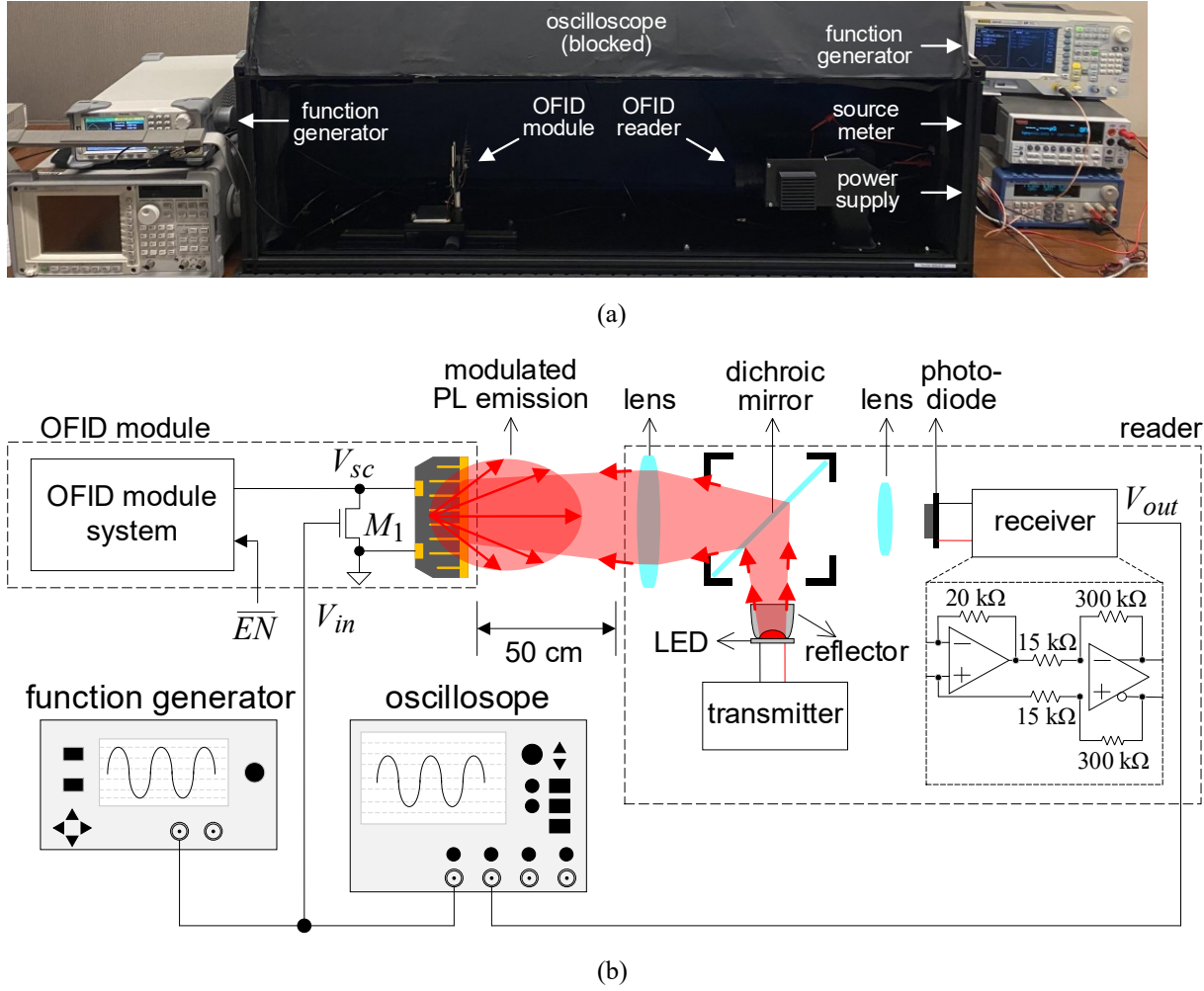


Figure 59. Experimental setup to evaluate the impulse response of the PL modulator. (a) photograph of the setup. (b) schematic diagram of the setup.

The Second experiment was carried out to compare noise levels before and after applying the band-pass filter in the receiver. During the experiment, the solar cell received the same radiant power. **Figure 58** shows measured PSD of V_{out} before and after using the band-pass filter. The solar cell received an irradiance of 2.5 mW/cm^2 and generated a photocurrent of 12 mA. Notably, the noise level due to the switching activity of the energy harvester reduces after applying the band-pass filter. As a result, V_{rms} dropped from 0.187 V to 0.02 V.

4.4.2.3 Tag PL Modulator Bandwidth

The PL modulator in the OFID module is simply N-channel MOSFET connected to the solar cell in parallel. The gate of this MOSFET is controlled directly by the FPGA so that only two

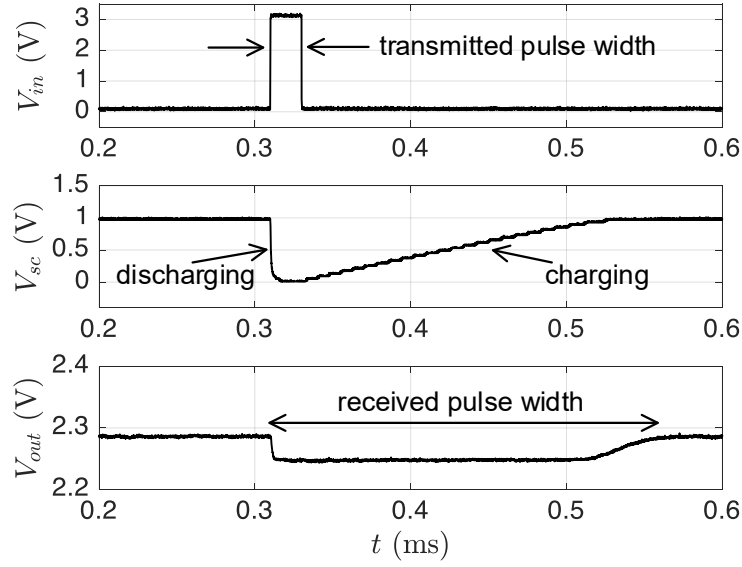


Figure 60. Captured waveforms V_{in} , V_{out} , and V_{sc} for the impulse response measurement when the solar cell received an irradiance of 3 mW/cm^2 and generated a photocurrent of 13 mA .

voltage levels (i.e., 0 V and 3 V) are available. As a result, we adopted the impulse response analysis in the time domain to evaluate how fast the PL emission can be modulated.

Figure 59 shows the experimental setup for the impulse response measurement of the PL modulator. The OFID module and reader was placed at a distance of 50 cm . The reader generated light to illuminate the solar cell and detected the PL emission from the solar cell. The receiver circuit consists of a TIA and a DFA. The total transimpedance gain of the receiver is 400 kV/A . A function generator (SIGLENT SDG2042X) applied a signal V_{in} directly to M_1 . A oscilloscope (SIGLENT 1104X-E) was employed to captured waveforms at V_{in} , V_{out} , and V_{sc} . The OFID module system was disabled during the experiment.

In the first experiment, a pulse with a width of $20 \mu\text{s}$ and a peak-to-peak voltage of 3 V was applied to V_{in} . Accordingly, responses at V_{sc} and V_{out} were captured and plotted. In the experiment, the solar cell received an irradiance of 3 mW/cm^2 and generated a photocurrent of 13 mA . **Figure 60** shows captured waveforms at V_{in} , V_{sc} , and V_{out} . As shown in the figure, the received pulse at V_{out} is wider than the transmitted pulse at V_{in} . The widened pulse is caused by both the pulse response of the cell's terminal voltage V_{sc} and the exponential relationship between the PL radiant power Φ_{lum} and V_{sc} .

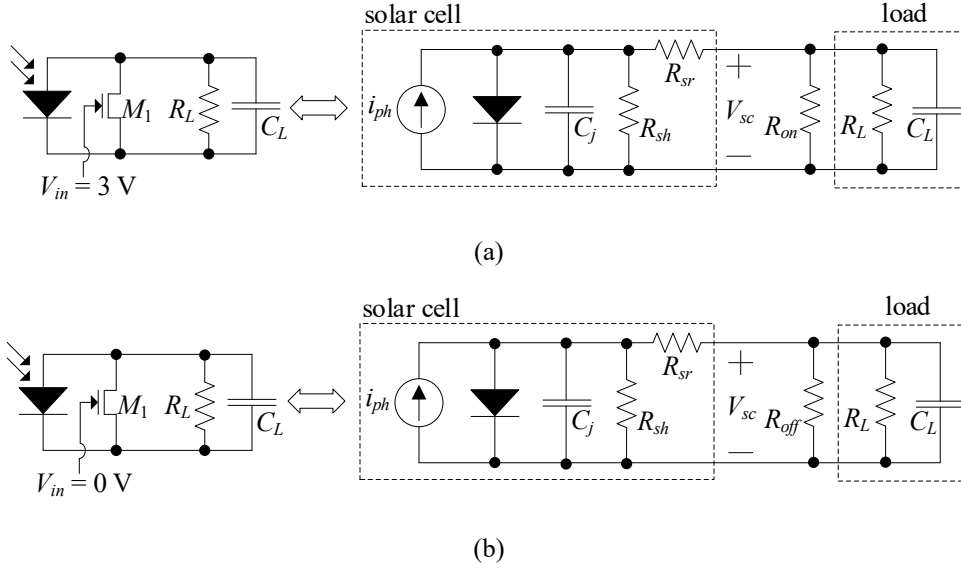


Figure 61. PL modulator and its equivalent circuit when the transistor, M_1 is open or closed. (a) M_1 is closed. (b) M_1 is open

A numerical analysis has been carried out to simulate the response of the uplink communication system to a pulse with a width $t_{pw} = 20 \mu s$ and an amplitude $A_p = 20$ V. The numerical analysis also models the pulse response of the cell's terminal voltage V_{sc} (see **Figure 60**) and the exponential relationship between V_{sc} and Φ_{lum} .

Figure 61 shows the PL modulator circuit and its equivalent circuit when the transistor, M_1 , is open or closed. M_1 is closed at $V_{in} = 3$ V and open at $V_{in} = 0$ V. The PL modulator circuit is used to model the pulse response of V_{sc} . The OFID module system can be modelled as an RC circuit, since the module system is disabled. Therefore, R_L is fairly large.

The first simulation has been carried out to simulate the pulse response of V_{sc} when a pulse is applied to M_1 . An analysis of the equivalent circuit in **Figure 61a** yields the following differential equation:

$$(C_L + C_j) \frac{dV_{sc}}{dt} = I_{ph} - I_s \left(e^{\frac{V_{sc}}{nV_T}} - 1 \right) - \frac{V_{sc}}{R_{sh}} - \frac{V_{sc}}{R_L} - \frac{V_{sc}}{R_{on}}$$

Equation 23. The equation describes the circuit in **Figure 61a**.

where, I_{ph} is the photocurrent, V_{sc} is the cell's terminal voltage, C_L is the load capacitor, C_j is the internal capacitance, I_s is the saturation current, n is the diode ideality factor, V_T is the thermal voltage, R_{sh} is the shunt resistor, R_L is the load resistor, and R_{on} is the on-resistance of M_1 . A

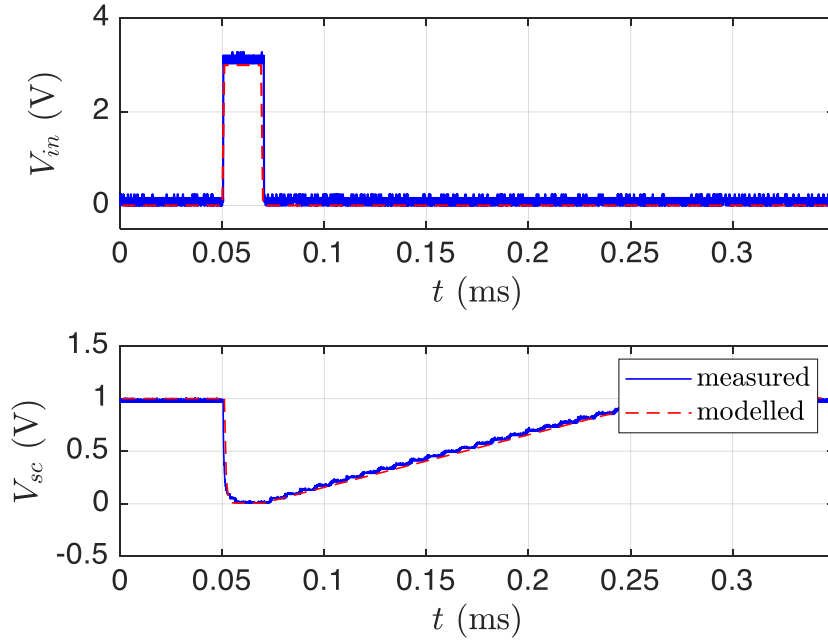


Figure 62. Measure and modelled cell's terminal voltage V_{sc} .

similar analysis can carry out for the circuit in **Figure 61b**, resulting in the following differential equation:

$$(C_L + C_j) \frac{dV_{sc}}{dt} = I_{ph} - I_s \left(e^{\frac{V_{sc}}{nV_T}} - 1 \right) - \frac{V_{sc}}{R_{sh}} - \frac{V_{sc}}{R_L} - \frac{V_{sc}}{R_{off}}$$

Equation 24. The equation describes the circuit in **Figure 61b**.

The model parameters of the solar cell were extracted using the curve-fitting technique, as explained in Subsection 3.3.3. **Equation 23** and **Equation 24** were solved numerically using the finite difference analysis in MATLAB. The initial condition was set to $V_{sc} = 1.02$ V, open-circuit voltage when M_1 is open. These two equations were solved for $I_{ph} = 13$ mA, $I_s = 0.01$ nA, $V_T = 0.026$ V, $n = 1.843$, $R_{sh} = 11.241$ k Ω , $C_L = 2.5$ μ F, $R_L = 1$ M Ω , $R_L = 0.5$ Ω , and $R_L = 1$ M Ω . In the simulation, pulse-on time t_{on} was set to 20 μ s. **Figure 62** shows the modelled and the measured V_{sc} . Notably, the modelled and the measured voltage profiles of V_{sc} agree fairly well demonstrating the validity of the derived analytical model.

To derive a model for the exponential relationship between Φ_{lum} and V_{sc} , an experiment has been carried out. **Figure 63** shows the experiment setup.

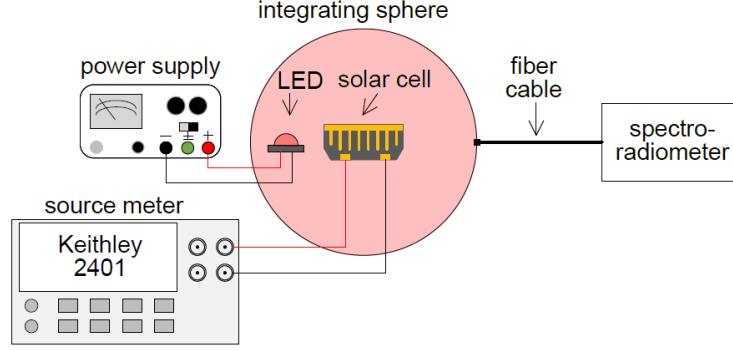


Figure 63. Experimental setup for measuring cell's photoluminescence radiant power.

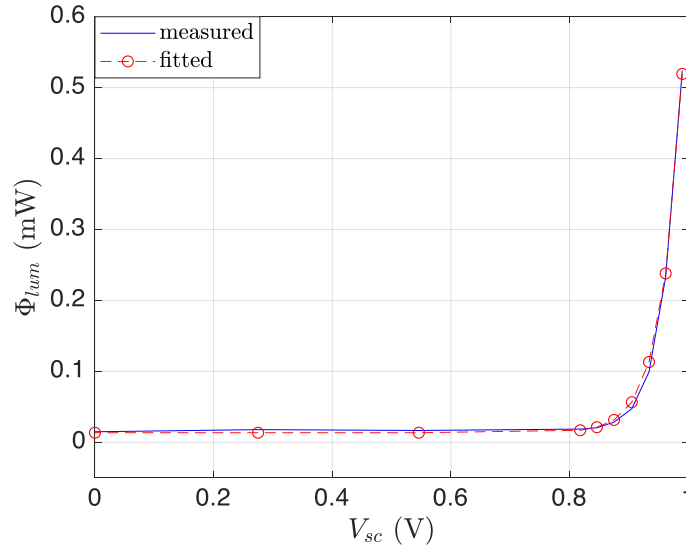


Figure 64. Measured and modelled Φ_{lum} as a function of V_{sc} .

Both the LED and the solar cell were placed inside of an integrating sphere (Stellarnet IS12). The integrating sphere provides a uniform diffusing environment for both the LED light and PL emission from the solar cell. The LED light was adjusted so that the solar cell generated a photocurrent of 13 mA. A spectroradiometer from Stellarnet was used to measure the PL emission level. The source meter was used to apply ten evenly spaced terminal voltages to the solar cell in between the cell's open-circuit and short-circuit voltages. The curve-fitting technique (Levenberg–Marquardt method) was used fit the collected PL emission samples and derive an equation expressing this exponential relationship. The derived equation is a generic version of **Equation 6** and is given by:

$$\Phi_{lum} = \Phi_0 + \Phi_s(e^{V_{sc}/nV_T} - 1)$$

Equation 25. Generic expression for the relationship between Φ_{lum} and V_{sc} . where, Φ_{lum} is the PL emission, $\Phi_0 = \eta \kappa R QE(\lambda_i) \Phi_{in}$ (the first term in **Equation 6**), and $\Phi_s = \eta \kappa \frac{E_{ph}^q}{q} I_s$. The fitted curve (see **Figure 64**) results in $\Phi_0 = 1.352 \times 10^{-5}$, $\Phi_s = 1.732 \times 10^{-6}$, and $nV_T = 0.034$.

The pulse response of the uplink communication can be determined by the following three components: (1) the pulse response of the PL modulator to the pulse at V_{in} ; (2) the exponential relationship between Φ_{lum} and V_{sc} ; and (3) the amplification gain of the optical channel and the reader's receiver. The first two components are modelled using **Equation 23**, **Equation 24**, and **Equation 25**. The relationship between Φ_{lum} and V_{out} can be simply formulated:

$$V_{out} = G_0 \times \Phi_{lum}$$

Equation 26. Relationship between V_{out} and Φ_{lum} .

where, G_0 is the amplification gain of the optical channel plus the reader's receiver. The pulse response of the uplink communication system is then modelled using parameters listed in **Table 4**. **Figure 65** shows both modelled and measured V_{out} . Notably, the modelled and the measured pulse responses of the uplink communication system agree fairly well demonstrating the validity of the derived analytical model.

If the solar cell receives more irradiances, the charging period becomes shorter and the received pulse at V_{out} has a narrower pulse width. An experiment was carried out to validate this relationship. **Figure 66** shows captured waveforms at V_{in} , V_{sc} , and V_{out} when the solar cell

Table 4. Model Parameters

Name	Value
I_{ph}	13 mA
I_s	0.01 nA
V_T	0.026 V
n	1.843
R_{sh}	11.241 k Ω
C_L	2.5 μ F
R_L	1 M Ω
R_{on}	0.5 Ω
R_{off}	1 M Ω
G_0	52.5

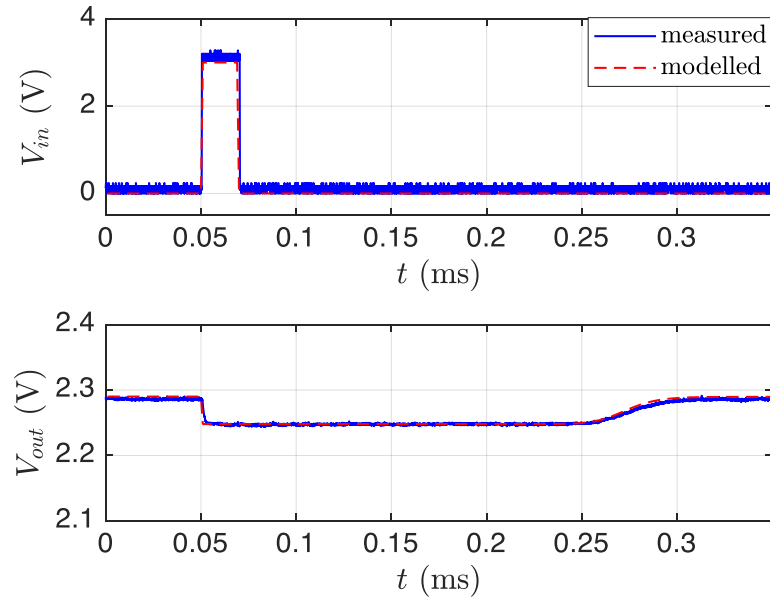


Figure 65. Measured and modelled pulse response of the uplink communication system measured at V_{out} .

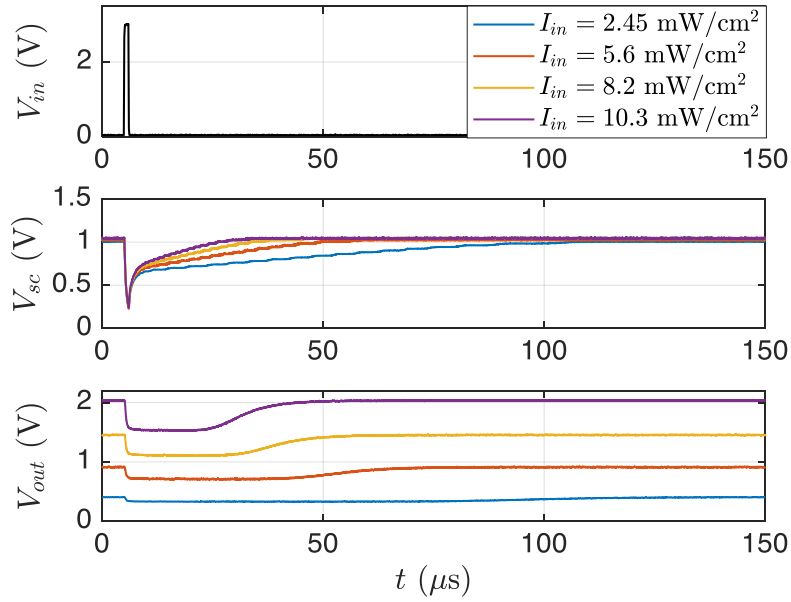


Figure 66. Captured waveforms at V_{in} , V_{sc} , and V_{out} for the pulse response measurement under different received irradiance I_{in} .

received various radiant powers. As the solar cell received more radiant power, the charging time

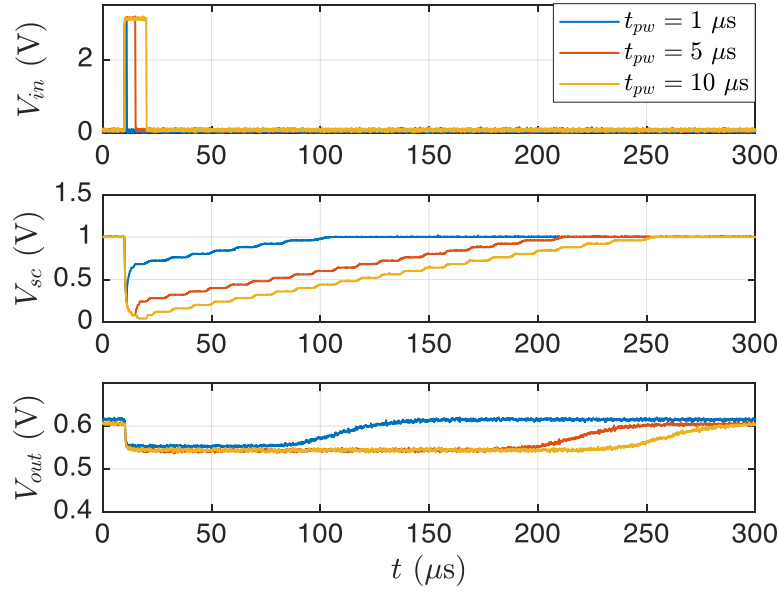


Figure 67. Captured waveforms at V_{in} , V_{sc} , and V_{out} for various pulse widths and for a received irradiance of 2.45 mW/cm^2 .

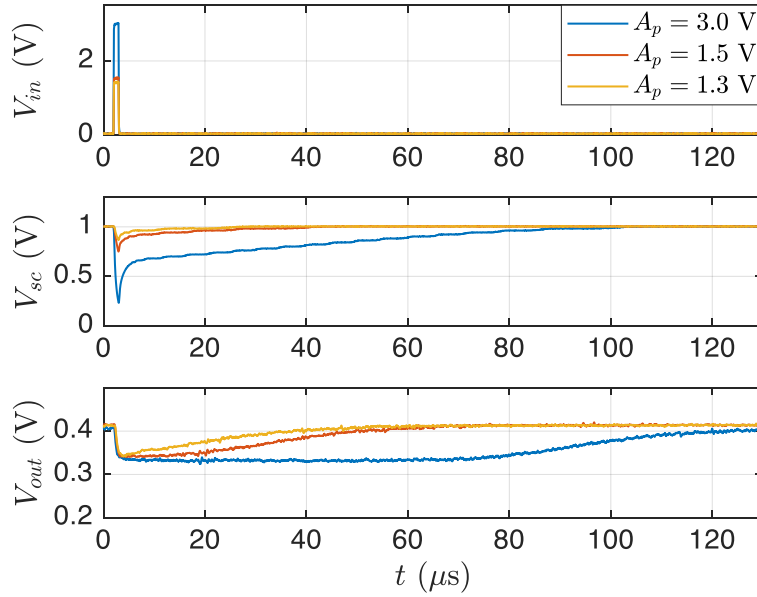


Figure 68. Captured waveforms V_{in} , V_{sc} , and V_{out} for various pulse amplitudes and for a received irradiance of 2.45 mW/cm^2 .

period at V_{sc} became shorter, and so did the pulse width at V_{out} .

Another experiment was carried out to evaluate the pulse width of the received pulses if the pulse width of pulses varies. In this experiment, the amplitude of the transmitted pulse was fixed at 3 V. The solar cell received an irradiance of 2.45 mW/cm^2 and generated a photocurrent of 11.3 mA. **Figure 67** shows captured waveforms V_{in} , V_{sc} , and V_{out} for various pulses widths. Notably, the pulse width of received pulses decreases if that of transmitted pulses reduces.

The last experiment was arranged to evaluate the pulse width of received pulses if the pulse amplitude of transmitted pulses varies. In the experiment, the solar cell received an irradiance of 2.45 mW/cm^2 and generated a photocurrent of 11.3 mA. **Figure 68** shows captured waveforms V_{in} , V_{sc} , and V_{out} for various pulse amplitudes. As shown in the figure, the pulse width of the received pulse reduces with the pulse amplitude the transmitted pulse. When the pulse amplitude of a pulse applied to the PL modulator decreases, both the on-resistance of M_1 and the voltage at the solar cell increases during the pulse-on time. Therefore, during the pulse-off time, the time period when the voltage at the cell reaches its final stable state (i.e., open-circuit voltage) decreases, resulting in a shorter received pulse at the reader. This result suggests using a lower pulse amplitude at the PL modulator if pulse modulation techniques, such as PPM and DPIM, are employed. However, a lower pulse amplitude complicates the design for an OFID module as it requires additional hardware components, such as a digital-to-analog converter (DAC).

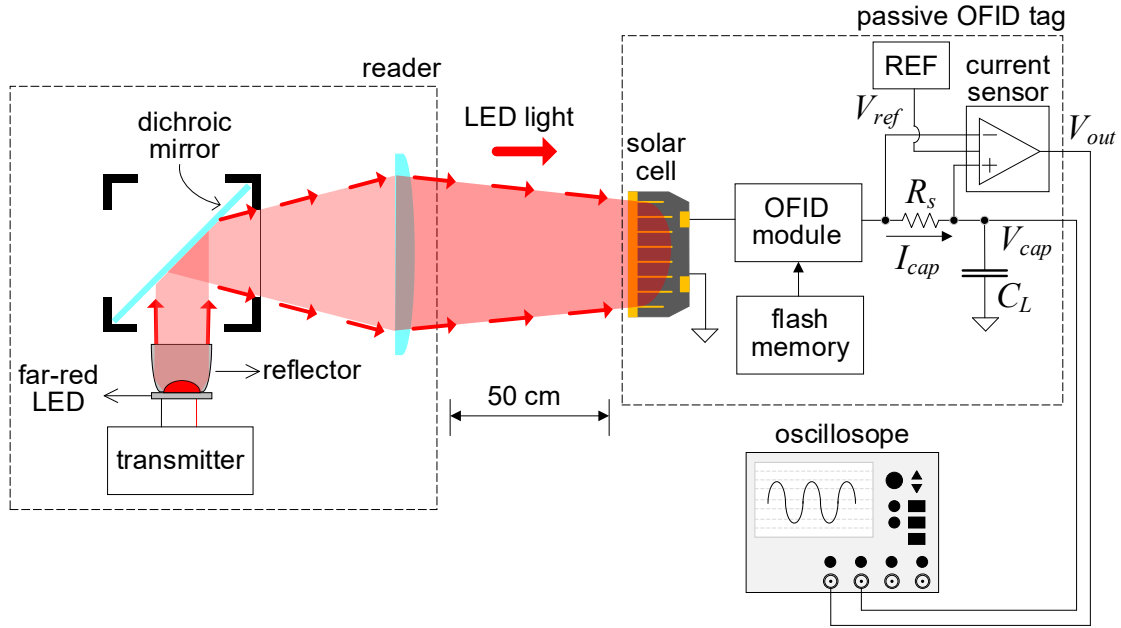
4.4.2.4 Cold Startup and Power Consumption

An OFID tag can be passive or active depending on whether it is equipped with a battery or not. To achieve the self-powering and two-way communications, a passive OFID tag should contain at least four hardware components, such as a GaAs solar cell, a flash memory, a capacitor for temporary energy storage and the needed electronic circuitry which is implemented in the OFID module described in Section 3.3.6. The flash memory (GigaDevice GD25Q32C) stores the logic configuration data for the FPGA (Lattice ICE5LP4K). The capacitor with a value of $330 \text{ }\mu\text{F}$ is employed to store energy harvested from the solar cell and supply power to the rest of hardware components.

An experimental setup was designed to capture the charging activity during a cold startup process, that is, when the capacitor is fully discharged, as shown in **Figure 69**.



(a)



(b)

Figure 69. Experimental setup to capture the charging activity of the passive OFID tag. (a) photograph of the setup. (b) schematic diagram of the setup.

In the experiment, the single-aperture OFID reader was placed 50 cm away from the OFID tag and was configured to illuminate the tag with a constant irradiance of 10.3 mW/cm^2 . The optical power density at the solar cell was measured using the optical power sensor S120C. A current sensing resistor $R_s = 1.5 \Omega$ along with an analog current sensor (Texas Instrument INA186) were used to monitor the current flow through the load capacitor C_L . This current sensing circuit has a transimpedance gain of 37.5 V/A . An external voltage reference provided a reference voltage V_{ref} to the current sensor such that it can sense current in both directions. The current I_{cap} through capacitor C_L can be calculated as follows:

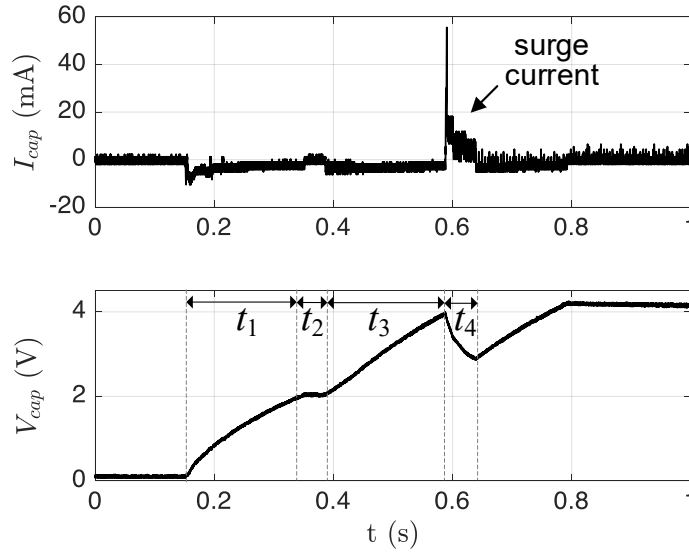


Figure 70. Captured charging profile in the cold startup when the solar cell received an irradiance of 10.3 mW/cm² and generated a photocurrent of 41.2 mA.

$$I_{cap} = \frac{V_{out} - V_{ref}}{25R_s}$$

Equation 27. Expression for I_{cap} .

where, V_{out} is the output of the current sensor. An oscilloscope (SIGLENT 1104X-E) captured the waveforms V_{out} and V_{cap} . V_{ref} was set to 2.5 V, the middle level of the supply voltage of 5 V, and $C_L = 330 \mu\text{F}$. A relatively large capacitor was needed to handle the surge current during the programming period of the FPGA.

Figure 70 shows both the charging profile and transient supply current in the cold-startup phase when the solar cell received an irradiance of 10.3 mW/cm² to produce a photocurrent of 41.2 mA. The waveform at V_{cap} captures the entire charging activity during the cold startup process. The process involves four stages (i.e., at t_1 to t_4). During t_1 , the charge pump in the EH chip charges the capacitor. Once the capacitor voltage at reaches nearly 1.95 V, the charge pump is disabled, and the DC-DC converter inside the EH chip is enabled. During t_2 the transition from the charge pump to DC-DC converter occurs. During t_3 , the capacitor voltage keeps increasing until it reaches the upper threshold voltage (i.e., 3.9 V) at which point the rest of hardware components enables. During t_4 , the FPGA in the tag reads data from the external flash

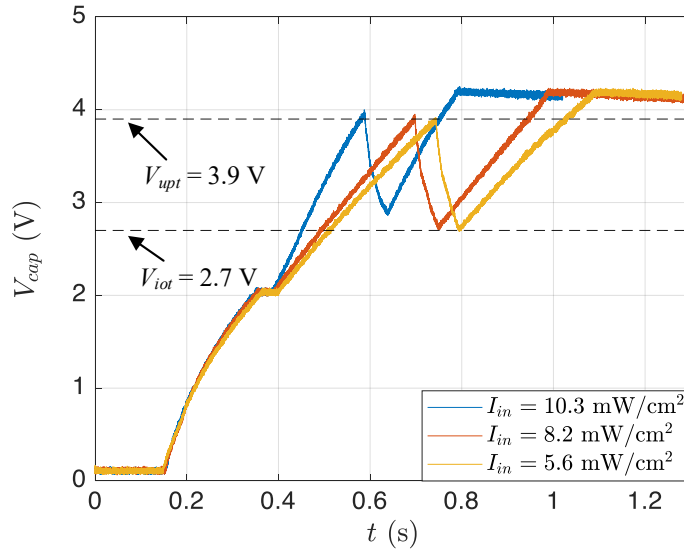


Figure 71. Captured charging profiles during the cold startup process when the solar cell was illuminated with different irradiances. The plot also marks out the upper threshold voltage V_{upt} and lower threshold voltage V_{lot} .

memory, which inducing large surge current. Accordingly, the capacitor voltage V_{cap} drops dramatically.

The passive tag was designed to provide a voltage hysteresis of 1.2 V for the capacitor voltage with an upper threshold voltage $V_{upt} = 3.9$ V and a lower threshold voltage $V_{lot} = 2.7$ V. The selected voltage hysteresis provides a sufficient headroom for the voltage drop at V_{cap} during t_4 . The lower threshold voltage is the minimum acceptable voltage of the main buck converter that supplied power to other electronic components. The value of C_L was selected to prevent a voltage drop from exceeding the predefined voltage hysteresis. In this experiment, a 330 μ F was selected such that the voltage drop at the capacitor was close to the hysteresis voltage. The cold startup process took 485 ms when the solar cell was illuminated by an irradiance of 10.3 mW/cm² and generated a photocurrent of 41.2 mA.

Another experiment was carried out to measure the time duration of the cold startup process under different lighting conditions. **Figure 71** shows captured charging profiles when the solar cell was illuminated with different irradiances. As expected, the cold startup process became faster when the solar cell received more irradiance. In the experiment, the solar cell was able to cold startup successfully when the solar cell received a minimum irradiance of

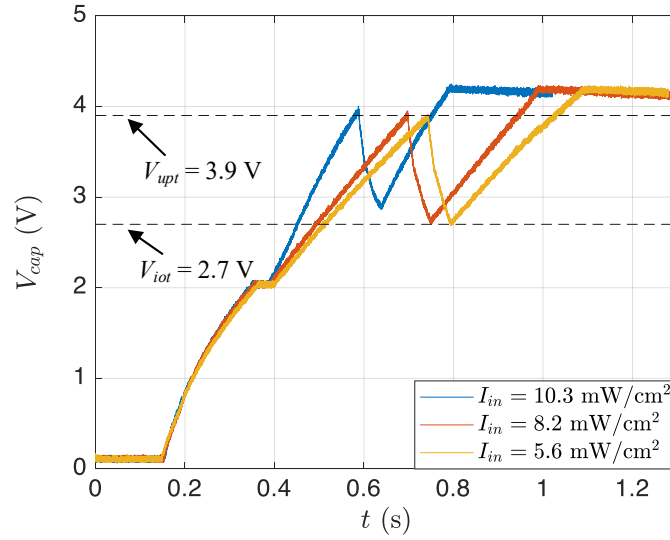


Figure 72. Captured charging profiles during the cold startup process for NVCM when the solar cell was illuminated with different irradiances. The plot also marks out the upper threshold voltage V_{upt} and lower threshold voltage V_{iot} .

5.6 mW/cm² and generated a photocurrent of 21.8 mA. This boundary condition can also be observed from **Figure 71**. The minimum received irradiance at the solar cell made sure that the voltage V_{cap} didn't drop down below the lower threshold voltage V_{iot} .

The FPGA can be programmed using an external flash memory but also its internal non-volatile configuration memory (NVCM). However, the available NVCM is only one-time programmable. An experiment was arranged to capture the charging profile when the FPGA read programs from the NVCM. **Figure 72** shows captured charging profiles when the solar cell was illuminated with different irradiances. As expected, the cold startup process is faster when the solar cell received more irradiance. A comparison of cold start charging profiles was also made between the program reading from these two memory resources. **Figure 73** shows charging profiles at V_{cap} for cold startup with these two memories when the solar cell received an irradiance of 10.3 mW/cm² and generated a photocurrent of 41.2 mA.

When the FPGA was being configured, V_{cap} dropped down to 2.872 V for the external flash memory but only to 3.3 V for the NVCM. The result indicates that less power was consumed if the FPGA is configured from the NVCM. The transient current profiles for both

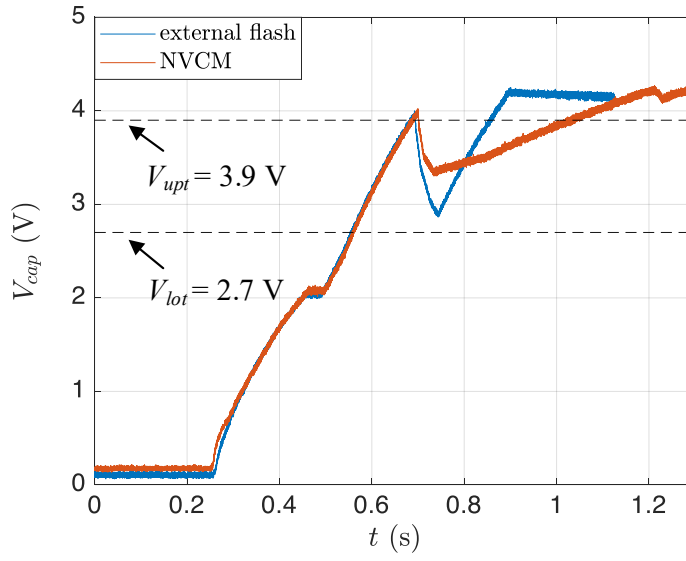


Figure 73. Captured charging profiles during the cold startup process when the FPGA was configured from an external flash memory or from an NVCM. The solar cell received an irradiance of 10.3 mW/cm^2 and generated a photocurrent of 41.2 mA . The plot also marks out the upper threshold voltage V_{upt} and lower threshold voltage V_{lot} .

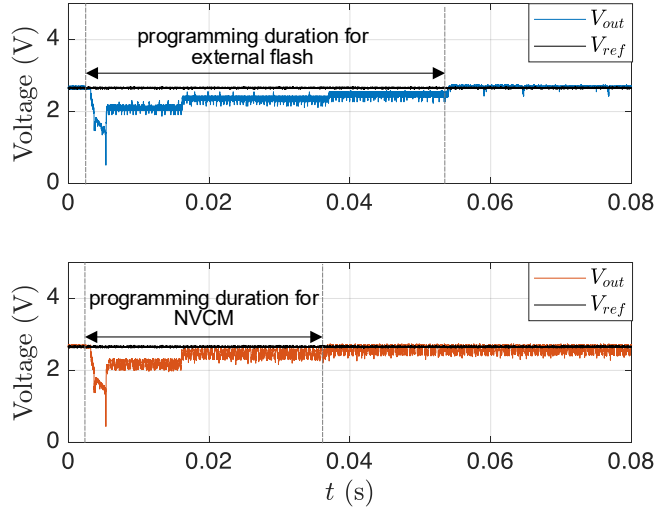


Figure 74. Signal waveforms V_{out} and V_{ref} when the FPGA read programs from either the external flash or the NVCM.

programming scenarios were extracted using **Equation 27**. **Figure 74** shows signal waveforms V_{out} and V_{ref} when the FPGA read programs from either the external flash or the NVCM.

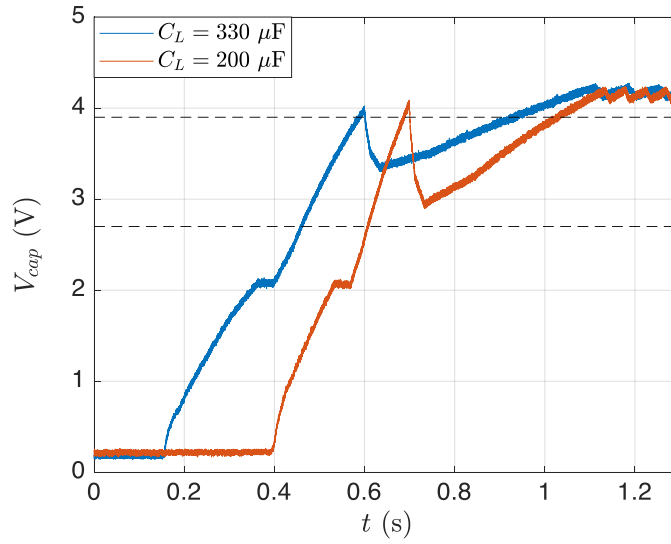


Figure 75. Captured charging profile in the cold startup process for different capacitor values when the FPGA read program from NVCM. The solar cell received an irradiance of 10.3 mW/cm² and generated a photocurrent of 41.2 mA.

Notably, the program reading from the NVCM takes less time than from the external flash. The average current drawn from the capacitor was calculated in MATLAB. The result shows that programming the FPGA with NVCM consumes an average current of 6.6 mA while this number jumps to 9.1 mA using the external flash memory. The result also indicates that a lower value of capacitor could be used to improve the cold startup process if the NVCM is used.

Another experiment was carried out to validate that a lower capacitor value (i.e., 200 μF) can be used to cold startup the passive tag configured via NVCM. In the experiment, the illuminated solar cell received an irradiance of 10.3 mW/cm² and generated a photocurrent of 41.2 mA. **Figure 75** shows charging profiles at V_{cap} . As shown in the figure, the time to cold start the tag dropped from 485 ms to 333 ms.

The power consumption of the passive tag was also evaluated. In the experiment, the capacitor was powered by a power supply that continuously supplied power to the tag. The current sensing circuit was used to monitor the tag's supply current. The tag was initially configured in the sleep mode. In this mode, no logic was implemented on the FPGA, and other electronic components, such as ADC, buck converter, and receiver, were disabled. Accordingly, the supply current was captured, and the average supply current was calculated in MATLAB. The result shows an average current of 87.4 μA. Table 4.2 lists of minimal quiescent currents for

Table 5. Minimal quiescent currents consumed by various hardware components

Component name	Part number	Quiescent current
FPGA	ICE5LP4K	71 μA
Buck converter	TPS62353	2 μA
ADC	MAX11615	0.5 μA
Energy harvester	ADP5090	0.5 μA
Flash memory	GD25Q32C	1 μA
Op amps	MAX40006	0.4 μA
Comparator	MAX40009	0.15 μA
Total		76 μA

various hardware components as extracted from datasheets. If all quiescent currents are added up together, the total power consumed by the passive tag is 76 μA that is smaller than the measured value (i.e, 87.4 μA). The difference is the power consumed by the buck converter (MAX17270), that has an efficiency less than 85 % for the load current $I_{load} < 100 \mu\text{A}$ (Maxim Integrated, 2008).

4.4.3 Uplink and Downlink Communication Performance

4.4.3.1 BER Measurement in the Downlink Direction

The bit error rate (BER) was used as the major figure of merit when characterizing the highest possible data rate in both uplink and downlink directions. BER is defined as the ratio of error bits to the total transmitted bits (Kikuchi, Okoshi, & Kitano, 1981). Therefore, two experimental setups were designed to measure BER in both uplink and downlink directions, aiming to find the highest possible data rates for both communication directions. The digital pulse interval modulation (DPIM) technique was selected for data encoding. DPIM is an asynchronous pulse time modulation (PTM) technique in which information is encoded as a sequence of discrete time slots between adjacent pulses (Ghassemlooy, Hayes, Seed, & Kaluarachchi, 1998). **Figure 76** shows a binary DPIM signal waveform applied to the reader. In binary DPIM only two symbols ('0' or '1') are transmitted. The transmission of a '0' is signaled by an inter-pulse separation of T_{s0} . The transmission of a '1' is signaled by an inter-pulse separation of T_{s1} . Here we used $T_{s1} = 2T_{s0}$.

The DPIM is beneficial to an OFID system for the following reasons: (1) band-pass filters are employed in both the OFID reader and the tag. Thus, modulation techniques with large

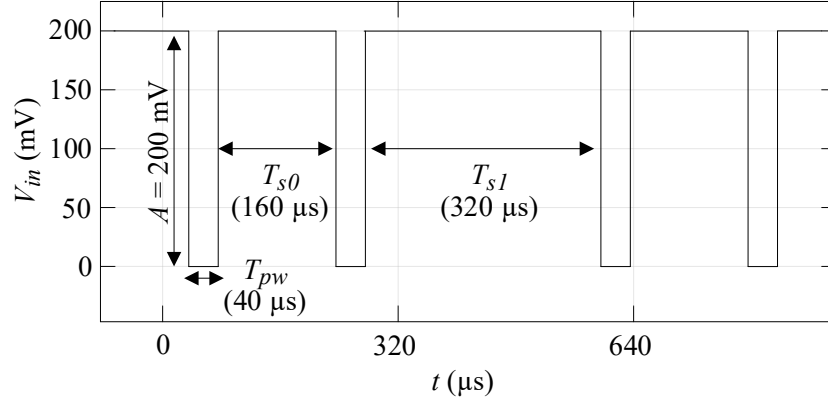


Figure 76. An example DPIM waveform applied to V_{in} .

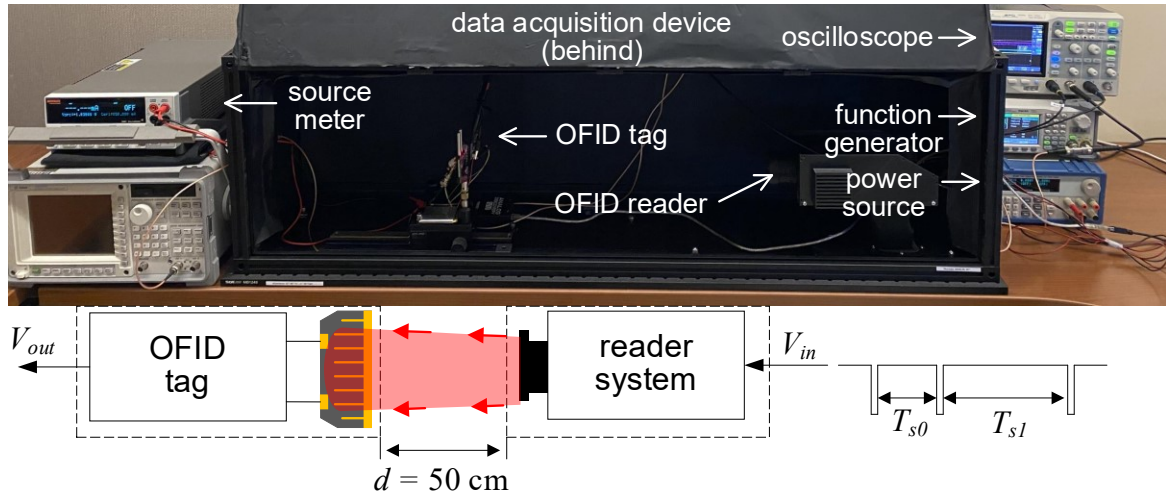


Figure 77. Experimental setup for BER measurements in the downlink direction.

DC components such as OOK are discouraged. The spectrum of a DPIM signal does not have a DC component so that it does not get distorted by the bandpass filter. (2) DPIM requires less transmission power as compared to OOK (Mahdiraji & Zahedi, 2006).

The first experimental setup, as illustrated in **Figure 77**, was built to measure BER for the downlink direction. A pseudo-random bit stream was transmitted from the OFID reader to the OFID tag. In this experiment setup, the OFID reader and tag were placed at the distance of 50 cm. A function generator was employed to generate the DPIM waveform V_{in} . A high-speed data acquisition device (MC Measurement Computing USB 1602) was employed to record the transmitted and received signal waveforms (i.e, V_{in} , V_{bp} , and V_{cmp}). These waveforms were then

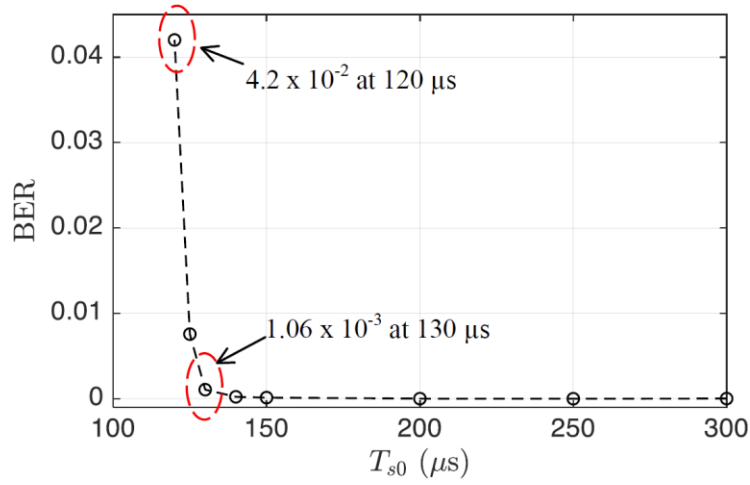
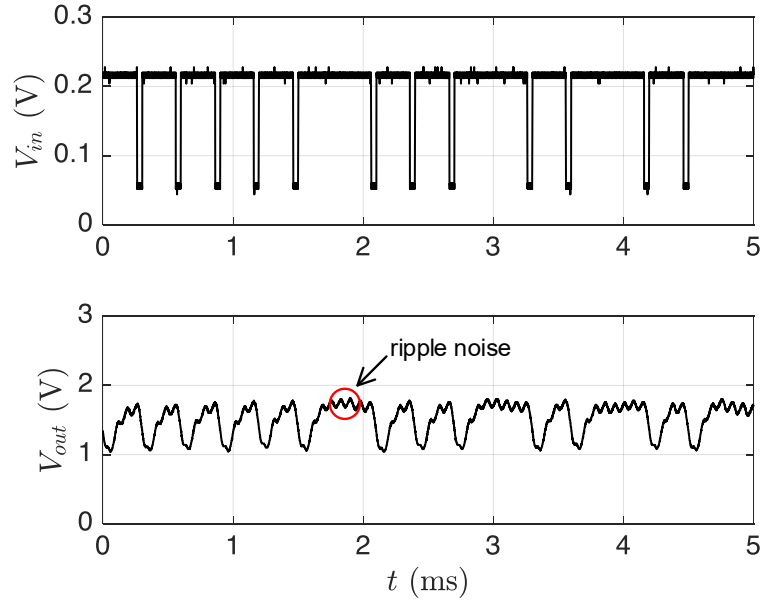


Figure 78. BER as a function of T_{s0} .

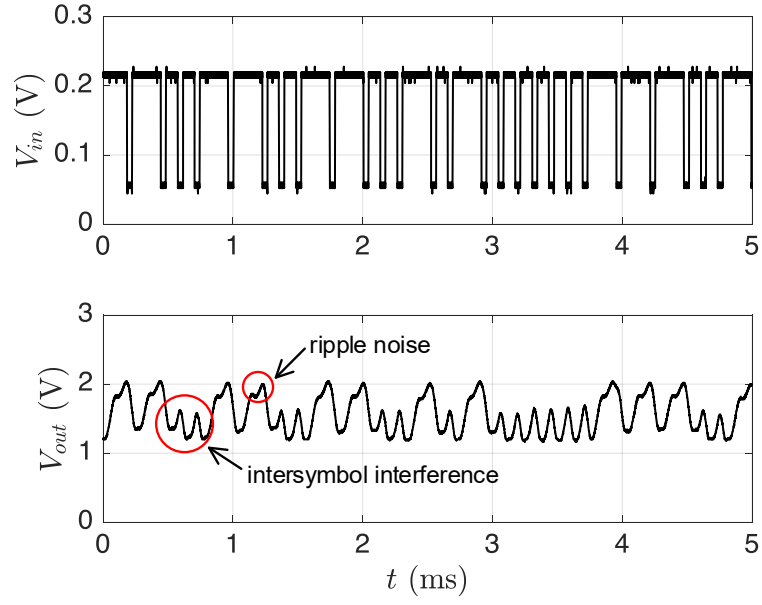
imported to MATLAB to compute the BER. An approximate number of 100,000 pseudo-random bits were generated and transmitted to compute each BER value.

The experimental setup was designed to answer two central question: (1) What is the highest data rate with an acceptable BER? (2) What are main constraints that limits the highest data rate? As the DPIM technique encodes information as a number of time slots between pulses, its length is determined only by the information content. As a result, the time period for symbol '0', T_{s0} , was employed to characterize the transmission speed (i.e., data rate).

In the first experiment, the function generator produced a sequence of pulses with a pulse width $t_{pw} = 40 \mu s$, a pulse amplitude $A = 200$ mV and varied T_{s0} from $120 \mu s$ to $300 \mu s$. This pulse width was selected so that received pulses by the tag were not distorted significantly by the tag's band-pass filter. When no pulses were transmitted, a constant voltage of 200 mV was applied to V_{in} , resulting an irradiance $I_{in} = 10.3$ mW/cm² received by the solar cell. The solar cell generated a photocurrent of $I_{ph} = 41.2$ mA. **Figure 78** shows the bit error rate as a function of T_{s0} . The result shows that the BER is nearly zero for $T_{s0} > 140 \mu s$ and it dramatically increases as T_{s0} drops below $140 \mu s$. For instance, for $T_{s0} = 120 \mu s$ (equivalent to a data rate of 7.69 kbps), $t_{pw} = 40 \mu s$, and $A = 200$ mV, a BER of 4.2×10^{-2} is achieved. If T_{s0} increases up to $130 \mu s$, this BER decreases to 1.06×10^{-3} , which is within the reach of the forward correction code. If the LDPC code is applied, the BER value further reduces to 10^{-5}



(a)



(b)

Figure 79. Transmitted and received signal waveforms at V_{in} , V_{bp} , and V_{cmp} for $t_{pw} = 40 \mu s$, and for different different T_{s0} . (a) $T_{s0} = 300 \mu s$. (b) $T_{s0} = 125 \mu s$.

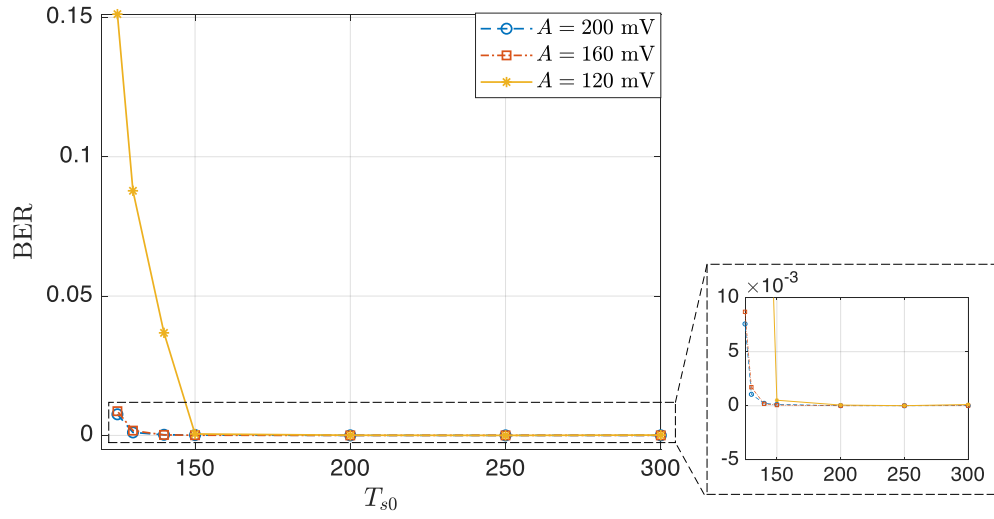
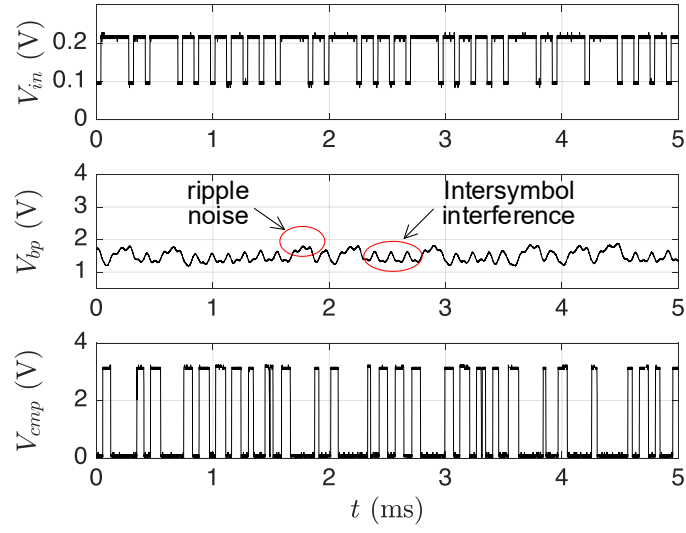


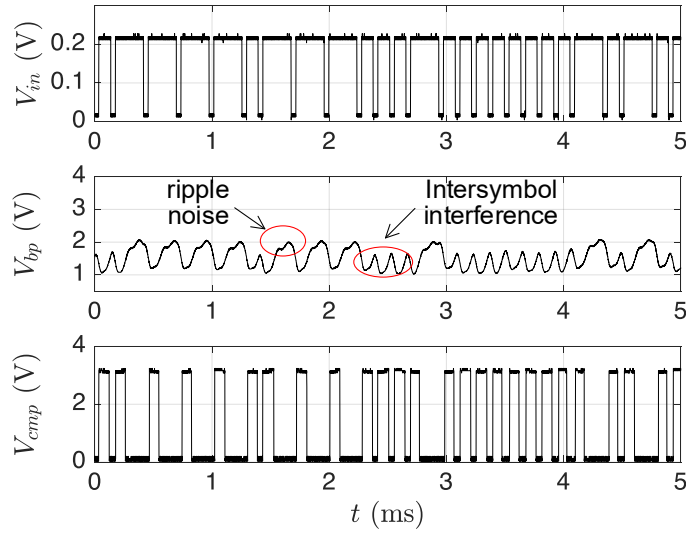
Figure 80. The bit error rate as a function of T_{s0} for $t_{pw} = 40 \mu s$, and for three pulse amplitudes of V_{in} : $A = 200$ mV, $A = 160$ mV, and $A = 120$ mV.

(International Telecommunications Union, 2004). A time-domain analysis can be carried out to inspect the cause of increased BER. **Figure 79** shows a segment of transmitted and received signal waveforms V_{in} , V_{bp} , and V_{out} for both $T_{s0} = 300 \mu s$ and $T_{s0} = 125 \mu s$. As shown in the figure, the intersymbol interference becomes significant when T_{s0} drops to $125 \mu s$. The intersymbol interference is mainly caused by the bandwidth of the module's receiver. To further reduce the intersymbol interference, pulse shaping techniques can be employed (Monmayrant, Weber, & Chatel, 2010).

Another experiment was carried out to explore how measured BER changes with various pulse amplitudes A for $I_{in} = 10.3 \text{ mW/cm}^2$, $t_{pw} = 40 \mu s$. **Figure 80** shows the BER as a function of T_{s0} for three different pulse amplitudes. The BER is zero for all three pulse amplitudes when $T_{s0} > 150 \mu s$ (see the zoom-in version of the selected region in **Figure 80**). The BER for $A_p = 100$ mV increases drastically for $T_{s0} < 150 \mu s$, which is not the case for $A = 160$ mV and $A = 200$ mV. Time-domain waveforms V_{in} , V_{bp} , and V_{out} were captured to visualize the cause of this rapid increase of BER for $A = 120$ mV. **Figure 81** shows captured waveforms for both $A = 120$ mV and $A = 200$ mV when $T_{s0} = 140 \mu s$. As observed from the waveform V_{bp} , the signal strength decreases when the pulse amplitude reduces from $A = 200$



(a)



(b)

Figure 81. Transmitted and received signal waveforms at V_{in} , V_{bp} , and V_{cmp} for $t_{pw} = 40 \mu s$, and for two pulse amplitudes. (a) $A = 120$ mV. (b) $A = 200$ mV.

mV to $A = 120$ mV. With the present of both ripple noise and intersymbol interference, the BER for $A = 120$ mV is higher than the BER for $A = 200$ mV due to reduced signal strength.

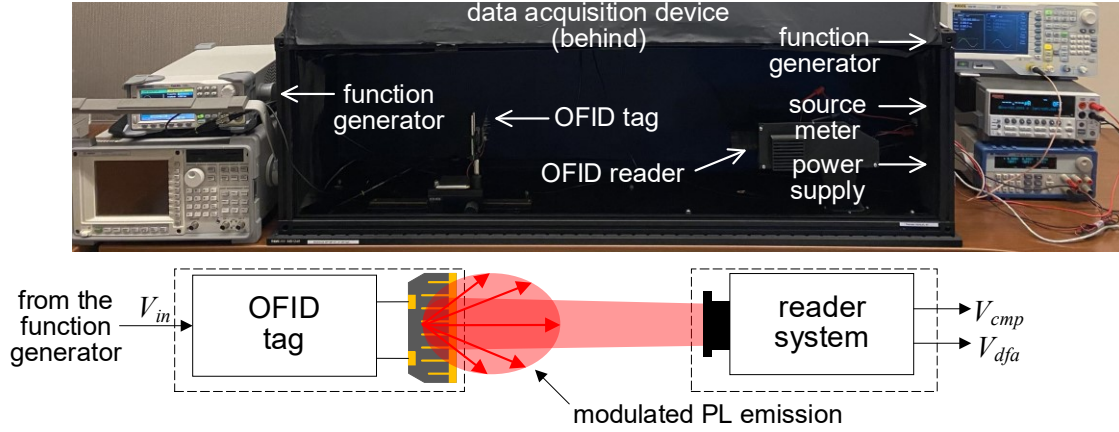


Figure 82. Experimental setup for BER measurements in the uplink communication scheme.

4.4.3.2 BER Measurement in the Downlink Direction

An experimental setup was arranged to explore the highest achievable data rate for an uplink direction. **Figure 82** shows the experimental setup. In this setup, the reader and tag were placed at a distance of 50 cm. The solar cell in the OFID tag received the radiant power generated from the reader. The function generator generated a sequence of pseudo-random bits encoded using the binary DPIM technique described in the previous subsection. **Figure 83** shows an example of DPIM signal waveform. An oscilloscope was employed to capture transmitted and received waveforms (i.e., V_{in} , V_{bp} , V_{cmp}). These waveforms were imported to MATLAB for calculating BER. The function generator simulated the behavior of the FPGA in controlling the tag's PL modulator so that the generated signal V_{in} has only two voltage levels (i.e., 0 V and 3 V). During BER measurements, DPIM pulses with a pulse width $t_{pw} = 10 \mu\text{s}$, a pulse amplitude $A = 3 \text{ V}$, and various time periods for the symbol '0' T_{s0} were generated. **Figure 84** shows measured BER versus T_{s0} . The result shows that the BER is nearly zero when $T_{s0} > 75 \mu\text{s}$ (see the zoom-in version of the selected region in **Figure 84**, and it dramatically increases as T_{s0} drops below $75 \mu\text{s}$. For example, for $T_{s0} = 72 \mu\text{s}$ (equivalent to a data rate of 13.9 kbps), $t_{pw} = 10 \mu\text{s}$, and $A = 3 \text{ V}$, a BER of 4.3×10^{-2} is achieved. If T_{s0} increases to $74 \mu\text{s}$ (equivalent to a data rate of 13.5 kbps), this BER decreases to 2.13×10^{-5} , which can be corrected down to 10^{-5} using the forward correction code (International Telecommunications

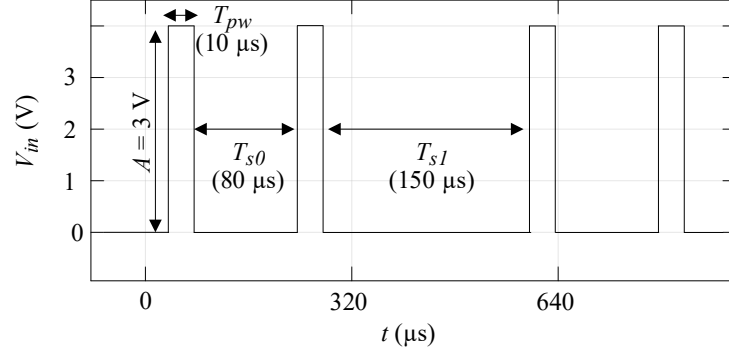


Figure 83. An example DPIM waveform applied to V_{in} .

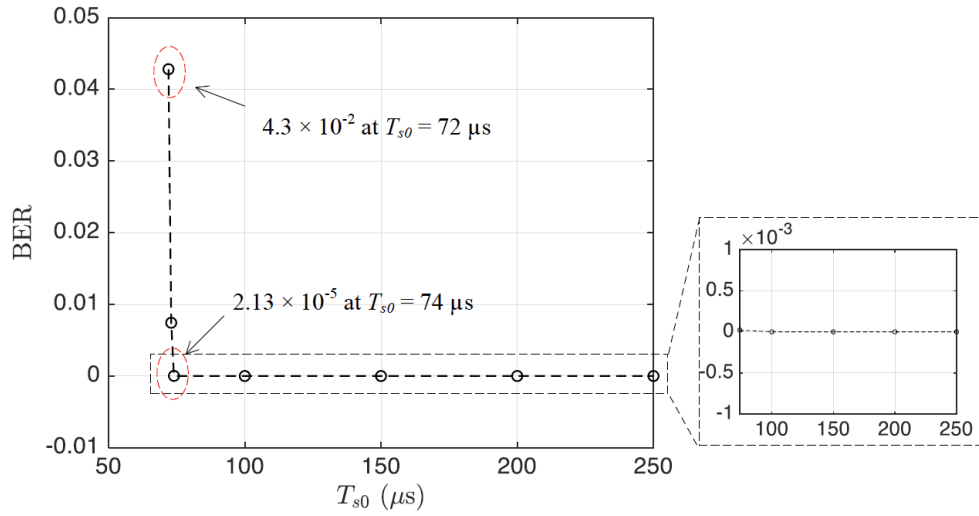
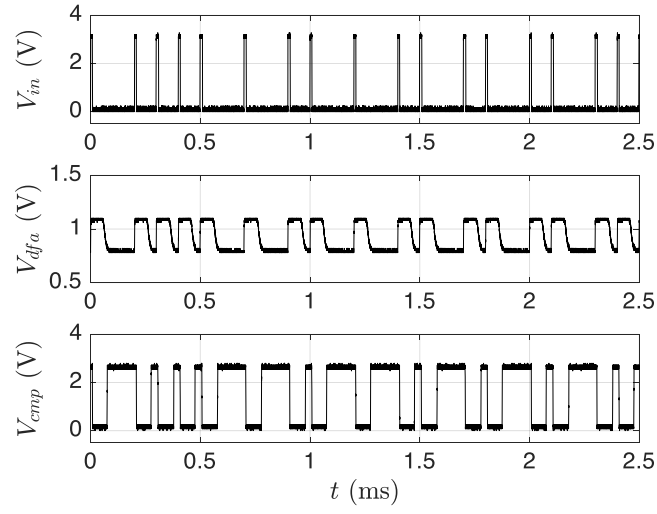


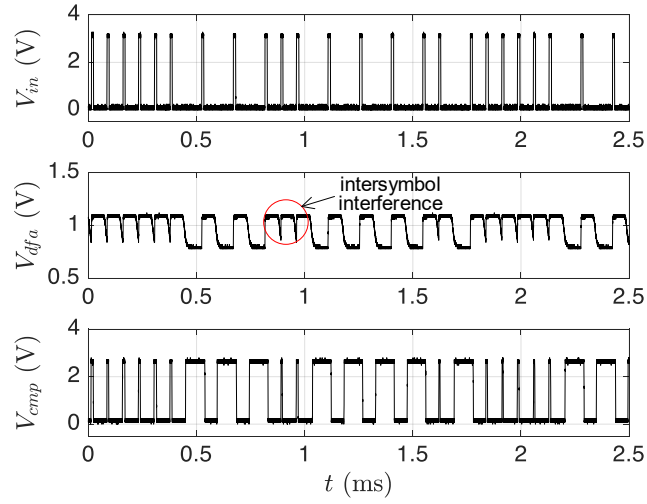
Figure 84. BER as a function of T_{s0} for $I_{in} = 10.3 \text{ mW/cm}^2$ and $t_{pw} = 10 \text{ μs}$.

Union, 2004). Data rates in an order of 100 bit/s or 1 kbit/s are sufficient for most environmental and biomedical monitoring applications, where a sampling rate of 1-100 Hz is typically required (Hempstead et al., 2008). To inspect the cause of increased BER, time-domain waveforms V_{in} , V_{dfa} , and V_{cmp} were captured for $T_{s0} = 73 \text{ μs}$. **Figure 85** shows recorded these waveforms for two T_{s0} : $T_{s0} = 100 \text{ μs}$ and $T_{s0} = 73 \text{ μs}$. Significant intersymbol interference occurs when $T_{s0} = 73 \text{ μs}$. The recorded waveform also received pulses are wider than transmitted ones, which have been explained in Section 4.4.2.3 in detail.

Another measurement was taken to explore the relationship between the BER and T_{s0} for various irradiances. **Figure 86** shows measured BER as a function of T_{s0} when the solar cell received different irradiances $I_{in} = 10.3 \text{ mW/cm}^2$, $I_{in} = 8.2 \text{ mW/cm}^2$, and $I_{in} = 5.6 \text{ mW/cm}^2$.



(a)



(b)

Figure 85. Transmitted and received signal waveforms at V_{in} , V_{dfa} , and V_{cmp} for $I_{in} = 10.3$ mW/cm^2 and $t_{pw} = 10$ μs and two different T_{s0} . (a) $T_{s0} = 100$ μs . (b) $T_{s0} = 73$ μs .

As shown in the figure, a better BER performance was achieved if the solar cell received more irradiance.

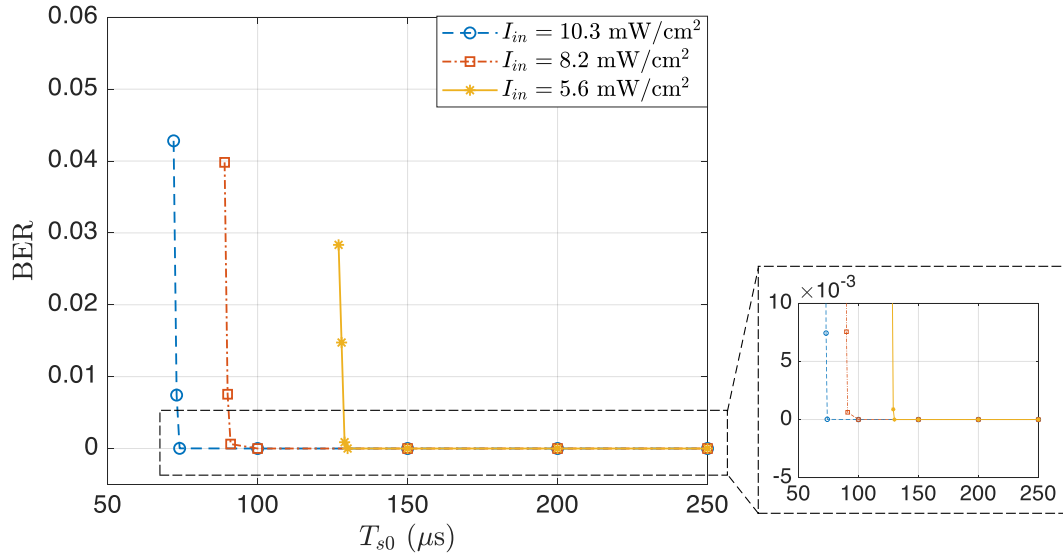


Figure 86. The bit error rate as a function of T_{s0} when the solar cell received various irradiances.

4.4.3.3 Evaluation of Communication Range

To evaluate the maximum communication range for the second OFID system prototype, 4-ary DPIM encoder and decoder were implemented in the tag and reader, respectively. The DPIM encoder encodes transmitted data into a packet. The packet was designed using the following structure: 1) three preamble pulses; 2) one data-length byte that indicates the number of data bytes; 3) several data bytes; 4) one checksum byte. The transmitted pulses have a pulse width of 40 μs . The minimal time interval between pulses was set to 640 μs to tolerant the response of the tag's PL modulator. As for a transmitted byte, it is partitioned into two halves (i.e., 4-bit nibbles). Each nibble is encoded with a quite time of $(n + 1) \times 640 \mu s$ followed by a pulse, where n is the decimal value of the nibble (i.e., an integer from 0 to 15). Therefore, each byte contains two pulses. The checksum byte is calculated by summing all transmitted bytes (i.e., data-length byte and data bytes), modulo by 256. **Figure 87** shows the state machine diagram of the implemented DPIM encoder. Three preambles pulses are generated in states $s_preamble0$ and $s_preamble1$. A byte, encoded with two pulses, is generated in states M0, M1, and M2. States s_data and $s_checksum$ prepares data bytes and checksum byte, respectively.

The DPIM decoder decodes received pulses by measuring time interval between pulse edges. The decoder firstly detects the three preambles pulses and issues an error if any preamble

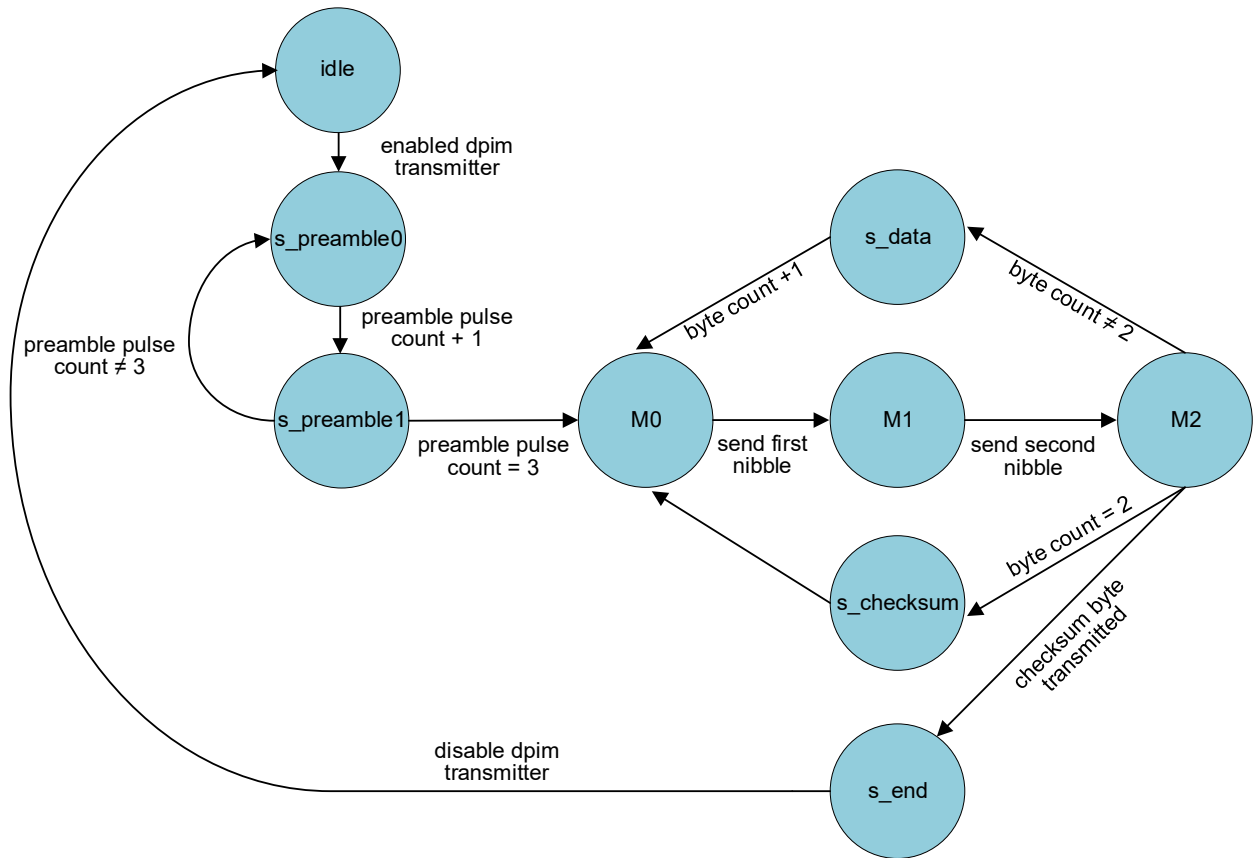


Figure 87. State machine of the 4-ary DPIM encoder.

pulse is missing. If all preamble pulses are detected, the decoder extracts data bytes and calculates the checksum. A data error is issued when the time interval between pulses are too short or too wide. A checksum error occurs when the calculated checksum byte does not match the received checksum byte. If no errors occur in a received packet, data bytes are extracted and sent to an external electronic device (e.g., a microcontroller or a laptop) via a universal asynchronous receiver-transmitter (UART) transmitter. A software UART transmitter was also implemented in the FPGA. **Figure 88** shows the state machine for the DPIM decoder.

In order to maximize the communication range, the receiver gain was maximized by setting the gain of DFA to 100, and that of the pass-band filter to 800. Therefore, the gain maximizes received pulses while making received pulses distinguishable from the noise floor at the output of INA.

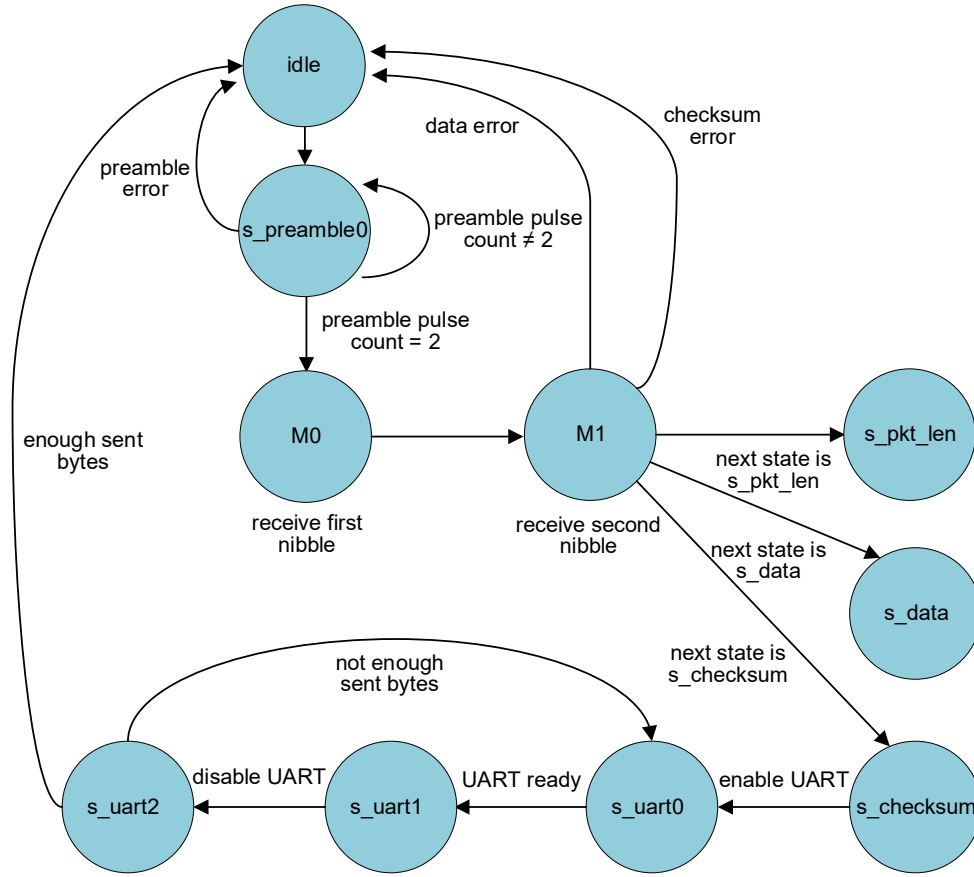
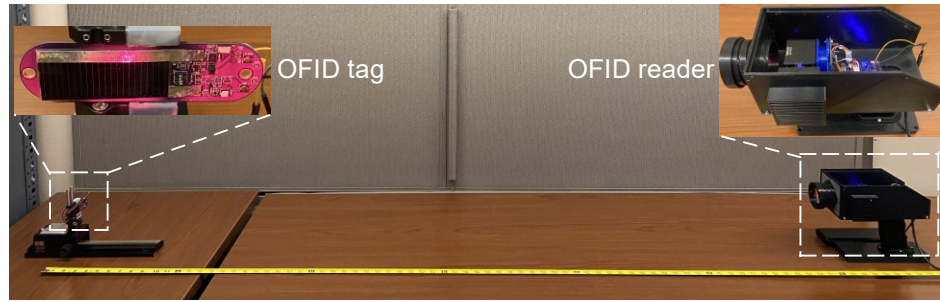
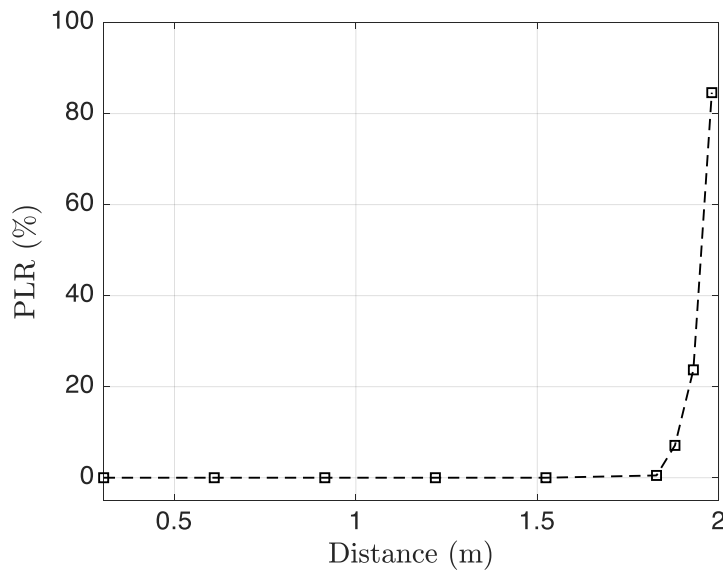


Figure 88. State machine of the 4-ary DPIM decoder.

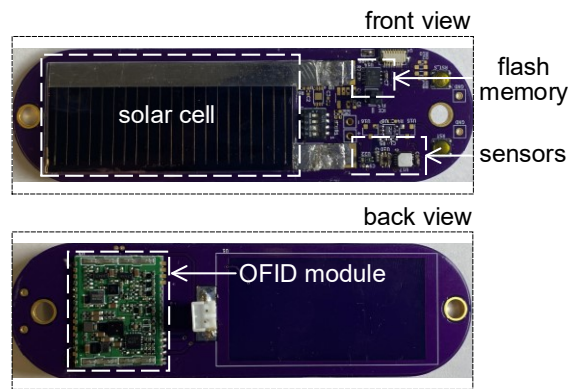
The packet loss rate (PLR), as a ratio of lost packets to total transmitted packets, was chosen to evaluate the communication range. The reader determines an error packet if it misses any preamble pulses or receives a wrong checksum byte. The tag was configured to transmit a two-byte counter, counting from 0 to 4096. Packets were transmitted at a time interval of 1 s. Accordingly, the reader decoded received pulses and sent retrieved counter to a laptop via a serial interface. A total number of 1000 packets were evaluated for each communication distance. In the experiment, the reader was configured to maximize its power output and the focusing lens (Thorlabs LA1050AB) was adjusted to focus the most light on the OFID tag. **Figure 89** shows the experimental setup, front and back views of the tag, and measured PLR at different distances between the tag and reader. No packets were dropped when the communication range was less than 1.8 m. However, PLR reached to 7.1 % at the distance of 1.88 m and increased dramatically between the range of 1.88 m to 2 m. **Figure 90** shows recorded waveforms in both tag and reader for one successful decoded packet for a



(a)



(b)



(c)

Figure 89. The experimental setup, front and back views of the tag, and measured PLR as a function of the communication distance between the tag and reader. The PLR for each communication distance was evaluated using 1000 data packets. (a) photograph of the experimental setup. (b) front and back views of the tag. (c) measured PLR as a function of the communication range.

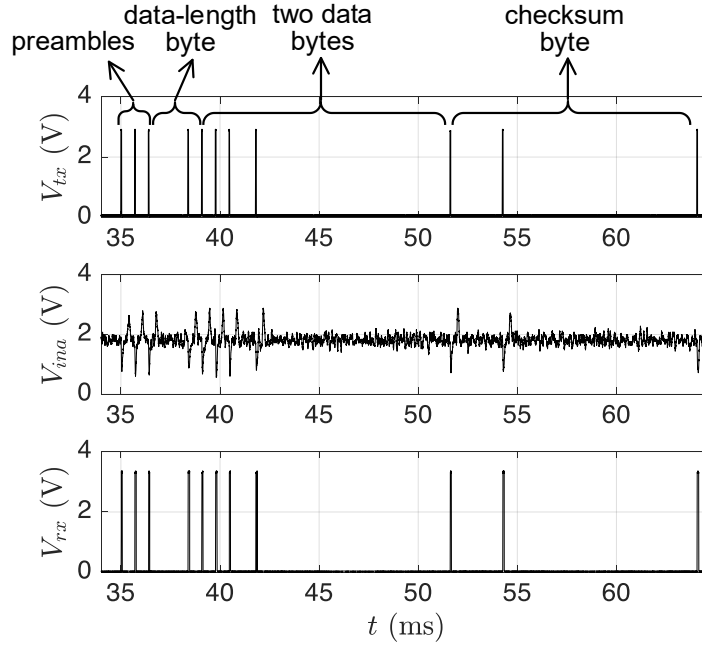


Figure 90. Typical example waveforms for one packet at a communication distance of 1.8 m. V_{tx} is the transmitted waveform at the tag's PL modulator while V_{ina} and V_{rx} are the received waveforms at the receiver's INA and comparator, respectively.

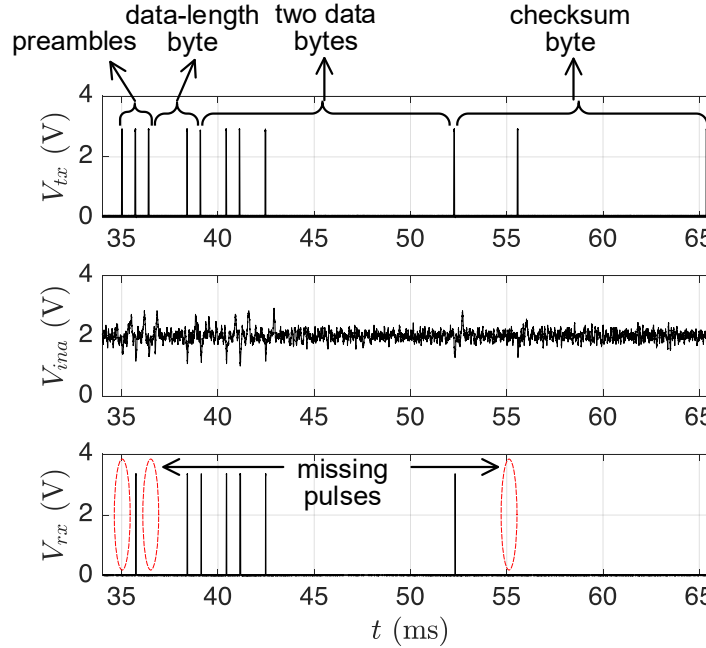


Figure 91. Typical example waveforms for one packet at a communication distance of 1.95 m. V_{tx} is the transmitted waveform at the tag's PL modulator while V_{ina} and V_{rx} are the received waveforms at the receiver's INA and comparator, respectively.

communication range of 1.8 m. As shown in the figure, the packet was successfully reconstructed at the reader as both transmitted and received waveforms (i.e., V_{tx} and V_{rx}) matched. The figure also captured the structure of a packet, consisting three preambles pulses, and additional eight pulses that represented four bytes. **Figure 91** shows recorded waveforms for one failed decoded packet for a communication range of 1.95 m. As shown in the figure, pulses are dropped in the packet, which is caused by weak signal strength.

4.5 Summary

This chapter presented various experimental designs and results to fulfill the following objectives:

1. Validate the use of luminescent emissions in a GaAs solar cell for the optical communication.
2. Compare two PL modulator circuits and discuss about the pros and cons.
3. Validate the OFID concept based on the proposed dual-aperture reader and a microcontroller-based OFID tag.
4. Characterize the proposed single-aperture OFID reader in terms of the LED selection, linearity, power efficiency, and bandwidth of both the LED driver and receiver.
5. Characterize the proposed FPGA-based OFID tag in terms of noise reduction, bandwidths of the PL modulator and receiver, cold startup time and power consumption.
6. Evaluate communication performance of both uplink and downlink channels.

A validation of luminescent emissions from a GaAs solar cell was presented at the beginning of this section. The experiment firstly shows strong luminescent emissions were captured by an infrared camera. Experiment result also shows that the luminescent power level varies with the solar cell's terminal voltage. A receiver was developed to detect the modulated PL emission at various speed, validating the use of luminescent emissions in optical communications.

Two PL modulator & EH circuits were also compared in this dissertation. A set of experiments were carried out to evaluate both circuits in harvesting energy and transmitting data simultaneously. Results showed that PL modulator & EH circuit 2 harvests more power during the data transmission than the PL modulator & EH circuit 1. However, the PL modulator & EH circuit 1 shows a better BER performance than the PL modulator & EH circuit 2.

The first OFID system prototype was developed based on a dual-aperture reader (i.e., first reader prototype) and a microcontroller-based OFID tag (i.e., first tag prototype). The system achieved a data rate of 1.2 kbps in a wireless temperature sensing application. The tag was capable of carrying out concurrent energy harvesting and information transmission. The reader prototype reads temperature data from the tag at a time interval of 5 s. The temperature reading shows a maximum error of 0.39 °C after calibration.

The second OFID system, based on a single-aperture reader (i.e., second reader prototype) and a FPGA-based OFID module (i.e., second tag prototype), was also proposed. The single-aperture reader, featured a shared optical path for both uplink and downlink communications, easing the alignment with an OFID tag. A set of experiments were carried out to characterize the proposed OFID system, and results are listed as follows:

1. Receiving the same irradiance from various visible LED lights, the GaAs solar cell harvests the most power and generates the most PL emission from the far-red LED light.
2. The LED driver in the reader has a linear modulation region that is compatible to amplitude modulation techniques, and the driver achieves a power efficiency of 84 % for a modulation voltage of 210 mV and a converter's output voltage of 2.027 V.
3. In the reader, the LED driver and receiver have bandwidths of 3 MHz and 10.7 kHz, respectively. The receiver is capable of reducing both DC and high-frequency noise from fluorescent light in an office environment.
4. The OFID module's receiver has a bandwidth of 4.3 kHz, capable of removing the DC noise and ripple noise of 10 kHz.
5. The OFID module takes 485 ms to complete the cold startup process when the solar cell receives an irradiance of 10.3 mW/cm². The time period of the cold startup process increases as the received irradiance decreases. The cold startup time can be reduced when programming the FPGA via an NVCM. The experiment result shows the cold startup time reduces from 485 ms to 333 ms for a received irradiance of 10.3 mW/cm².
6. The OFID module draws a minimum quiescent current of 87.4 μA.
7. The OFID system implements a binary DPIM encoder to evaluate BER performances in both uplink and downlink directions. In the downlink direction, the system achieves the BER of 1.06×10^{-3} and the data rate of 7.69 kbps for an irradiance of 10.3 mW/cm² and a transmitted pulse width of 40 μs. This BER value can be corrected down to 10^{-15} using

forward correction codes. In the uplink direction, the OFID achieves the BER of 2.13×10^{-5} and the data rate of 13.5 kbps for an irradiance of 10.3 mW/cm² and a transmitted pulse width of 10 μ s. The data rate can be further improved by either increasing the irradiance or decreasing the gate voltage at the PL modulator.

8. To evaluate the communication distance between a tag and reader, 4-ary DPIM encoder and decoder are implemented in the tag and reader, respectively. A two-byte counter is sent from the tag to reader at a time interval of 1 s. Accordingly, a total number of 1000 packets are used to calculate PLR for each communication distance. The experiment results show that no errors occurs when the communication distance is less than 1.8 m. However, the PLR reaches at 7.1 % when the communication distance increases to 1.88 m.

CHAPTER 5. SUMMARY, CONCLUSIONS, AND RECOMMENDATIONS

This dissertation exploited the feasibility to use solar cells as an optical antenna, capable of harvesting energy and transmitting/receiving optical information. Reusing a solar cell for these three purposes has benefits in reducing cost, size, and complexity of a system. This research also presented a new communication technique that is called optical frequency identification (OFID). Fueled by the scope of OFID, two OFID system prototypes have been designed, fabricated, and validated.

The dissertation firstly introduced previous works that used light for both bi-directional optical communication and energy harvesting. These research works shared a same vision to achieve a fully passive wireless device for low-power applications. However, these works used separate optical components for the energy harvesting and bi-directional data communication, preventing wireless devices from being further scaled down. Reusing a solar cell for both the energy harvesting and two-way communication provides an attractive solution to tackle challenges faced by previous works.

In the methodology section, the dissertation presented a detailed description on design works for proposed two OFID system prototypes.

The last section thoroughly evaluated the OFID concept and characterized proposed two OFID system prototypes. The entire section can be divided into four subsections. The first subsection firstly validated strong luminescent emissions from a GaAs solar cell. The same subsection also experimentally presented a non-linear relationship between the luminescent emission and the cell's terminal voltage.

The second subsection included a detailed comparison between two PL modulator & EH circuits. Experiments results showed both circuits were capable of transmitting data and harvesting energy at the same time. The PL modulator & EH circuit 2 harvests more power than the PL modulator & EH circuit 1. However, the PL modulator & EH circuit 1 shows a better BER performance than the PL modulator & EH circuit 2.

The third subsection evaluated the first OFID system prototype that consists of a dual-aperture reader and a microcontroller-based OFID tag. The proposed system was validated in a wireless temperature sensing application. The OFID tag was able to harvest energy and transmit data concurrently. The prototype was validated by transmitting temperature information from the

tag to the reader for a time interval of 5 s. The received temperature information shows a maximum error of 0.39 °C after calibration.

The last subsection evaluated the performance of the second OFID system prototype, including a single-aperture OFID reader and an FPGA-based OFID module. In the reader, the LED driver demonstrated a linear modulation region, and achieved a power efficiency of 84 % for a modulation voltage of 210 mV and a converter's output voltage of 2.027 V. The receiver in the reader attenuated both DC and ambient noise. Equipped with the FPGA-based OFID module, a fully passive OFID tag was achieved. The tag took 485 ms to complete the cold startup process when it received an irradiance of 10.3 mW/cm². The cold-startup period increased as the received irradiance reduced. Additionally, the cold-startup period further reduced as the tag's FPGA read programs from an NVCM. The tag consumed a minimal quiescent current of 87.4 µA.

The communication performance, such as data rate and communication range, was also evaluated for the second system prototype. BER was employed as the figure of merit for evaluating the data rate. The binary DPIM encoding technique was used to measure BER for both uplink and downlink communication directions. In the downlink direction, one hundred thousand bits were used to calculate each BER value. The result showed that the system achieved the BER of 1.06×10^{-3} and the data rate of 7.69 kbps for an irradiance of 10.3 mW/cm² and a transmitted pulse width of 40 µs. This BER value could be corrected down to 10^{-15} using forward correction codes. In the uplink direction, one hundred thousand bits were also used to calculate each BER value. The result showed that the OFID achieved the BER of 2.13×10^{-5} and the data rate of 13.5 kbps for an irradiance of 10.3 mW/cm² and a transmitted pulse width of 10 µs. The data rate could be further improved by either increasing the irradiance or decreasing the gate voltage at the PL modulator. The communication range was also evaluated for the second prototype. 4-ary encoder and decoder were implemented in the tag and reader, respectively. A total number of 1000 packets were used to calculate PLR for each communication distance. The experiment results showed that no errors occurred when the communication distance is less than 1.8 m. However, the PLR reached at 7.1 % when the communication distance increased to 1.88 m.

The contributions of this dissertation are listed as follows:

1. This dissertation validated the use of solar cells for three purposes, such as energy harvesting, data transmission and data reception.
2. This dissertation introduced a simultaneous wireless information and power reception circuit based on a modified DC-DC converter.
3. This dissertation presented two photoluminescence (PL) modulator & energy harvesting (EH) circuits for concurrent energy harvesting and information transmission.
4. This dissertation proposed two OFID system prototypes and characterizes their performance.
5. This dissertation developed various optical testbeds for characterizing proposed OFID systems.
6. This dissertation provided the theoretical analysis of the photoluminescence modulation, that was verified experimentally.
7. This dissertation experimentally determined the highest data rate and the communication range under various luminance conditions.

The research works in this dissertation can be expanded into the following directions:

1. Customize OFID systems for different application scenarios, such as harsh environmental sensing, structural health monitoring, and medical sensing. One of the attractive advantages of the proposed OFID system is that OFID tags can be localized using an imaging camera. Therefore, an OFID reader can be replaced with a camera so that it can receive information from OFID tags while pointing out the precise location of each tag.
2. Integrate OFID modules on an ASIC using available CMOS technologies in order to optimize their size, cost, and power consumption.
3. Model and optimize the reader's optical system.
4. Characterize communication performances using the solar cell's electroluminescence.

Research works during the five-year Ph.D. study has produced the following publications:

1. (Fan & Leon-Salas, 2017). This paper presented a circuit for simultaneous optical data reception and energy harvesting using a photovoltaic cell.
2. (Leon-Salas & Fan, 2018). This live demonstration used luminescent emissions of a GaAs solar cell for wireless data transmission.

3. (Leon-Salas & Fan, 2018). This paper presented the optical frequency identification (OFID) technique for Internet-of-Things (IoT) applications in which GaAs solar cell are used for energy harvesting, data transmission and data reception.
4. (Leon-Salas & Fan, 2019b). This paper firstly presented a circuit model for the solar cell including luminescent emissions, followed by introducing an approach to modulate the photoluminescence (PL). The same paper also introduced a PL modulator with a comprehensive analysis of its performance.
5. (Leon-Salas, Fan, Zhang, & Kadirvelu, 2019). This paper proposed two photoluminescence modulators and compared their performance in concurrent energy harvesting and data transmission.
6. (Fan et al., 2019) This paper analyzed the transmission speed in luminescence modulation using the impulse response technique.
7. (Fan, Leon-Salas, & Zhang, 2019) This live demonstration presented an OFID system including a laser-based reader and an FPGA-based OFID tag.
8. (Rajendran et al., 2020). This paper proposed an OFID system for the wireless temperature sensing, including a dual-aperture OFID reader and a microcontroller-based OFID tag.
9. (Fan et al., 2021). This paper proposed a low-complexity RF transceiver for torque sensing applications.
10. (Rajendran et al., 2020). This paper presented the design and development of a low-cost and low-profile sensor suitable for measuring Photosynthetic Active Radiation (PAR).
11. (Leon-Salas, Fan, Hidalgo, Peleato, & Molina, 2020). This paper proposed a new wireless solution that uses the photo-luminescence radiation of LEDs for data transmission.
12. (Fan et al., 2021). This paper presented the design and evaluations of a single-Aperture, single-Pixel reader for optical frequency identification (OFID). This paper has been accepted.
13. (Kadirvelu et al., 2021). This paper presented a circuit for simultaneous reception of optical power and data using a solar cell. A comprehensive analysis of bandwidth,

energy harvesting, electronic noise, and BER, has been carried out in a system level.
This paper is currently under review.

REFERENCES

- Ahmad, J. (2010). A fractional open circuit voltage based maximum power point tracker for photovoltaic arrays. In *2010 2nd International Conference on Software Technology and Engineering* (Vol. 1, p. V1-247-V1-250).
- Al-Halafi, A., & Shihada, B. (2018). Udo video transmission over bidirectional underwater wireless optical communication. *IEEE Photonics Journal*, 10(2), 1-14.
- Alta Devices. (2014). Technology brief: single solar cell. Retrieved 2021-02-02, from <http://dukeofdrones.com/wp-content/uploads/2015/02/singlecell.pdf>
- Analog Devices. (2009). Basic two op amp in-amp configuration. Retrieved 2021-01-23, from <https://www.analog.com/media/en/training-seminars/tutorials/MT-062.pdf>.
- Aquib, M., Jain, S., & Agarwal, V. (2020). A time-based global maximum power point tracking technique for pv system. *IEEE Transactions on Power Electronics*, 35(1), 393-402.
- Bialic, E., Maret, L., & Kt'enas, D. (2015, Sep). Specific innovative semi-transparent solar cell for indoor and outdoor LiFi applications. *Appl. Opt.*, 54(27), 8062–8069.
- Carter, B. (2013). *Op amps for everyone*. Newnes.
- Chalasani, S., & Conrad, J. M. (2008). A survey of energy harvesting sources for embedded systems. In *IEEE Southeast Con. 2008* (p. 442-447).
- Fakidis, J., Ijaz, M., Kucera, S., Claussen, H., & Haas, H. (2014). On the design of an optical wireless link for small cell backhaul communication and energy harvesting. In *2014 IEEE 25th Annual International Symposium on Personal, Indoor, and Mobile Radio Communication (PIMRC)* (p. 58-62).
- Fakidis, J., Videv, S., Helmers, H., & Haas, H. (2018). 0.5-gb/s OFDM-based laser data and power transfer using a GaAs photovoltaic cell. *IEEE Photonics Technology Letters*, 30(9), 841-844.
- Fan, X., Hidalgo, J., & Leon-Salas, W. D. (2021). A single-aperture single-pixel reader for optical frequency identification. In *2021 IEEE International Symposium on Circuits and Systems (ISACS)* (p. 1-5).
- Fan, X., Lee, S., & Leon-Salas, W. D. (2019). An optical wireless temperature sensor. In *2019 IEEE Sensors* (p. 1-4).

- Fan, X., & Leon-Salas, W. D. (2017, Aug). A circuit for simultaneous optical data reception and energy harvesting. In *2017 IEEE 60th International Midwest Symposium on Circuits and Systems (MWSCAS)* (p. 831-834).
- Fan, X., Leon-Salas, W. D., & Zhang, H. H. (2019). An embedded inductive coupling transceiver for internet of things applications. In *2019 UNSA International Symposium on Communications (UNSA ISCOMMS)* (p. 1-4).
- Ghassemlooy, Z., Hayes, A. R., Seed, N. L., & Kaluarachchi, E. D. (1998). Digital pulse interval modulation for optical communications. *IEEE Communications Magazine*, 36(12), 95-99.
- Ghosh, S., Wang, H., & Leon-Salas, W. D. (2014). A circuit for energy harvesting using on-chip solar cells. *IEEE Transactions on Power Electronics*, 29(9), 4658-4671.
- Gioux, S., Kianzad, V., Ciocan, R., Choi, H. S., Nelson, C., Thumm, J., Frangioni, J. V. (2008). A low-cost linear DC - 35 MHz high-power LED driver for continuous wave (CW) and fluorescence lifetime imaging (FLIM). In *Advanced Biomedical and Clinical Diagnostic Systems VI* (Vol. 6848, p. 19-26).
- Gorlatova, M., Kinget, P., Kymissis, I., Rubenstein, D., Wang, X., & Zussman, G. (2010, December). Energy harvesting active networked tags (ENHANTS) for ubiquitous object networking. *IEEE Wireless Communications*, 17(6), 18-25.
- Goto, Y., Takai, I., Yamazato, T., Okada, H., Fujii, T., Kawahito, S., Kamakura, K. (2016). A new automotive vlc system using optical communication image sensor. *IEEE Photonics Journal*, 8(3), 1-17.
- Haas, H., & Chen, C. (2015). What is LiFi? In *2015 European Conference on Optical Communication (ECOC)* (p. 1-3).
- Haas, H., Videv, S., Das, S., Fakidis, J., & Stewart, H. (2019). Solar cell receiver free-space optical for 5g backhaul. In *2019 Optical Fiber Communications Conference and Exhibition (OFC)* (p. 1-3).
- Hanzo, L., Haas, H., Imre, S., O'Brien, D., Rupp, M., & Gyongyosi, L. (2012). Wireless myths, realities, and futures: from 3g/4g to optical and quantum wireless. *Proceedings of the IEEE*, 100(Special Centennial Issue), 1853-1888.

- Haydaroglu, I., & Mutlu, S. (2015). Optical power delivery and data transmission in a wireless and batteryless microsystem using a single light emitting diode. *Journal of Microelectromechanical Systems*, 24(1), 155-165.
- Hempstead, M., Lyons, M., Brooks, D., & Wei, G. (2008, 04). Survey of hardware systems for wireless sensor networks. *J. Low Power Electronics*, 4, 11-20.
- International Telecommunications Union. (2004). Forward error correction for high bit-rate dwdm submarine systems, document itu-t g.975.1, itu. Retrieved 2021-04-20, from <https://www.itu.int/rec/T-REC-G.975.1-200402-I/en>
- Jokanovic, D., & Josipovic, M. (2011). Rf spectrum congestion: Resolving an interference case. In *2011 IEEE International Conference on Microwaves, Communications, Antennas and Electronic Systems (COMCAS 2011)* (p. 1-4).
- Kadirvelu, S., Leon-Salas, W. D., Fan, X., Kim, J., Peleato, B., Mohammadi, S., & Vijayalakshmi, B. (2021). A circuit for simultaneous reception of power and data using a solar cell (under review).
- Kahn, J. M., & Barry, J. R. (1997). Wireless infrared communications. *Proceedings of the IEEE*, 85(2), 265-298.
- Kechiche, S. (2018). IoT: the Next Wave of Connectivity and Services. Retrieved 2020-03-10, from <https://www.gsmainelligence.com/research/2018/04/iot-the-next-wave-of-connectivity-and-services/665/>
- Kikuchi, K., Okoshi, T., & Kitano, J. (1981). Measurement of bit-error rate of heterodyne-type optical communication system - a simulation experiment. *IEEE Journal of Quantum Electronics*, 17(12), 2266-2267.
- Krikidis, I., Timotheou, S., Nikolaou, S., Zheng, G., Ng, D. W. K., & Schober, R. (2014, Nov). Simultaneous wireless information and power transfer in modern communication systems. *IEEE Communications Magazine*, 52(11), 104-110.
- Kumar, R. A., Suresh, M. S., & Nagaraju, J. (2003). Time domain technique to measure solar cell capacitance. *Review of Scientific Instruments*, 74(7), 3516-3519.
- Lee, S. (2015). A passive transponder for visible light identification using a solar cell. *IEEE Sensors Journal*, 15(10), 5398-5403.

- Leon-Salas, W. D., & Fan, X. (2018, May). Exploiting luminescence emissions of solar cells for optical frequency identification (OFID). In *2018 IEEE International Symposium on Circuits and Systems (ISCAS)* (p. 1-5).
- Leon-Salas, W. D., & Fan, X. (2019a). Photo-luminescence modulation circuits for solar cell based optical communications. In *2019 IEEE International Symposium on Circuits and Systems (ISCAS)* (p. 1-5).
- Leon-Salas, W. D., & Fan, X. (2019b). Solar cell photo-luminescence modulation for optical frequency identification devices. *IEEE Transactions on Circuits and Systems I: Regular Papers*, 66(5), 1981-1992.
- Leon-Salas, W. D., & Fan, X. (2018). Live demonstration: modulating luminescence emissions of solar cells for sensing and identification. In *2018 IEEE International Symposium on Circuits and Systems (iscas)* (p. 1-1).
- Leon-Salas, W. D., Fan, X., Hidalgo, J., Peleato, B., & Molina, P. J. (2020). Modulation of LED photo-luminescence for underwater optical communications. In *2020 IEEE International Symposium on Circuits and Systems (ISCAS)* (p. 1-5).
- Leon-Salas, W. D., Fan, X., & Lee, S. (2019). Live demonstration: a wireless sensor using a solar cell optical transceiver. In *2019 IEEE International Symposium on Circuits and Systems (ISCAS)* (p. 1-1).
- Leon-Salas, W. D., Fan, X., Zhang, Y., & Kadirvelu, S. (2019). Wireless optical communications with GaAs solar cells. In *Frontiers in Optics Laser Science* (p. JTU4A.83).
- Li, J., Liu, A., Shen, G., Li, L., Sun, C., & Zhao, F. (2015). Retro-VLC: enabling battery-free duplex visible light communication for mobile and IoT applications. In *Proceedings of the 16th International Workshop on Mobile Computing Systems and Applications* (p. 21–26).
- Liu, J., Faulkner, G., Choubey, B., Collins, S., & O'Brien, D. C. (2019). An optical transceiver powered by on-chip solar cells for IoT smart dusts with optical wireless communications. *IEEE Internet of Things Journal*, 6(2), 3248-3256.
- Liu, J. J., Faulkner, G., Choubey, B., Liu, J., Chen, R. Q., O'brien, D. C., & Collins, S. (2014). Optically powered energy source in a standard CMOS process for integration in smart dust applications. *IEEE Journal of the Electron Devices Society*, 2(6), 158-163.

- Liu, Y., Chen, H., Liang, K., Hsu, C., Chow, C., & Yeh, C. (2016). Visible light communication using receivers of camera image sensor and solar cell. *IEEE Photonics Journal*, 8(1), 1-7.
- Lu, H., Li, C., Chen, H., Ho, C., Cheng, M., Yang, Z., & Lu, C. (2017). A 56 gb/spam⁴ vcsel-based LiFi transmission with two-stage injection-locked technique. *IEEE Photonics Journal*, 9(1), 1-8.
- Mahdiraji, G. A., & Zahedi, E. (2006). Comparison of selected digital modulation schemes (OOK, PPM and DPIM) for wireless optical communications. In *2006 4th Student Conference on Research and Development* (p. 5-10).
- Malik, B., & Zhang, X. (2015). Solar panel receiver system implementation for visible light communication. In *2015 IEEE International Conference on Electronics, Circuits, and Systems (ICECS)* (p. 502-503).
- Mamun, M. A. A., & Yuce, M. R. (2019, Sep.). Sensors and systems for wearable environmental monitoring toward IoT-enabled applications: a review. *IEEE Sensors Journal*, 19(18), 7771-7788.
- Markovic, D., Chang, C., Richards, B., So, H., Nikolic, B., & Brodersen, R. W. (2007). ASIC design and verification in an FPGA environment. In *2007 IEEE Custom Integrated Circuits Conference* (p. 737-740).
- Maxim Integrated. (2008). Nano power triple-output, single-inductor, multiple-output (SIMO) buck-boost regulator. Retrieved 2021-04-08, from <https://datasheets.maximintegrated.com/en/ds/MAX17270-MAX17271.pdf>
- McSpadden, J. O., Lu Fan, & Kai Chang. (1998). Design and experiments of a high-conversion-efficiency 5.8-ghz rectenna. *IEEE Transactions on Microwave Theory and Techniques*, 46(12), 2053-2060.
- Miller, O. D., Yablonovitch, E., & Kurtz, S. R. (2012, July). Strong internal and external luminescence as solar cells approach the Shockley–Queisser limit. *IEEE Journal of Photovoltaics*, 2(3), 303-311.
- Moayeri Pour, G., Benyhesan, M. K., & Leon-Salas, W. D. (2014). Energy harvesting using substrate photodiodes. *IEEE Transactions on Circuits and Systems II: Express Briefs*, 61(7), 501-505.

- Monmayrant, A., Weber, S., & Chatel, B. (2010, may). A newcomer's guide to ultra short pulse shaping and characterization. *Journal of Physics B: Atomic, Molecular and Optical Physics*, 43(10), 103001.
- Moreno, I. (2006). Spatial distribution of LED radiation. In *International optical design conference 2006* (Vol. 6342, p. 378-384).
- Narasimhan, R., Audeh, M. D., & Kahn, J. M. (1996). Effect of electronic-ballast fluorescent lighting on wireless infrared links. In *Proceedings OFICC/SUPERCOMM '96 - International Conference on Communications* (Vol. 2, p. 1213-1219 vol.2).
- Nayak, P. K., Mahesh, S., Snaith, H. J., & Cahen, D. (2019, March). Photovoltaic solar cell technologies: analysing the state of the art. *Nature Reviews Materials*, 4, 269-285.
- O'brien, D. C., Liu, J. J., Faulkner, G. E., Sivathasan, S., Yuan, W. W., Collins, S., Pithamiron, V. (2009). Design and implementation of optical wireless communications with optically powered smart dust motes. *IEEE Journal on Selected Areas in Communications*, 27(9), 1646-1653.
- Omairi, A., Ismail, Z. H., Danapalasingam, K. A., & Ibrahim, M. (2017). Power harvesting in wireless sensor networks and its adaptation with maximum power point tracking: current technology and future directions. *IEEE Internet of Things Journal*, 4(6), 2104-2115.
- Park, G., Rosing, T., Todd, M. D., Farrar, C. R., & Hodgkiss, W. (2008). Energy harvesting for structural health monitoring sensor networks. *Journal of Infrastructure Systems*, 14(1), 64-79.
- Pillai, D. S., Ram, J. P., Ghias, A. M. Y. M., Mahmud, M. A., & Rajasekar, N. (2020). An accurate, shade detection-based hybrid maximum power point tracking approach for pv systems. *IEEE Transactions on Power Electronics*, 35(6), 6594-6608.
- Piñuela, M., Mitcheson, P. D., & Lucyszyn, S. (2013, July). Ambient rf energy harvesting in urban and semi-urban environments. *IEEE Transactions on Microwave Theory and Techniques*, 61(7), 2715-2726.
- Qin, Y., Vu, T. T., & Ban, Y. (2012). Toward an optimal algorithm for lidar waveform decomposition. *IEEE Geoscience and Remote Sensing Letters*, 9(3), 482-486.
- Queraltà, J. P., Yuhong, F., Salomaa, L., Qingqing, L., Gia, T. N., Zou, Z., Westerlund, T. (2019). FPGA-based architecture for a low-cost 3d lidar design and implementation from multiple rotating 2d lidars with ROS. In *2019 IEEE Sensors* (p. 1-4).

- Raguse, J. M., & Sites, J. R. (2015). Correlation of electroluminescence with open-circuit voltage from thin-film cdte solar cells. *IEEE Journal of Photovoltaics*, 5(4), 1175-1178.
- Rajendran, J., Leon-Salas, W. D., Fan, X., Zhang, Y., Vizcardo, M. A., & Postigo, M. (2020). On the development of a low-cost photosynthetically active radiation (par) sensor. In *2020 IEEE International Symposium on Circuits and Systems (ISCAS)* (p. 1-5).
- Rau, U. (2012). Superposition and reciprocity in the electroluminescence and photoluminescence of solar cells. *IEEE Journal of Photovoltaics*, 2(2), 169-172.
- Razavi, B. (2001). *Design of analog CMOS integrated circuits*. McGraw Hill Higher Education.
- Schick, K., Daub, E., Finkbeiner, S., & Würfel, P. (1992, February). Verification of a generalized Planck law for luminescence radiation from silicon solar cells. *Applied Physics A: Materials Science & Processing*, 54(2), 109-114.
- Selvakumar, S., Madhusmita, M., Koodalsamy, C., Simon, S. P., & Sood, Y. R. (2019). High-speed maximum power point tracking module for PV systems. *IEEE Transactions on Industrial Electronics*, 66(2), 1119-1129.
- Subudhi, B., & Pradhan, R. (2019). A new adaptive maximum power point controller for a photovoltaic system. *IEEE Transactions on Sustainable Energy*, 10(4), 1625-1632.
- Svilen, D., & Harald, H. (2015). *Principles of led light communications: towards networked lifi*. Cambridge University Press.
- Sze, S. M., & Ng, K. K. (n.d.). *Physics of semiconductor devices*. John Wiley and Sons, Inc.
- Texas Instruments. (2008). 800-ma/1000-ma, 3-mhz synchronous step-down converter with i2c compatible interface in chip scale packaging. Retrieved 2021-04-07, from <https://www.ti.com/lit/ds/symlink/tps62353.pdf>
- Tsonev, D., Videv, S., & Haas, H. (2015, Jan). Towards a 100 gb/s visible light wireless access network. *Opt. Express*, 23(2), 1627-1637.
- Ud Din, I., Guizani, M., Hassan, S., Kim, B., Khurram Khan, M., Atiquzzaman, M., & Ahmed, S. H. (2019). The internet of things: A review of enabled technologies and future challenges. *IEEE Access*, 7, 7606-7640.
- Wang, A., Calhoun, B. H., & Chandrakasan, A. P. (2006). *Sub-threshold design for ultra low-power systems (series on integrated circuits and systems)*. Springer-Verlag.
- Wang, Y., Zhang, P., Wang, X., Wang, T., Wang, D., Zhang, L., & Tong, S. (2018). Spectrum effect on output characteristics of wireless energy and data hybrid transmission system

- using a solar panel. In Y. Huang (Ed.), *Tenth International Conference on Information Optics and Photonics* (Vol. 10964, pp. 1077 – 1085).
- Wang, Z., Tsonev, D., Videv, S., & Haas, H. (2014). Towards self-powered solar panel receiver for optical wireless communication. In *2014 IEEE International Conference on Communications (ICC)* (p. 3348-3353)
- Wang, Z., Tsonev, D., Videv, S., & Haas, H. (2015). On the design of a solar-panel receiver for optical wireless communications with simultaneous energy harvesting. *IEEE Journal on Selected Areas in Communications*, 33(8), 1612-1623.
- Want, R. (2006). An introduction to rfid technology. *IEEE Pervasive Computing*, 5(1), 25-33.
- William, S., & Hans, Q. (1961). Detailed balance limit of efficiency of p-n junction solar cells. *Journal of Applied Physics*, 32(3), 510-519.
- Williams, E. W., & Hall, R. (1978). *Luminescence and excitation. In Luminescence and the light emitting diode* (p. 72-94).
- Yamazato, T., Takai, I., Okada, H., Fujii, T., Yendo, T., Arai, S., Kawahito, S. (2014). Image-sensor-based visible light communication for automotive applications. *IEEE Communications Magazine*, 52(7), 88-97.
- Zhang, J. (2000). Modulation analysis for outdoors applications of optical wireless communications. In *Wcc 2000 - icct 2000. 2000 International Conference on Communication Technology Proceedings* (Vol. 2, p. 1483-1487).
- Zhang, S., Tsonev, D., Videv, S., Ghosh, S., Turnbull, G. A., Samuel, I. D. W., & Haas, H. (2015, Jul). Organic solar cells as high-speed data detectors for visible light communication. *Optica*, 2(7), 607-610.
- Zheng, Z., Liu, L., & Hu, W. (2017). Accuracy of ranging based on dmt visible light communication for indoor positioning. *IEEE Photonics Technology Letters*, 29(8), 679-682.